University of Pennsylvania
ScholarlyCommons

Publicly Accessible Penn Dissertations

Fall 12-22-2009

# Cellular and Molecular Analyses of Neural and Synaptic Development in Zebrafish

Yuanquan Song
*University of Pennsylvania*, yuanquan@mail.med.upenn.edu

Follow this and additional works at: http://repository.upenn.edu/edissertations

 Part of the Developmental Neuroscience Commons, and the Molecular and Cellular Neuroscience Commons

Recommended Citation
Song, Yuanquan, "Cellular and Molecular Analyses of Neural and Synaptic Development in Zebrafish" (2009). *Publicly Accessible Penn Dissertations*. 297.
http://repository.upenn.edu/edissertations/297

This paper is posted at ScholarlyCommons. http://repository.upenn.edu/edissertations/297
For more information, please contact libraryrepository@pobox.upenn.edu.

# Cellular and Molecular Analyses of Neural and Synaptic Development in Zebrafish

**Abstract**
Proper function of the nervous system requires the precise wiring of neuronal circuitry, which is established during development via mechanisms that guide cells to establish a correct identity, direct axons to navigate to and make synaptic connections with appropriate targets, and establish and maintain the function of synaptic circuits. Dysfunction of genes implicated in one or more of these processes has been linked to human neurological disorders with behavioral and cognitive manifestations. However, our understanding of how specific gene defects affect circuitry formation, function and in turn behavior remains fragmentary.

I have used zebrafish as a genetic model system to begin to address some aspects of this central question. I performed in vivo imaging and cellular analyses of the formation of a peripheral neural circuit, synapses between motor neurons and muscle fibers, called neuromuscular junctions. I then characterized two zebrafish mutants, identified from a small-scale genetic screen for neuromuscular synaptic defects, slytherin (srn) and xavier (xav). Analyses of srn uncovered a previously underappreciated role for protein fucosylation in several aspects of neural development. Analyses of xav suggest critical roles for mitochondria during neural development. Given that the corresponding mutations in humans result in disorders with poorly explored neural defects, the molecular and cellular characterization of these mutants may shed light on our understanding of the neural and synaptic phenotypes in human patients.

**Degree Type**
Dissertation

**Degree Name**
Doctor of Philosophy (PhD)

**Graduate Group**
Neuroscience

**First Advisor**
Rita J. Balice-Gordon

**Keywords**
zebrafish, synaptogenesis, fucosylation, notch, etfdh, madd

**Subject Categories**
Developmental Neuroscience | Molecular and Cellular Neuroscience

This dissertation is available at ScholarlyCommons: http://repository.upenn.edu/edissertations/297

# CELLULAR AND MOLECULAR ANALYSES OF NEURAL AND SYNAPTIC DEVELOPMENT IN ZEBRAFISH

**Yuanquan Song**

**A DISSERTATION**

**in**

**Neuroscience**

**Presented to the Faculties of the University of Pennsylvania**

**in**

**Partial Fulfillment of the Requirements for the**

**Degree of Doctor of Philosophy**

**2009**

**Supervisor (or co-Supervisors) of Dissertation**

_____

Rita J. Balice-Gordon, Ph.D.

**Graduate Group Chairperson**

_____

Rita J. Balice-Gordon, Ph.D.

**Dissertation Committee** *(typed names and title; no signatures)*

Steven S. Scherer, M.D., Ph.D.

Greg Bashaw, Ph.D.

Jonathan A. Raper, Ph.D.

Michael J. Bennett, PhD, FRCPath, FACB

# ABSTRACT

## CELLULAR AND MOLECULAR ANALYSES OF NEURAL AND SYNAPTIC DEVELOPMENT IN ZEBRAFISH

Yuanquan Song

Thesis advisor: Rita J. Balice-Gordon

Proper function of the nervous system requires the precise wiring of neuronal circuitry, which is established during development via mechanisms that guide cells to establish a correct identity, direct axons to navigate to and make synaptic connections with appropriate targets, and establish and maintain the function of synaptic circuits. Dysfunction of genes implicated in one or more of these processes has been linked to human neurological disorders with behavioral and cognitive manifestations. However, our understanding of how specific gene defects affect circuitry formation, function and in turn behavior remains fragmentary.

I have used zebrafish as a genetic model system to begin to address some aspects of this central question. I performed *in vivo* imaging and cellular analyses of the formation of a peripheral neural circuit, synapses between motor neurons and muscle fibers, called neuromuscular junctions. I then characterized two zebrafish mutants, identified from a small-scale genetic screen for neuromuscular synaptic defects, *slytherin* (*srn*) and *xavier* (*xav*). Analyses of *srn* uncovered a previously underappreciated role for protein fucosylation in several aspects of neural development. Analyses of *xav* suggest

critical roles for mitochondria during neural development. Given that the corresponding mutations in humans result in disorders with poorly explored neural defects, the molecular and cellular characterization of these mutants may shed light on our understanding of the neural and synaptic phenotypes in human patients.

## TABLE OF CONTENTS

**Abstract** **ii**

**Table of Contents** **iv**

**List of Figures** **vi**

**List of Tables** **ix**

**Chapter 1:** Introduction 1

References 14

**Chapter 2**: *In vivo* imaging of preferential motor axon outgrowth to and synaptogenesis at prepatterned acetylcholine receptor clusters in embryonic zebrafish skeletal muscle

Abstract 22

Introduction 23

Materials and Methods 26

Results 34

Discussion 45

References 53

Figures and Legends 61

**Chapter 3**: Notch-dependent and -independent mechanisms underlie neural and synaptic defects in *slytherin*, a zebrafish model for human congenital disorders of glycosylation

Abstract 89

Introduction 90

Materials and Methods 93

Results 97

Discussion 108

References 112

Figures and Legends 119
Supplemental Methods, Results and Figures 140

**Chapter 4**: Mutations in electron transfer flavoprotein (ETF) and electron transfer flavoprotein dehydrogenase (ETFDH), cause fatty acid metabolism and mitochondrial dysfunction, unbalanced oxidative phosphorylation and glycolysis, and lead to severe neural defects in zebrafish and humans
Abstract 158
Introduction 159
Materials and Methods 162
Results 170
Discussion 183
References 186
Figures and Legentds 193
Supplemental Results and Figures 208

**Chapter 5**: General Conclusions and Future Directions 236
References 244

## LIST OF FIGURES

**Chapter 2:**

Fig. 1 Location of prepatterned AChR clusters in myotomal muscle. 61

Fig. 2 Dynamics of prepatterned AChR clusters. 63

Fig. 3 Motor axon growth cones preferentially extend toward prepatterned AChR clusters. 67

Fig. 4 Motor axon filopodia preferentially extend toward and contact prepatterned AChR clusters. 70

Fig. 5 Filopodia are preferentially extended from synapses. 73

Fig. 6 Postsynaptic AChR clusters precede presynaptic vesicle clusters during initial neuromuscular synaptogenesis. 75

Fig. 7 Insertion of new AChRs and redistribution of prepatterned AChRs during initial neuromuscular synaptogenesis. 78

Fig. 8. AChR activity or AChR clusters are not required for motor axon outgrowth or neuromuscular synaptogenesis. 80

Supplemental Fig. 1 VAMP-GFP marks sites of presynaptic vesicle clusters and does not alter motor axon outgrowth. 83

Supplemental Fig. 2 Blockade of sodium channels with tricaine does not affect dispersal of prepatterned AChR clusters or initial motor axon outgrowth. 85

**Chapter 3**:

Figure 1. *Slytherin* external phenotype, genotype, cloning and mRNA rescue of *srn* mutants. 119

Figure 2. *slytherin* mutants exhibit reduced protein fucosylation as measured by AAL staining. 122

Figure 3. Supplementation with exogenous GDP-fucose rescues *srn* external phenotypes and restores AAL staining. 124

Figure 4. Reduction in Notch-Delta signaling accounts for some *srn* phenotypes. 126

Figure 5. *mib* and DAPT treatment exclude *srn* phenotypes. 129

Figure 6. NICD rescues *srn* neuro- and gliogenesis phenotypes. 131

Figure 7. *srn* mutants showed aberrant expression of Notch responsive genes similar to *mib* mutants. 133

Figure 8. *Slytherin* mutants exhibit defects in neuromuscular synaptogenesis due in part to reduction in Notch-Delta signaling. 135

Figure 9. *Slytherin* mutants exhibit defects in axon branching and CNS synaptic connectivity that are independent of Notch-Delta signaling. 137

Supplemental Figure 1. *Gmds* mRNA localization by *in situ* hybridization in wild type zebrafish embryos from 12 to 72 hpf. 143

Supplemental Figure 2. Modeling of zebrafish GMDS protein structure. 145

Supplemental Figure 3. GDP-fucose rescue of *srn* and morpholino knockdown of *gmds*. 147

Supplemental Figure 4. Secondary motor neuron number is reduced in *mib* but not *srn*, *des* or *dla* compared to wild type embryos. 150

Supplemental Figure 5. Reduction in Notch-Delta signaling accounts for some *srn* phenotypes in the retina. 152

Supplemental Figure 6. Muscle patterning is grossly normal in *srn* mutants. 154

**Chapter 4**:

Figure 1. *xavier* external phenotype, genotype, cloning and morpholino phenocopy of *xav* mutants 193

Figure 2. *xavier* mutants display abnormal acylcarnitine and organic acid profile 195

Figure 3. *xav* mutants exhibit mitochondrial dysfunction 197

Figure 4. Human MADD fibroblast cells display similar mitochondrial defects as *xav* 200

Figure 5. Increased aerobic glycolysis in MADD fibroblasts and *xav* 202

Figure 6. *xav* exhibits increased neural cell proliferation as a result of increased glycolysis, due to perturbation of the PPARG-ERK pathway 205

Supplemental Figure 1. Genetic map of the *xav* locus 215

Supplemental Figure 2. Nonsense mediated decay and nonsense mediated alternative splicing of *etfdh* transcript in *xav,* and morpholino knock down of *etfdh* 217

Supplemental Figure 3. *xav* mutants display polycystic kidney like phenotypes. 219

Supplemental Figure 4. *xav* mutants exhibit respiratory deficiency 221

Supplemental Figure 5. *xav* mutants exhibit neural and glial defects and cell death 223

Supplemental Figure 6. *xav* mutants exhibit reduced motor axon branching and neuromuscular synaptogenesis that are not caused by change of motor neuron number or viability 225

Supplemental Figure 7. *xav* mutants display electrophysiological properties in the muscle, comparable to WT 227

Supplemental Figure 8. *xav* mutants exhibit aberrant mitochondria distribution in motor neurons 229

Supplemental Figure 9. *xav* mutants exhibit cell death throughout the nervous system that is rescued by p53 morpholino knockdown and does not account for the motor axon branching, neuromuscular synapse or motility defects 231

## LIST OF TABLES

**Chapter 3**:

Supplemental Table 1. Primers used for qRT-PCR. 142

**Chapter 4:**

Supplemental Table 1. Primer sequences for new zebrafish simple sequence repeat (SSR) markers 233

Supplemental Table 2. Primers for qRT-PCR analyses of gene expression in *xav* and fibroblasts from human MADD patients 234

# Chapter 1

## Introduction

This chapter is published in

International Anesthesiology Clinics:
Spring 2006 - Volume 44 - Issue 2 - pp 145-178

**Formation and Plasticity of Neuromuscular Synaptic Connections**

Song, Yuanquan BS; Panzer, Jessica A. MD, PhD; Wyatt, Ryan M. BS; Balice-Gordon, Rita J. PhD

The nervous system becomes wired into circuits that are fine tuned to subserve particular functions and behaviors through a series of events including neurogenesis and differentiation; cell migration, axon guidance and synapse formation; synaptic pruning and circuit maturation and maintenance. Perturbation of any of these steps results in neurodevelopmental, cognitive or behavioral abnormalities, as well as neurological and psychiatric disorders. My thesis project utilized zebrafish as a model organism to characterize some of the cellular and molecular mechanisms underlying synapse formation, and also revealed several mechanisms that impact other aspects of neural development. Here I review our current understanding of mechanisms underlying synapse formation, as a basis for my dissertation.

The specificity of synaptic connections that is essential for nervous system function arises during development through a series of events, including axon outgrowth and guidance, target selection, synaptogenesis and synapse elimination. Neuromuscular synapses between spinal motor neurons and skeletal muscle fibers have become one of the most widely used model systems to study these events due to its relatively large size, accessibility and the wealth of molecular and functional information about their formation, maintenance and plasticity (Goda and Davis, 2003; Sanes and Lichtman, 1999).

Neuromuscular synapses are established through complex multi-directional signaling among presynaptic motor neurons, postsynaptic muscle fibers (Burden, 2002; Luo et al., 2003; Sanes and Lichtman, 2001) and perisynaptic glia (Koenig et al., 1998). These synapses consists of specialized regions of the presynaptic membrane, termed active zones, at which clustered synaptic vesicles fuse and release the neurotransmitter acetylcholine (ACh), as well as peptides such as calcitonin gene related peptide (CGRP) and other signaling molecules. Directly apposed to the presynaptic active zones are acetylcholine receptors (AChRs) which cluster at the crests of junctional folds in the muscle fiber membrane. These AChRs bind ACh that has diffused across the synaptic cleft, leading to subsequent depolarization, which, if above threshold, leads to contraction of the muscle fiber (Sanes and Lichtman, 1999). The temporal and spatial extent of ACh signaling is regulated by acetycholinesterase (AChE), which is located within the basal lamina that invaginates the synaptic cleft, and cleaves ACh, thereby terminating the signal (Rotundo, 2003). Surrounding the neuromuscular synapses are perisynaptic

Schwann cells, specialized glia that have been found to modulate synaptic structure, activity, and response to injury (Koenig et al., 1998; Son et al., 1996).

*The role of the Agrin – MuSK – Lrp4 –Rapsyn pathway in neuromuscular synaptogenesis*

Neuromuscular synaptic function depends critically on the precise spatial apposition of presynaptic motor neuron acetylcholine release sites with high-density clusters of AChRs in the postsynaptic muscle fiber membrane. During neuromuscular synaptogenesis, AChRs are clustered before innervation, prepatterning a central muscle region where synapses will later be established. Motor neuron signals refine the muscle prepattern by clustering AChRs beneath terminals and dispersing uninnervated clusters so that AChRs become localized to, and are stably maintained, at nascent synapses. Over the last 15 years, work from a number of groups has uncovered the basic signaling mechanisms that underlie these events (reviewed in Sanes and Licthman 2001). Muscle specific kinase (MuSK), a receptor tyrosine kinase expressed by postsynaptic muscle fibers, is essential for the formation of aneural, prepatterned AChR clusters as well as for the formation and maintenance of later, innervated AChR clusters (Lin et al., 2001; Yang et al., 2001). The presynaptically released proteoglycan Agrin, that activates MuSK signaling, is now more fully understood to be important as an anti-declustering, AChR cluster maintenance factor. A role for the neurotransmitter ACh as a cluster dispersion factor for non-innervated AChR clusters has also recently come to be appreciated (Misgeld et al. 2005).

A third protein shown to be crucial for the clustering of AChRs is the cytoskeletal linker protein rapsyn. Following activation by MuSK, Rapsyn, which binds both AChRs and β-dystroglycan, clusters at synapses, resulting in the synaptic clustering of AChRs (Gautam et al., 1995). Although AChR clustering is completely absent in Rapsyn mutant mice (Gautam et al., 1995), many aspects of synaptic differentiation, including concentration of MuSK at synapses and selective transcription of AChR genes by synaptic nuclei, are unaffected (Apel et al., 1997; Gautam et al., 1995). Thus, although necessary for neuromuscular synaptogenesis, it may be that Rapsyn plays a role in a relatively late step in the Agrin-MuSK signaling cascade. The understanding of Rapsyn's role in directing synaptic AChRs clustering is further complicated by recent findings that AChRs themselves are necessary to direct Rapsyn clusters to synapses (Grow and Gordon, 2000; Huh and Fuhrer, 2002; Missias et al., 1997; Ono et al., 2001).

While a wealth of genetic evidence supports the Agrin-MuSK hypothesis, evidence for a protein-protein interaction between Agrin and MuSK has been lacking. Earlier work had proposed that an additional protein complex that directly bind Agrin and was expressed specifically in muscle cells, called myotube-associated specificity component (MASC), was required to constitute a fully functional receptor complex that both binds and responds to Agrin (Glass et al., 1996). Recently mice lacking Lrp4 expression was reported to display neuromuscular synaptic defects strikingly similar to those present in mice lacking MuSK expression (DeChiara et al., 1996), namely the absence of postsynaptic AChR clusters, extensive aberrant presynaptic branching and reduced formation of presynaptic terminals (Weatherbee et al., 2006). Prompted by this observation, latest work from Steve Burden's and Lin Mei's labs, proved that Lrp4 is the

long sought MASC, and that it binds, clusters and works in concert with Agrin to activate MuSK (Kim et al., 2008; Zhang et al., 2008). These observations raise the question of whether Lrp4 clustering precedes and in turn leads to MuSK clustering, priming transcriptional mechanisms in sub-synaptic nuclei and protein-protein interactions that lead to the formation of aneural AChR clusters and ultimately the formation of functional neuromuscular synapses.

*Intracellular signaling mechanisms downstream of MuSK activation*

Although the roles of Agrin, MuSK, and Rapsyn in neuromuscular synaptogenesis have been relatively well established, much less is known about the identity and role of effectors downstream of MuSK activation. Recent work, however, has begun to fill in some of these gaps (Luo et al., 2003). The activity of several muscle enzymes, including Rho-family GTPases, NO synthetases (NOS), and geranylgeranyl-transferase I, has been shown to increase in response to Agrin (Luo et al., 2002), and both NO and cGMP have been implicated in the regulation of AChR clustering (Jones and Werle, 2000; Luck et al., 2000). AChRs are tightly associated with cytoskeletal proteins, and since Rho GTPases are well-known regulators of the cytoskeleton, they may play a role in translating MuSK activation into the cytoskeletal reorganization required to cluster AChRs synaptically (Luo et al., 2003). One Rho-family GTPase, Rac1 has been implicated in initial induction of small AChR clusters by Agrin, and Rho itself appears to be required to then condense these "microclusters" into full size AChR clusters (Weston et al., 2003).

Given MuSK's importance in neuromuscular synapse formation, much attention has focused on identifying its downstream interactors. Recent work has identified Disheveled (Dvl) as a MuSK binding protein (Luo et al., 2002). Dvl was originally identified in Drosophila as a molecule that is activated by the Wingless (Wnt) receptor Frizzled (Dierick and Bejsovec, 1999). Interestingly, MuSK shares a conserved extracellular domain with Wnt receptors (Saldanha et al., 1998). MuSK activation of Dvl signaling may result in AChR clustering through the function of the Rho GTPases discussed above, as it is known that Dvl activation results in activation of Rho GTPases (Habas et al., 2001). In addition, Dvl is also known to inhibit phosphorylation of β-catenin (Cadigan and Nusse, 1997), and β-catenin itself has been shown to bind Rapsyn (Luo et al., 2003) and inhibit the clustering activity of Agrin (Zhang et al., 2001). These data are consistent with a model in which Dvl signaling results in reduced binding of β-catenin to Rapsyn, allowing Rapsyn to cluster AChRs (Luo et al., 2003), although this model remains to be tested. Interestingly, Wnt signaling has been implicated in the development of both CNS synapses (Hall et al., 2000) and of the glutamatergic neuromuscular synapses in Drosophila. Thus, it may be that this evolutionarily conserved pathway is involved in the formation of a diverse array of structurally and functionally distinct synapses.

*The role of Agrin – MuSK – Lrp4 signaling in presynaptic differentiation*

In addition to lacking postsynaptic specializations, Agrin, MuSK and Lrp4 mutant mice also display aberrant presynaptic differentiation. Motor axons are not confined to a

discrete endplate band, but instead branch extensively throughout the muscle. Thus, Agrin, MuSK and Lrp4 signaling must induce a retrograde signal that instructs axons to stop and undergo presynaptic differentiation (DeChiara et al., 1996; Gautam et al., 1996). *In vitro* experiments have demonstrated that Agrin inhibits neurite outgrowth (Bixby et al., 2002; Campagna et al., 1995; Chang et al., 1997; Halfter et al., 1997; Mantych and Ferreira, 2001), and can initiate some aspects of presynaptic differentiation at sites of neurite contact with Agrin expressing cells (Campagna et al., 1995). The current understanding of the cellular and molecular events underlying presynaptic development, however, is much less advanced than that of postsynaptic differentiation.

*The role of prepatterned AChR clusters in neuromuscular synaptogenesis*

The presence of prepatterned (aneural) AChR clusters was not well appreciated until recently. That muscle might be patterned independent of motor innervation was first strongly suggested in studies of the mouse topisomerase IIβ knockout (Yang et al., 2000). In these mutants, although motor axons fail to branch within muscles, a band of AChR clusters is observed within the central region of the muscle (Yang et al., 2000). These AChR clusters are present in an area ca. two-fold wider than the normal endplate zone (Yang et al., 2000). This finding has been confirmed in additional mouse mutants in which motor nerves are disrupted (Lin et al., 2000) or fail to form (Lin et al., 2001; Yang et al., 2001), or in which motor neurons are ablated (Yang et al., 2001).

In light of these findings, researchers have re-examined the early embryonic stages of neuromuscular synaptogenesis and found that AChR clusters are present in wild type muscle along the endplate band prior to the formation of neuromuscular synapses in a distribution similar to that seen in the genetically manipulated animals discussed above (Feng et al., 2000; Lin et al., 2001; Lupa and Hall, 1989; Morris et al., 1999). These phenomena have been extensively examined in the mouse, where AChR clusters appear 1-2 days after the first motor axons reach the muscle, at approximately the same time that motor axon branches first contact myotubes (Lin et al., 2001; Misgeld et al., 2002). Moreover, recent studies in zebrafish have demonstrated that AChR clusters are also present in myotomal muscles, but well before motor axons extend from the spinal cord (Flanagan-Steet et al., 2005; Panzer et al., 2005; Panzer et al., 2006). Thus postsynaptic specializations are prepatterned in vertebrate muscles well in advance of innervation.

Less well studied then the mechanisms underlying the formation of prepatterned AChR clusters is their actual role in synapse formation. *In vitro* studies of nerve-muscle co-cultures demonstrated that motor axon growth cones did not preferentially contact "hot spots," but rather appeared to contact myotubes at random, inducing new AChR clusters at sites of contact (Anderson and Cohen, 1977; Frank and Fischbach, 1979). These and related studies (Kuromi and Kidokoro, 1984; Role et al., 1985; Ziskind-Conhaim et al., 1984) further showed that "hot spots" are stable in the absence of nerves, but rapidly disperse following synaptogenesis. It may be that, *in vivo*, motor axons similarly ignore prepatterned AChR clusters.

In contrast, during axon regeneration in adult muscle, pre-existing AChR clusters are selectively reinnervated (Bennett and Pettigrew, 1976). Similarly, during development, motor axons might contact prepatterned AChR clusters, either via an as-yet unidentified attractive cue or via random exploration, and incorporate them into newly formed synapses. In mutant mice in which motor axons branch extensively and grow beyond the confines of the endplate zone, synaptic terminals are still restricted to the central region of the muscle, indicating that the prepattern may play a key role in defining the location of future synapses (Yang et al., 2001).

Further supporting the idea that motor axons might selectively innervate prepatterned AChR clusters is the fact that no uninnervated AChR clusters are observed in ChAT knockout mice in which prepattern dispersal is theoretically absent (Brandon et al., 2003; Misgeld et al., 2002). If prepattern dispersal is indeed disrupted in ChAT mutants, the observed lack of uninnervated AChR clusters must indicate that random exploration by growth cones is sufficient to result in contact with and innervation of all prepatterned AChR clusters, or that there is a cue attracting motor axon growth cones to AChR clusters. In support of the latter hypothesis, it is thought that muscle-intrinsic cues are present at future postsynaptic sites on drosophila muscle fibers, and that these cues trigger axon termination and synaptogenesis (Broadie and Bate, 1993).

Recent work in zebrafish, however, has provided direct evidence revealing a critical role of postsynaptic muscle prepatterning during neuromuscular synaptogenesis. *In vivo* time lapse studies have shown that some prepatterned AChR clusters are directly incorporated into synapses (Flanagan-Steet et al., 2005; Panzer et al., 2006); and that

selective outgrowth of growth cones and filopodia towards prepatterned AChR clusters have been observed, suggesting that one function of the muscle prepattern is to determine the sites of future synapses (Panzer et al., 2006). Although the underlying mechanism remains unclear, pharmacological and genetic analysis have demonstrated that AChR activity, overall excitability and AChR protein itself are dispensable for these events to occur, suggesting that other cues that are co-patterned with AChR clusters may play this instructive role (Panzer et al., 2006). One candidate is MuSK or a downstream signaling component. In mouse, MuSK has been shown to be colocalized with prepatterned AChR clusters (Burden, 2002), and defects in motor axon outgrowth, branching and initial neuromuscular synaptogenesis are observed in MuSK mutant mice (Sanes and Lichtman, 1999) and in *unplugged* mutant zebrafish in which the zebrafish MuSK homolog is absent (Zhang et al., 2004).

Taken together, two distinct modes of synaptogenesis can be proposed. In the first mode, initial synapses are formed at sites that contain preexisting neurotransmitter receptor clusters. In a second and possibly contemporaneous mode, additional synapses are formed by the clustering of receptors beneath presynaptic nerve terminals (Flanagan-Steet et al., 2005; Panzer et al., 2006). These latter events are mediated by Agrin-MuSK and other signaling (Sanes and Lichtman, 1999).

*Mutagenesis in zebrafish to study neuromuscular synapse formation*

As discussed above, several of the molecular events underlying the differentiation of postsynaptic specializations are known. However, many of the molecules connecting

these events into a coherent signaling pathway remain to be elucidated. In addition, the cell-cell signaling mechanisms mediating the differentiation of presynaptic nerve terminals and regulating synapse number, size and location are poorly understood. The technical limitations inherent in studying early embryonic development in a mammalian system and the difficulty of performing forward genetic screens in mammals has limited our understanding of the cellular events that take place during neuromuscular synaptogenesis and hampered the discovery of the molecules which underlie them.

Zebrafish is a useful model system in which to address these issues. The development of spinal motor neurons and myotomal muscle targets has been described in detail (Eisen, 1998; Westerfield and Eisen, 1988). The optical transparency, external fertilization and rapid development of embryos facilitate the cellular analysis of early stages in neuromuscular synaptogenesis. These advantages, combined with the large number of embryos produced per clutch, has allowed performing mutagenesis screens which have revealed genetic, molecular and cellular mechanisms underlying many aspects of neural development.

Towards this goal, our lab previously performed a small-scale forward mutagenesis screen to identify genes important for neuromuscular synaptogenesis (Panzer et al., 2005). Form this screen, six novel mutants were identified that display defects including axon outgrowth, branching, pathfinding, AChR clustering and synaptogenesis. Uncovering the genetic mutations underlying these mutants and characterization of the responsible signaling events will provide valuable insights towards

a more complete understanding of the establishment and function of neuromuscular as well as central synapses.

*Summary of Dissertation Chapters*

Although the mechanisms underlying the formation of neuromuscular synapses remain amongst the most well-understood of any synapse, it is clear that many questions still remain. The identity of the repertoire of molecules that mediate and modulate the clustering of AChRs at synapses, as well as the molecular mediators and modulators of presynaptic differentiation, remain unknown. In addition, the events initiating the dynamic clustering and dispersal of prepatterned AChRs, as well as their role in neuromuscular synaptogenesis, remains poorly understood.

To begin to address these questions, I examined neuromuscular synaptogenesis in live zebrafish embryos, and established a potential role for prepatterned AChRs in the formation of mature neuromuscular connectivity (see Chapter 2, published as Panzer, Song et al., 2006). I then characterized two mutants identified in a small-scale genetic screen (Panzer et al., 2005), that provided insight into several of the mechanisms underlying synapse formation, in muscle as well as in the central nervous system. Analyses of one of these mutants, *slytherin (srn)*, whose mutation we found resides in GDP-mannose 4,6 dehydratase (GMDS), the rate-limiting enzyme in protein fucosylation, including that of Notch, demonstrated that defects in protein fucosylation leads to defects in neuronal differentiation, maintenance, axon branching, and synapse formation, due, at least in part, to malfunction of the Notch signaling pathway (see

Chapter 3, Song et al., in revision in Development). Analyses of a second mutant, *xavier* (*xav*), that we found has a nonsense mutation in electron transfer flavoprotein dehydrogenase (etfdh) critical for fatty acid metabolism and electron transport in mitochondria, demonstrated that defects in electron transfer flavoprotein genes cause fatty acid metabolism and mitochondrial dysfunction, unbalanced oxidative phosphorylation leading to an increase in glycolysis, in turn leading to severe neural defects in zebrafish and humans, at least in part, due to perturbation of the pparγ-ERK pathway (see Chapter 4, Song et al., in preparation).

**References**

**Anderson, M. J. and Cohen, M. W.** (1977). Nerve-induced and spontaneous redistribution of acetylcholine receptors on cultured muscle cells. *J Physiol* **268**, 757-73.

**Apel, E. D., Glass, D. J., Moscoso, L. M., Yancopoulos, G. D. and Sanes, J. R.** (1997). Rapsyn is required for MuSK signaling and recruits synaptic components to a MuSK-containing scaffold. *Neuron* **18**, 623-35.

**Bennett, M. R. and Pettigrew, A. G.** (1976). The formation of neuromuscular synapses. *Cold Spring Harb Symp Quant Biol* **40**, 409-24.

**Bixby, J. L., Baerwald-De la Torre, K., Wang, C., Rathjen, F. G. and Ruegg, M. A.** (2002). A neuronal inhibitory domain in the N-terminal half of agrin. *J Neurobiol* **50**, 164-79.

**Brandon, E. P., Lin, W., D'Amour, K. A., Pizzo, D. P., Dominguez, B., Sugiura, Y., Thode, S., Ko, C. P., Thal, L. J., Gage, F. H. et al.** (2003). Aberrant patterning of neuromuscular synapses in choline acetyltransferase-deficient mice. *Journal of Neuroscience* **23**, 539-49.

**Broadie, K. and Bate, M.** (1993). Innervation directs receptor synthesis and localization in Drosophila embryo synaptogenesis. *Nature* **361**, 350-3.

**Burden, S. J.** (2002). Building the vertebrate neuromuscular synapse. *J Neurobiol* **53**, 501-11.

**Cadigan, K. M. and Nusse, R.** (1997). Wnt signaling: a common theme in animal development. *Genes Dev* **11**, 3286-305.

**Campagna, J. A., Ruegg, M. A. and Bixby, J. L.** (1995). Agrin is a differentiation-inducing "stop signal" for motoneurons in vitro. *Neuron* **15**, 1365-74.

**Chang, D., Woo, J. S., Campanelli, J., Scheller, R. H. and Ignatius, M. J.** (1997). Agrin inhibits neurite outgrowth but promotes attachment of embryonic motor and sensory neurons. *Dev Biol* **181**, 21-35.

**DeChiara, T. M., Bowen, D. C., Valenzuela, D. M., Simmons, M. V., Poueymirou, W. T., Thomas, S., Kinetz, E., Compton, D. L., Rojas, E., Park, J. S. et al.** (1996). The receptor tyrosine kinase MuSK is required for neuromuscular junction formation in vivo. *Cell* **85**, 501-12.

**Dierick, H. and Bejsovec, A.** (1999). Cellular mechanisms of wingless/Wnt signal transduction. *Curr Top Dev Biol* **43**, 153-90.

**Eisen, J. S.** (1998). Genetic and molecular analyses of motoneuron development. *Current Opinion in Neurobiology* **8**, 697-704.

**Feng, G., Mellor, R. H., Bernstein, M., Keller-Peck, C., Nguyen, Q. T., Wallace, M., Nerbonne, J. M., Lichtman, J. W. and Sanes, J. R.** (2000). Imaging neuronal subsets in transgenic mice expressing multiple spectral variants of GFP. *Neuron* **28**, 41-51.

**Flanagan-Steet, H., Fox, M. A., Meyer, D. and Sanes, J. R.** (2005). Neuromuscular synapses can form in vivo by incorporation of initially aneural postsynaptic specializations. *Development* **132**, 4471-81.

**Frank, E. and Fischbach, G. D.** (1979). Early events in neuromuscular junction formation in vitro: induction of acetylcholine receptor clusters in the postsynaptic membrane and morphology of newly formed synapses. *J Cell Biol* **83**, 143-58.

**Gautam, M., Noakes, P. G., Moscoso, L., Rupp, F., Scheller, R. H., Merlie, J. P. and Sanes, J. R.** (1996). Defective neuromuscular synaptogenesis in agrin-deficient mutant mice. *Cell* **85**, 525-35.

**Gautam, M., Noakes, P. G., Mudd, J., Nichol, M., Chu, G. C., Sanes, J. R. and Merlie, J. P.** (1995). Failure of postsynaptic specialization to develop at neuromuscular junctions of rapsyn-deficient mice. *Nature* **377**, 232-6.

**Glass, D. J., DeChiara, T. M., Stitt, T. N., DiStefano, P. S., Valenzuela, D. M. and Yancopoulos, G. D.** (1996). The receptor tyrosine kinase MuSK is required for neuromuscular junction formation and is a functional receptor for agrin. *Cold Spring Harb Symp Quant Biol* **61**, 435-44.

**Goda, Y. and Davis, G. W.** (2003). Mechanisms of synapse assembly and disassembly. *Neuron* **40**, 243-64.

**Grow, W. A. and Gordon, H.** (2000). Acetylcholine receptors are required for postsynaptic aggregation driven by the agrin signalling pathway. *Eur J Neurosci* **12**, 467-72.

**Habas, R., Kato, Y. and He, X.** (2001). Wnt/Frizzled activation of Rho regulates vertebrate gastrulation and requires a novel Formin homology protein Daam1. *Cell* **107**, 843-54.

**Halfter, W., Schurer, B., Yip, J., Yip, L., Tsen, G., Lee, J. A. and Cole, G. J.** (1997). Distribution and substrate properties of agrin, a heparan sulfate proteoglycan of developing axonal pathways. *J Comp Neurol* **383**, 1-17.

**Hall, A. C., Lucas, F. R. and Salinas, P. C.** (2000). Axonal remodeling and synaptic differentiation in the cerebellum is regulated by WNT-7a signaling. *Cell* **100**, 525-35.

**Huh, K. H. and Fuhrer, C.** (2002). Clustering of nicotinic acetylcholine receptors: from the neuromuscular junction to interneuronal synapses. *Mol Neurobiol* **25**, 79-112.

**Jones, M. A. and Werle, M. J.** (2000). Nitric oxide is a downstream mediator of agrin-induced acetylcholine receptor aggregation. *Mol Cell Neurosci* **16**, 649-60.

**Kim, N., Stiegler, A. L., Cameron, T. O., Hallock, P. T., Gomez, A. M., Huang, J. H., Hubbard, S. R., Dustin, M. L. and Burden, S. J.** (2008). Lrp4 is a receptor for Agrin and forms a complex with MuSK. *Cell* **135**, 334-42.

**Koenig, J., de La Porte, S. and Chapron, J.** (1998). The Schwann cell at the neuromuscular junction. *J Physiol Paris* **92**, 153-5.

**Kuromi, H. and Kidokoro, Y.** (1984). Nerve disperses preexisting acetylcholine receptor clusters prior to induction of receptor accumulation in Xenopus muscle cultures. *Dev Biol* **103**, 53-61.

**Lin, W., Burgess, R. W., Dominguez, B., Pfaff, S. L., Sanes, J. R. and Lee, K. F.** (2001). Distinct roles of nerve and muscle in postsynaptic differentiation of the neuromuscular synapse. *Nature* **410**, 1057-64.

**Lin, W., Sanchez, H. B., Deerinck, T., Morris, J. K., Ellisman, M. and Lee, K. F.** (2000). Aberrant development of motor axons and neuromuscular synapses in erbB2-deficient mice. *Proc Natl Acad Sci U S A* **97**, 1299-304.

**Luck, G., Hoch, W., Hopf, C. and Blottner, D.** (2000). Nitric oxide synthase (NOS-1) coclustered with agrin-induced AChR-specializations on cultured skeletal myotubes. *Mol Cell Neurosci* **16**, 269-81.

**Luo, Z., Wang, Q., Dobbins, G. C., Levy, S., Xiong, W. C. and Mei, L.** (2003). Signaling complexes for postsynaptic differentiation. *J Neurocytol* **32**, 697-708.

**Luo, Z. G., Wang, Q., Zhou, J. Z., Wang, J., Luo, Z., Liu, M., He, X., Wynshaw-Boris, A., Xiong, W. C., Lu, B. et al.** (2002). Regulation of AChR clustering by Dishevelled interacting with MuSK and PAK1. *Neuron* **35**, 489-505.

**Lupa, M. T. and Hall, Z. W.** (1989). Progressive restriction of synaptic vesicle protein to the nerve terminal during development of the neuromuscular junction. *Journal of Neuroscience* **9**, 3937-45.

**Mantych, K. B. and Ferreira, A.** (2001). Agrin differentially regulates the rates of axonal and dendritic elongation in cultured hippocampal neurons. *J Neurosci* **21**, 6802-9.

**Misgeld, T., Burgess, R. W., Lewis, R. M., Cunningham, J. M., Lichtman, J. W. and Sanes, J. R.** (2002). Roles of neurotransmitter in synapse formation: development of neuromuscular junctions lacking choline acetyltransferase. *Neuron* **36**, 635-48.

**Missias, A. C., Mudd, J., Cunningham, J. M., Steinbach, J. H., Merlie, J. P. and Sanes, J. R.** (1997). Deficient development and maintenance of postsynaptic specializations in mutant mice lacking an 'adult' acetylcholine receptor subunit. *Development* **124**, 5075-86.

**Morris, J. K., Lin, W., Hauser, C., Marchuk, Y., Getman, D. and Lee, K. F.** (1999). Rescue of the cardiac defect in ErbB2 mutant mice reveals essential roles of ErbB2 in peripheral nervous system development. *Neuron* **23**, 273-83.

**Ono, F., Higashijima, S., Shcherbatko, A., Fetcho, J. R. and Brehm, P.** (2001). Paralytic zebrafish lacking acetylcholine receptors fail to localize rapsyn clusters to the synapse. *Journal of Neuroscience* **21**, 5439-48.

**Panzer, J. A., Gibbs, S. M., Dosch, R., Wagner, D., Mullins, M. C., Granato, M. and Balice-Gordon, R. J.** (2005). Neuromuscular synaptogenesis in wild-type and mutant zebrafish. *Dev Biol* **285**, 340-57.

**Panzer, J. A., Song, Y. and Balice-Gordon, R. J.** (2006). In vivo imaging of preferential motor axon outgrowth to and synaptogenesis at prepatterned acetylcholine receptor clusters in embryonic zebrafish skeletal muscle. *J Neurosci* **26**, 934-47.

**Role, L. W., Matossian, V. R., O'Brien, R. J. and Fischbach, G. D.** (1985). On the mechanism of acetylcholine receptor accumulation at newly formed synapses on chick myotubes. *J Neurosci* **5**, 2197-204.

**Rotundo, R. L.** (2003). Expression and localization of acetylcholinesterase at the neuromuscular junction. *J Neurocytol* **32**, 743-66.

**Saldanha, J., Singh, J. and Mahadevan, D.** (1998). Identification of a Frizzled-like cysteine rich domain in the extracellular region of developmental receptor tyrosine kinases. *Protein Sci* **7**, 1632-5.

**Sanes, J. R. and Lichtman, J. W.** (1999). Development of the vertebrate neuromuscular junction. *Annu Rev Neurosci* **22**, 389-442.

**Sanes, J. R. and Lichtman, J. W.** (2001). Induction, assembly, maturation and maintenance of a postsynaptic apparatus. *Nat Rev Neurosci* **2**, 791-805.

**Son, Y. J., Trachtenberg, J. T. and Thompson, W. J.** (1996). Schwann cells induce and guide sprouting and reinnervation of neuromuscular junctions. *Trends Neurosci* **19**, 280-5.

**Weatherbee, S. D., Anderson, K. V. and Niswander, L. A.** (2006). LDL-receptor-related protein 4 is crucial for formation of the neuromuscular junction. *Development* **133**, 4993-5000.

**Westerfield, M. and Eisen, J. S.** (1988). Neuromuscular specificity: pathfinding by identified motor growth cones in a vertebrate embryo. *Trends Neurosci* **11**, 18-22.

**Weston, C., Gordon, C., Teressa, G., Hod, E., Ren, X. D. and Prives, J.** (2003). Cooperative regulation by Rac and Rho of agrin-induced acetylcholine receptor clustering in muscle cells. *J Biol Chem* **278**, 6450-5.

**Yang, X., Arber, S., William, C., Li, L., Tanabe, Y., Jessell, T. M., Birchmeier, C. and Burden, S. J.** (2001). Patterning of muscle acetylcholine receptor gene expression in the absence of motor innervation. *Neuron* **30**, 399-410.

**Yang, X., Li, W., Prescott, E. D., Burden, S. J. and Wang, J. C.** (2000). DNA topoisomerase IIbeta and neural development. *Science* **287**, 131-4.

**Zhang, B., Luo, S., Wang, Q., Suzuki, T., Xiong, W. C. and Mei, L.** (2008). LRP4 serves as a coreceptor of agrin. *Neuron* **60**, 285-97.

**Zhang, J., Lefebvre, J. L., Zhao, S. and Granato, M.** (2004). Zebrafish unplugged reveals a role for muscle-specific kinase homologs in axonal pathway choice. *Nat Neurosci* **7**, 1303-9.

**Zhang, J., Malayaman, S., Davis, C. and Granato, M.** (2001). A dual role for the zebrafish unplugged gene in motor axon pathfinding and pharyngeal development. *Dev Biol* **240**, 560-73.

**Ziskind-Conhaim, L., Geffen, I. and Hall, Z. W.** (1984). Redistribution of acetylcholine receptors on developing rat myotubes. *J Neurosci* **4**, 2346-9.

# Chapter 2

## *In vivo* imaging of preferential motor axon outgrowth to and synaptogenesis at prepatterned acetylcholine receptor clusters in embryonic zebrafish skeletal muscle

This chapter is published in

The Journal of Neuroscience, January 18, 2006, 26(3):934-947

***In Vivo* Imaging of Preferential Motor Axon Outgrowth to and Synaptogenesis at Prepatterned Acetylcholine Receptor Clusters in Embryonic Zebrafish Skeletal Muscle**

Jessica A. Panzer, Yuanquan Song, and Rita J. Balice-Gordon

**Abstract**

Little is known about the spatial and temporal dynamics of pre- and postsynaptic specializations that culminate in synaptogenesis. Here we imaged presynaptic vesicle clusters in motor axons and postsynaptic acetylcholine receptor (AChR) clusters in embryonic zebrafish to study the earliest events in synaptogenesis *in vivo*. Prepatterned AChR clusters are present on muscle fibers in advance of motor axon outgrowth from the spinal cord. Motor axon growth cones and filopodia are selectively extended toward and contact prepatterned AChR clusters, followed by the rapid clustering of presynaptic vesicles and insertion of additional AChRs, hallmarks of synaptogenesis. All initially formed neuromuscular synapses contain AChRs that were inserted into the membrane at the time the prepattern is present. Examination of embryos in which AChRs were blocked or clustering is absent showed that neither receptor activity or receptor protein is required for these events to occur. Thus during initial synaptogenesis, postsynaptic differentiation precedes presynaptic differentiation, and prepatterned neurotransmitter clusters mark sites destined for synapse formation.

## Introduction

Neuronal circuitry becomes wired during development via mechanisms that direct axons to make synaptic connections with appropriate postsynaptic targets. However, the spatial and temporal dynamics of these events are poorly understood. Some studies have suggested that presynaptic differentiation precedes and initiates postsynaptic differentiation (Rao et al., 1998; Friedman et al., 2000; Okabe et al., 2001; Washbourne et al., 2002), whereas others have suggested that the opposite occurs (Cooper et al., 1992; Saito et al., 1992). These questions remain unresolved in large part because, to date, few studies have simultaneously imaged both presynaptic terminals and postsynaptic specializations *in vivo* (Javaherian and Cline, 2005), and none have examined the dynamism of both pre- and postsynaptic specializations simultaneously in living animals over time.

Neuromuscular synapses between motor neurons and muscle fibers have been used for studies of synaptogenesis in several invertebrate and vertebrate species (Sanes and Lichtman, 1999; Jin, 2002; Goda and Davis, 2003). Over the last 2 decades, studies of neuromuscular synaptogenesis in rodents, amphibians and fish have suggested that the clustering of postsynaptic acetylcholine receptors (AChRs) is induced by motor axon contact with muscle fibers by presynaptic release of the proteoglycan agrin and signaling through the tyrosine kinase receptor, MuSK, in the muscle fiber membrane (Sanes and Lichtman, 1999). In contrast, work in nerve-muscle cocultures has shown that small, non-synaptic AChR clusters were present in the absence of neurite contact. These clusters, however, were not targeted for innervation, but were dispersed and receptors

clustered *de novo* at sites of neurite contact with muscle fiber membranes (Fischbach and Cohen, 1973; Sytkowski et al., 1973; Anderson and Cohen, 1977; Frank and Fischbach, 1979; Bloch, 1988).

More recently, observations made in rodents during early stages of synaptogenesis and in mutant mice lacking motor neurons showed that, prior to and in the absence of innervation, AChR clusters are present on central region of muscle fibers (endplate band) through which the ingrowing nerve normally extends (Harris et al., 1981; Lupa and Hall, 1989; Morris et al., 1999; Feng et al., 2000; Yang et al., 2000; Lin et al., 2001; reviewed in Arber et al., 2002). We recently showed that AChR clusters are present in myotomal muscle of zebrafish, well before motor axons extend from the spinal cord (Panzer et al., 2005; see also Flanagan-Steet et al., 2005). Thus postsynaptic specializations are prepatterned in vertebrate muscles well in advance of innervation. Contrary to the prevailing belief that AChR clustering was dependent on the activation of a muscle-specific kinase (MuSK) via agrin released from motor axon growth cones (Sanes and Lichtman, 1999), in mice, prepatterned AChR clusters are formed in an agrin-independent, although MuSK-dependent fashion (Lin et al., 2001; Yang et al., 2001). Similarly, non-synaptic neurotransmitter receptor clusters are present on the dendrites and soma of CNS neurons prior to axon contact both *in vivo* and *in vitro* (Aoki et al., 1994; Rao et al., 1998; Washbourne et al., 2002). However, the fate of prepatterned neurotransmitter receptor clusters and their role in subsequent synaptogenesis remain poorly understood.

Here we report observations made using *in vivo* imaging of the spatial and temporal dynamics of motor axon growth cones and nascent terminals, and of the fate of prepatterned AChR clusters in zebrafish embryos. The optical transparency and rapid development of zebrafish embryos facilitate studies of neuromuscular synaptogenesis at developmental stages that are inaccessible in mammals. These observations show that motor axon growth cones preferentially contact prepatterned AChR clusters and form synapses at those sites. Thus, prepatterning of postsynaptic targets determines the spatial location of initial synaptogenesis in muscle, and may play a similar role during synaptogenesis in the CNS.

## Materials and Methods

### *Zebrafish strains*

Wild type, HuC:GFP (Park et al., 2000) and *sofa potato* (Ono et al., 2001) embryos were obtained from crosses between adult zebrafish. The HuC promoter drives GFP expression in all neurons, and was used here to visualize motor axons in some experiments.

### *Generation of transient transgenic embryos expressing VAMP-GFP*

A plasmid encoding UAS-VAMP2-GFP (Jontes et al., 2004) was co-injected with a plasmid encoding a-tubulin-GAL4 (7.5-15 ng/ml) in Yamamoto Ringers (in mM: 17 NaCl, 0.4 KCl, 0.27 $CaCl_2$, 0.5 Mg $Cl_2$, 2.4 $NaHCO_3$, pH 7.3 plus 0.05% Phenol red) into embryos at the 1-4 cell stage. Thus GAL4 activation of UAS drove VAMP2-GFP expression in all cells in a mosaic fashion. Embryos were then raised to 18-20 hours post fertilization (hpf) at 28.5° C in E3 medium (in mM: 5 NaCl, 0.17 KCl, 0.33 $CaCl_2$, 0.33 $MgSO_4$) and evaluated for GFP expression in the spinal cord. Embryos in which primary motor neurons were VAMP-GFP+ were selected for rhodamine a-bungarotoxin ($\alpha$BTX) staining and subsequent imaging as described below.

VAMP-GFP expression was observed in many types of neurons, including primary motor neurons CaP, MiP, RoP, and VaP. Motor neuron identity was determined by the location and size of the neuronal cell body and the territory innervated by the outgrowing motor axon (Myers et al., 1986), and was confirmed by post-imaging

immunostaining. Diffuse VAMP-GFP within axons and punctate VAMP-GFP clusters were observed in motor neuron axons, growth cones, and fine filopodia during early stages of axon outgrowth and synaptogenesis, as previously reported for VAMP-GFP and other synaptic vesicle proteins during early neural development (Sabo and McAllister, 2003; Jontes et al., 2004). Colocalization of VAMP-GFP with the synaptic vesicle protein SV2 after immunostaining (see immunostaining section below) confirms that VAMP-GFP accurately marks the location of synaptic vesicle clusters in zebrafish (Supplemental Fig. 1A; (Panzer et al., 2005)). In addition, VAMP-GFP expression did not affect motor axon outgrowth or synaptogenesis (Supplemental Fig. 1B).

*Fluorescent αBTX staining in live embryos*

At ca. 18-24 hpf, wild type, HuC:GFP or transient transgenic embryos were briefly anesthetized in 0.02% Tricaine (Sigma, St. Louis, MO) in Hank's solution (in mM: 137 NaCl, 5.4 KCl, 0.25 mM $Na_2HPO_4$, 0.44 $KH_2PO_4$, 1.3 $CaCl_2$, 1.0 $MgSO_4$, 4.2 $NaHCO_3$). The most caudal 1 to 2 segments of the tail were removed using a scalpel. Embryos were rinsed in Hank's solution, and incubated in rhodamine αBTX (15 mg/ml; Molecular Probes, Eugene, OR) for 1.5 hours at room temperature followed by extensive washing in Hank's solution. We empirically determined that this αBTX staining protocol resulted in labeling of AChRs that was optically saturating but non-paralytic. Absence of paralysis was determined by normal response of embryos to head or tail tap. Optical saturation of AChRs was defined as failure of Cy5 αBTX, applied immediately after the initial rhodamine αBTX application, to result in Cy5 αBTX labeling of receptors that

could be detected optically, even with the highest gain settings of the confocal photomultiplier tube. Optically saturating but non-paralytic labeling of AChR receptors did not significantly alter motor axon outgrowth or neuromuscular synapse formation. Embryos were then rinsed with Hank's solution prior to imaging. Using this technique, AChRs inserted into the muscle fiber membrane after αBTX application are unlabeled, and therefore not detectable during *in vivo* imaging.

To examine the localization of newly inserted receptors, in one series of experiments, the location of AChRs that were inserted in the muscle fiber membrane at the time of initial rhodamine αBTX labeling (old AChRs) was compared to the location of subsequently inserted AChRs (new AChRs) that were labeled with Cy5 αBTX after a 2, 4 or 7 hour delay. Embryos were then processed for immunostaining.

*In vivo imaging*

Embryos were placed in 1.2% low melting temperature agarose (SeaPlaque; Cambrex) in Hank's solution in a modified imaging chamber (Warner Instrument Co.) perfused with Hank's solution at 28.5 °C. In transient transgenic VAMP-GFP embryos, confocal z-stacks of images were obtained approximately every 10-20 minutes for 2-8 hours (Leica TCS 4D or SP2 system). In HuC:GFP embryos, confocal z-stacks were obtained every 1 hour for 6 hours. Unless otherwise stated, each movie panel is a single plane projection of a z-stack of 20-60 1 μm thick planes taken at the indicated time interval. Z-stacks of up to 60 microns were necessary in some embryos because the initial path of outgrowing motor axons is not flat and because, in older embryos, motor axon arbors becomes elaborate in three dimensions (c.f. Fig. 1, Panzer et al. (2005)).

Spontaneous movements and blood cell circulation, indicators of embryo viability, were observed throughout the duration of movies that were subsequently analyzed. At the conclusion of the imaging session, embryos were re-anesthetized, fixed and processed for immunostaining.

In transient transgenic embryos expressing VAMP-GFP at ca. 24 hpf, relatively few motor axon branches or neuromuscular synapses are present, whereas by 72 hpf axons have branched into their appropriate, cell specific territory and many neuromuscular synapses are present (Supplemental Fig. 1C). *In vivo* imaging of VAMP-GFP+ primary motor neurons showed that motor axons were extended at a rate of 10.1 ± 0.8 μm / hour (mean ± s.e.m; N = 10 22-30 hpf embryos, 10 neurons), similar to that observed in previous *in vivo* analyses using single cell fills (Eisen et al., 1986; Myers et al., 1986; Westerfield et al., 1986). Thus the imaging procedures used in the present study do not interfere with axon outgrowth or neuromuscular synaptogenesis.

*AChR blockade*

Rhodamine αBTX was diluted to 0.25 mM in Yamamoto Ringers with 0.05% Phenol red and injected directly into the yolk of 12-14 hpf embryos (Lefevre et al., 2004). This approach was used to achieve sustained paralysis, since it likely achieves a higher concentration of αBTX within embryonic muscle than bath application does, both by bypassing the skin, a natural barrier to toxins, and by providing sustained exposure to αBTX released by the yolk sac over many hours. At 24 hpf, embryos were scored for

motility by evaluating responses to head and tail tap, and only those embryos that were completely paralyzed were collected, fixed and immunostained.

*Sodium channel blockade*

Embryos were raised from 10 to 21 hpf in 0.01% tricaine in E3. At 21 hpf, embryos were scored for motility by evaluating spontaneous tail movements, and only those embryos that were completely immotile were collected, fixed and immunostained.

*Whole mount immunostaining of zebrafish embryos*

Embryos were anesthetized, fixed and immunostained as described previously (Panzer et al., 2005) using antibodies against SV2 (Developmental Studies Hybridoma Bank (DSHB)) and/or GFP (Chemicon, Inc.) and a fluorescently conjugated secondary antibody (Jackson Labs, Inc.). Immunostained embryos were examined using confocal microscopy. Unless otherwise stated, each figure panel showing immunostaining is a single plane projection of a z-stack of 20-60 1 μm thick planes.

*Analyses of prepatterned AChR clusters, presynaptic vesicle clusters and synapse formation*

AChR or presynaptic vesicle cluster number and area were measured from single plane projections of confocal image stacks using interactive software (Metamorph, Molecular Dynamics, Inc.). The number and intensity of pixels in a line parallel to the

longest axis of a cluster were measured to analyze changes in AChR cluster length and intensity over time. Pre- and postsynaptic clusters were scored as synapses if there was at least 30% pixel overlap between presynaptic and postsynaptic labeling.

To quantify the contribution of prepatterned AChR clusters to synapses, each cluster present in the first frame of a time lapse movie was analyzed and placed into one of three categories: Present but subsequently disappeared; present with a VAMP-GFP+ cluster overlying at least 30% of the AChR cluster, and thus innervated (synaptic); and present throughout the movie but not innervated during the imaging interval (non-synaptic). Preliminary analyses suggested that the 30% colocalization criteria is the minimum for reliable identification of a synapse at the early embryonic ages examined here (see also Panzer et al., 2005). Synapses were confirmed after subsequent immunostaining of presynaptic vesicles with antibodies against SV2. The percentage of events in which an AChR cluster was present in advance of a presynaptic vesicle cluster and in which a presynaptic vesicle cluster was present followed by appearance of an AChR cluster was also determined.

*Quantification of growth cone and filopodia dynamics*

To quantify axon and growth cone outgrowth with respect to prepatterned AChR clusters, the position of a growth cone was determined from a point in its geometric center. The closest AChR cluster in advance of the growth cone was defined as a potential target AChR cluster. Three angles were then measured: angle 1, the angle between the actual growth cone trajectory and the AChR cluster; angle 2, the angle

between the actual trajectory and the initial trajectory if the growth cone were to grow in a straight line; and angle 3, the angle between the initial trajectory and the target AChR cluster (see Fig. 3D). The distribution of angles 1 and 2 was evaluated, and the relationship between angle 2 and angle 3 was analyzed by linear regression. In some cases, more than one time interval of axon outgrowth was analyzed per neuron, and this number is reported as an outgrowth event.

To quantify the direction of filopodial extension with respect to prepatterned AChR clusters, only filopodia extended near AChR clusters that were not along the direct path of axon extension were analyzed. This is because we wished to avoid a bias in the quantification that would have arisen if filopodia tended to grow out in the direction of axon extension, and AChR clusters happened to be along this pathway. All filopodia within a 5 μm radius of an axon or growth cone region nearest the target AChR cluster were analyzed. The mean distance from an axon or growth cone to a target AChR cluster was 15 μm. The presence of multiple AChR clusters that were an equal distance from an axon or filopodia was rare, and these cases were not analyzed.

The length of the filopodia, the actual trajectory of the filopodia and the straightest, shortest trajectory between the base of the filopodia at the axon and an AChR cluster were determined in each movie frame (see Fig. 4D). The length of the filopodia and the angle between its actual trajectory and the straightest trajectory with respect to an AChR cluster were plotted using polar coordinates where each line segment represents filopodia length. Similarly, the length of filopodia, and the angles between the filopodia and a control region, defined as an area 15 μm from an axon or growth cone with no

AChR clusters in the vicinity were also measured and plotted. The cumulative percent of filopodia extended at various angles with respect to an AChR cluster or control region was plotted and differences assessed (Komolgorov-Smirnoff test).

**Acknowledgements**

We thank A. Kugath, M. Scott and H.-Y. Zhou for technical assistance, Dr. P. Brehm for providing heterozygous carriers of the *sofa potato* mutation, Dr. S. Smith for providing the UAS-VAMP-GFP construct, and Dr. S. Gibbs for helpful discussions. Supported by grants from the NIH to R. B. G. (NS45919, NS50524) and a Howard Hughes Medical Institute predoctoral fellowship to J. A. P.

## Results

*Prepatterned AChR clusters are dynamic*

Each of the three primary motor neurons per spinal cord hemisegment (CaP, MiP, and RoP) sends an axon out of the spinal cord between 16-24 hours post-fertilization (hpf). Primary motor axons then grow ventrally along the lateral surface of the notochord to the so-called choice point at the horizontal myosepta (midline) of the somite. Axons pause at the choice point for several hours, then grow out across the medial surface (CaP, MiP), or branch near the midline (RoP, VaP) of the myotome, and subsequently all axons branch extensively (Eisen et al., 1986). Neuromuscular synapses are formed en passant along the axon shaft and branches (Eisen et al., 1986; Myers et al., 1986; Westerfield et al., 1986; Panzer et al., 2005). Approximately 5 hours after initiation of primary motor axon outgrowth, the axons of secondary motor axons (ca. 20-30 per hemisegment) begin to extend into the periphery along the pathways pioneered by primary motor axons and also form en passant synapses (Myers et al., 1986; Westerfield et al., 1986).

In fixed and immunostained embryos at 24 hpf, AChR clusters are present on each muscle fiber along the medial surface of the myotome (Fig. 1A, caudal most segments, Fig. 1D), on many muscle fibers in lateral muscle layers, and along the lateral myosepta, well in advance of motor axon outgrowth from the spinal cord (Panzer et al., 2005). These AChR clusters are thus prepatterned on muscle fibers in advance of innervation (Yang et al., 2000; Lin et al., 2001; Yang et al., 2001). Prepatterned AChR clusters are elongated and diffuse in caudal and thus younger myotomes, but are small, punctate, and reduced in number in more rostral, older myotomes (Fig. 1A-D). The

largest prepatterned AChR clusters are present at the choice point; these clusters persist as motor axons enter the myotome and the first neuromuscular synapses are made at these prepatterned AChR clusters (Fig. 1B, bracket; Panzer et al., 2005). These observations suggest that initially diffuse, elongated prepatterned AChR clusters coalesce, and some AChR clusters disappear, as innervation occurs.

To directly determine the fate of prepatterned AChR clusters as motor axons grow into the myotome, AChRs were labeled with a non-paralyzing dose of rhodamine αBTX in HuC:GFP embryos, in which all neurons including primary motor neurons and axons express GFP, and confocal z-stacks were obtained over time (N = 4 20-26 hpf embryos, 19 myotome segments). At the beginning of imaging, motor axons had not exited the spinal cord (Fig. 2A, panel 0:00). Prepatterned AChR clusters are initially elongated and diffuse, and over several hours, most if not all clusters coalesce (Fig. 2A; compare panel 1:00 with panel 3:00). During a 6 hour interval, AChR cluster width is reduced (Fig. 2F) and fluorescence intensity increases (Fig. 2G), consistent with the coalescing of each cluster. During this interval, 20% of all prepatterned AChR clusters disappear, as demonstrated both by comparing subsequent images qualitatively (Fig. 2B, arrow) as well as quantifying changes in individual cluster length and intensity (Fig. 2C, F-H). This dynamic redistribution of AChRs usually begins in advance of motor axon outgrowth into the myotome. Thirty percent of all prepatterned AChR clusters persist and become innervated during a 6 hour interval (Fig. 2D, arrow), as demonstrated by the presence of GFP+ axons apposed to AChR clusters (Fig. 2D, panel 5:00, asterisk) as well as by post-imaging immunostaining for presynaptic vesicles (Fig. 2D, last panel). As stated above, 20% of prepatterned AChR clusters that are not innervated disappear.

However, about half of the prepatterned AChR clusters are neither dispersed nor innervated during a 6 hour imaging interval. Given the absence of uninnervated AChR clusters in older embryos (Panzer et al., 2005), these clusters must either be innervated or disappear over longer intervals. These observations show that prepatterned AChR clusters are highly dynamic before and during motor axon outgrowth into the myotome, and that some of these clusters are incorporated into synapses, whereas others are dispersed or persist in an uninnervated state.

*Motor axon outgrowth occurs along prepatterned AChR clusters*

*In vivo* imaging of VAMP-GFP+ primary motor axon outgrowth in transiently transgenic embryos was used to examine the spatial and temporal dynamics of these events with respect to prepatterned AChR clusters over time (N = 20 20-30 hpf embryos, 29 growth cones, 44 outgrowth events). *In vivo* imaging showed that, at any given time, AChR clusters are observed in advance, or within 2-3 muscle fibers, of ca. 75% (33 / 44) of outgrowing motor axons (c.f. Fig. 1C; Fig. 3A; Fig. 4A; Fig. 6A, E). Motor axon growth cones grow directly towards, then along and eventually innervate, prepatterned AChR clusters (Fig. 3B). Continual growth towards, and innervation of, prepatterned AChR clusters result in motor axon extension across the medial surface of the myotome (Fig. 3B). Thus, motor axons appear to follow a pathway across the medial surface of the myotome that is spatially coincident with prepatterned AChR clusters. These results contrast with previous reports that AChR clustering and motor axon outgrowth are simultaneous in zebrafish (Luo and Westerfield, 1992), and raise the possibility that, in at

least some cases, prepatterned AChR clusters themselves, or cues that are co-patterned with such clusters, might direct motor axon outgrowth.

These possibilities are further supported by the observation that the location of prepatterned AChR clusters predicts growth cone turning. For example, in Fig. 3B, prepatterned, previously uncontacted, AChR clusters are located ca. 15 μm rostral (and somewhat lateral) to the motor axon growth cone in panel 2:20, and in the subsequent 2 hours, the growth cone turns 65° toward and contacts these AChR clusters. Sixty-three percent of growth cones are extended with an angle ≤ 10º, and 95% are extended at an angle of ≤ 30º, with respect to a prepatterned, previously uncontacted, AChR cluster (Fig. 3E, black bars). Growth cones were observed to turn toward a prepatterned AChR cluster over a wide range of angles, from 10º to 130º (Fig. 3E, grey bars). For the population of growth cones that were observed over time, a significant correlation exists between the location of a prepatterned AChR cluster with respect to the motor axon's initial trajectory, and the angle that the growth cone eventually turns toward that cluster (Fig. 3F). These observations show that the direction of motor axon outgrowth is dynamically altered so that axons continually extend along a pathway that is spatially coincident with prepatterned AChR clusters that they will eventually contact.

*Motor axon filopodia are preferentially extended toward prepatterned AChR clusters*

In the course of time lapse imaging of motor axon outgrowth to, and interactions with, prepatterned AChR clusters, many examples were observed of filopodia that were

rapidly extended toward and touched prepatterned AChR clusters (Fig. 4A-C). In some cases, filopodia were extended toward a prepatterned AChR cluster (Fig. 4B, arrow), touched it (Fig. 4B, panels 0:10 and 3:30, asterisk), and retracted. In other cases, filopodia were observed that contacted a prepatterned AChR cluster (Fig. 4C, arrowhead), dilated (Fig. 4C, panel 4:20), and subsequently persisted as an axon branch for the duration of the imaging interval (Fig. 4C, panel 5:10).

Quantitative analyses showed that filopodia were preferentially extended toward prepatterned AChR clusters. When the direction of all of the filopodia extended from a single motor axon was plotted using polar coordinates, the majority were extended $\leq 30°$ with respect to a target prepatterned AChR cluster (Fig. 4E). In contrast, when the direction of filopodial extension was analyzed with respect to a control region without an AChR cluster in the vicinity, extension was random (Fig. 4F). For all filopodia from all motor neurons imaged over time, approximately 30% of filopodia were extended at an angle $\leq 10°$ with respect to a prepatterned AChR cluster located a mean of 15 μm away, and 54% of filopodia were extended at an angle $\leq 30°$ of such clusters (Fig. 4G, gray line). In contrast, when no AChR cluster was present, filopodia extension was non-directional (Fig. 4G, black line). These results show that motor axon filopodia are preferentially extended toward prepatterned AChR clusters.

Time lapse imaging demonstrated that filopodia are not extended with equal frequency from all areas of the motor axon. The majority of filopodia (90%) were extended from axon locations that contained VAMP-GFP+ clusters of synaptic vesicles. 70% of the VAMP-GFP+ clusters from which filopodia extended were also apposed to

AChR clusters (63% of all filopodia) and were thus synaptic sites (Fig. 5A-A", D). Only 10% of filopodia were extended from locations on the axon shaft that lacked VAMP-GFP+ clusters (Fig. 5C-C", D). These results show that filopodia are preferentially extended from synaptic sites on axons, consistent with observations of axon branch formation in *Xenopus laevis* tadpoles (Javaherian and Cline, 2005).

*Prepatterned AChR clusters determine the location of initial neuromuscular synapses*

The results described above show that prepatterned AChR clusters play an important role in determining the direction of motor axon outgrowth. We next asked whether initial neuromuscular synapses are established at prepatterned AChR clusters (N = 19 20-30 hpf embryos, 34 motor neurons, 75 synapse formation events).

In 81% of synapse formation events, a motor axon growth cone or filopodia was observed to reach a prepatterned AChR cluster and subsequently extend beyond it. In these cases, a VAMP-GFP+ cluster, at least 2 μm in length, was subsequently formed over the AChR cluster (Fig. 6A, E). The formation of VAMP-GFP+ clusters occurred rapidly, within 20 minutes to 1.5 hours after contact (Fig. 6B, panel 1:00; 6F, panel 4:00, asterisk) and persisted for several hours, or until the end of the imaging session (Fig. 6B, panel 1:40; 6F 4:40). These results show that in ca. 80% of cases, clustering of presynaptic material, a requisite step in neuromuscular synapse formation, occurs at prepatterned AChR clusters.

In 11% of synapse formation events, a motor axon growth cone or filopodia was observed that had extended over one or more AChR clusters at the beginning of the imaging session. In these cases, we were unable to establish whether AChR clusters were indeed prepatterned, i.e., present prior to motor axon contact. However, in these cases VAMP-GFP+ clusters subsequently appeared over AChR clusters (see Fig. 3B, panel 0:40, asterisks). Taken together with the results above, theses results indicate that in ca. 90% of cases, AChR clusters are present prior to clustering of VAMP.

Prior to ca. 24 hpf, in only 5% of events did motor axons appear to initiate neuromuscular synaptogenesis. In these cases, a motor axon or growth cone was present first, followed by the appearance of an AChR cluster (Fig. 6F, G, arrowhead), and subsequently, a VAMP-GFP+ cluster appeared at this site (Fig. 6F, panel 4:40, empty arrowhead). In 2/75 events (3%), VAMP-GFP+ and AChR clusters appeared simultaneously (data not shown). Out of 75 synapses formation events, VAMP-GFP+ clusters were never observed to form prior to AChR clustering. Together with synapse formation at prepatterned AChR clusters, these results show that, in the vast majority of cases of initial synaptogenesis in muscle, postsynaptic AChR clusters are formed before presynaptic clusters of synaptic vesicles accumulate.

*Redistribution of AChRs from prepatterned clusters and preferential insertion of new receptors at synaptic sites*

To determine the location of newly inserted AChRs during initial stages of synaptogenesis, all AChRs were optically saturated with rhodamine αBTX at 20 hpf, and 2, 4 or 7 hours later, newly inserted AChRs were labeled with Cy5 αBTX. The location of existing (old) AChRs and receptors inserted since the initial rhodamine αBTX labeling (new) was compared to the location of motor axons and terminals visualized after immunostaining.

After a 2-4 hour interval after initial labeling of old AChRs, all prepatterned AChRs coalesced and some disappeared, consistent with immunostaining and *in vivo* imaging observations (compare Fig. 7A' with 7B'). Moreover, the majority of AChR clusters beneath SV2+ terminals, and thus at synapses, were composed of both old and new AChRs (Fig. 7A-B"), while the majority of non-synaptic sites (Fig. 7B, arrows) were composed only of old AChRs (Fig. 7D). Few if any AChR clusters are observed that contain only newly inserted AChRs (Fig. 7B", D). This result suggests that new AChRs are preferentially inserted at synapses and not at sites of non-synaptic AChR clusters.

Strikingly, after a 7 hour interval, old AChRs labeled at 20 hpf were observed to be located in clusters beneath presynaptic nerve terminals throughout the myotome (compare Fig. 7A, A', B, B' to C, C'). This observation suggests that, even though some prepatterned AChR clusters disappear, receptors in those clusters may be re-clustered beneath synapses (Fig. 7C, C'). We cannot rule out the possibility that some old AChRs contained within synaptic clusters at 27 hpf may have been originally diffusely distributed in the muscle membrane at 20 hpf and not present in prepatterned clusters *per se*. Moreover, *in vivo* imaging observations showed that non-synaptic AChR clusters,

containing old AChRs labeled several hours earlier, occasionally appeared on muscle fibers 10-20 microns in advance of or beneath motor axons or growth cones (data not shown, see Fig. 6F, G). Thus, some non-synaptic AChR clusters are primarily formed via redistribution of AChRs that were in the membrane at an earlier time. These data show that AChRs that are present in the muscle fiber membrane prior to motor axon outgrowth into the myotome are redistributed, such that all synapses formed by 27 hpf contain at least some of this original population of receptors.

*AChR activity or AChR clusters are not required for initial neuromuscular synaptogenesis*

In mouse, both presynaptic release of ACh and the depolarization of muscle fibers have been proposed as signals that lead to the dispersion of prepatterned AChR clusters and their redistribution beneath nascent motor nerve terminals (Lin et al., 2001; Yang et al., 2001; Misgeld et al., 2002; Lin et al., 2005). Moreover, given that growth cones and filopodia are preferentially extended toward prepatterned AChR clusters, we wondered whether AChRs might detect presynaptic ACh release, leading to signaling that culminated in synapse formation. These possibilities were tested by examining prepatterned AChR clusters, motor axon outgrowth and neuromuscular synapse formation in wild type zebrafish in which AChRs were blocked with αBTX from 12-24 hpf.

In caudal and thus younger segments of paralyzed embryos at 24 hpf, the number and total area of prepatterned AChR clusters, and the dispersion of some prepatterned AChR clusters, were similar to control embryos (Fig. 8A", B", G). Thus AChR activity is not required for the formation or dispersion of prepatterned AChR clusters.

In both rostral (Fig. 8A, B) and middle (Fig. 8A', B') segments, the outgrowth of primary motor neurons is similar in paralyzed and control embryos (Fig. 8D). Moreover, the number and total area of SV2+ presynaptic vesicle clusters, postsynaptic AChR clusters and of synapses are similar (Fig. 8E), although the distribution of areas of individual SV2+ clusters was shifted to larger values in paralyzed compared to control embryos (Fig. 8F), probably reflecting enlargement of the 3-4 choice point synapses in some myotomes.

In addition to using αBTX to block signaling through AChRs, we also blocked activity with the sodium channel blocker tricaine and found that prepatterned AChR cluster dispersal and motor axon outgrowth were similarly unaffected (Supp. Fig. 2). Blockade of sodium channels with tetrodotoxin (TTX) provided similar results (data not shown). Consistent with previous work in zebrafish, chicken and rodents, these results show that neither AChR activity nor neuronal activity is required for motor axon outgrowth or initial neuromuscular synapse formation.

Although only those embryos that were completely paralyzed following αBTX application were selected for analysis in the above experiments, it remains possible that this technique might not completely abolish signaling through AChRs. Thus, we next examined neuromuscular synaptogenesis in *sofa potato* (*sop*) mutants, in which AChRs

are absent due to a mutation in the AChR d subunit (Ono et al., 2001). As reported previously, no AChR clusters were observed in *sop* mutant embryos (Fig. 8C-C"; (Ono et al., 2001)). Moreover, at 24 hpf, the extent of primary motor axon outgrowth is similar between *sop* mutants and normal siblings (Fig. 8D). However, in many segments, the first formed presynaptic SV2+ vesicle clusters, at the choice point, are enlarged in *sop* mutant embryos compared to normal siblings (Fig. 8A, C, brackets). While the number and total area of SV2+ vesicle clusters are similar (Fig. 8E), the distribution of individual SV2+ cluster area was shifted to larger values in *sop* mutant compared to normal siblings (Fig. 8F), probably reflecting the enlargement of the 3-4 presynaptic terminals at the choice point in each myotome. Taken together with the results of αBTX blockade, these experiments suggest that, perhaps via a negative feedback loop, AChR signaling limits the size of presynaptic vesicle clusters. However, it is clear from these experiments that AChR activity, and indeed AChRs themselves, are dispensable for motor axon outgrowth. Thus, it may be that cues colocalized with prepatterned AChR clusters, but not the receptors themselves, determine motor axon outgrowth, branching and initial neuromuscular synaptogenesis.

**Discussion**

The observations we report here provide fundamentally new insights into the initial steps of synapse formation. We show that AChR clusters are prepatterned in myotomal muscle prior to motor axon outgrowth from the spinal cord, and that prepatterned AChR clusters are localized to the pathway of motor axon outgrowth along the myotome. Moreover, motor axon growth cones and filopodia are preferentially extended toward and contact prepatterned AChR clusters. After contact, presynaptic vesicles cluster at these sites, resulting in the formation of neuromuscular synapses. AChR blockade and examination of *sop* AChR mutants showed that neither receptor activity or receptor protein is required for these events to occur. Thus cues that are colocalized with prepatterned AChR clusters, but not the clusters themselves, must regulate motor axon outgrowth, branching and initial neuromuscular synaptogenesis.

Complementary work in zebrafish to that reported here was recently published (Flanagan-Steet et al., 2005). Flanagan-Steet et al. used time lapse imaging to show that prepatterned AChR clusters on adaxial slow muscle fibers are incorporated into neuromuscular synapses as axons advance. In a transgenic line in which motor axon outgrowth occasionally did not occur normally, axons were observed to be required for the subsequent stabilization of prepatterned AChR clusters. Together, these studies show that postsynaptic differentiation precedes presynaptic differentiation and that the formation of initial postsynaptic specializations does not require motor axons (see also Panzer et al., 2004). Conversely, initial motor axon outgrowth and clustering of presynaptic vesicles does not require AChR activity or protein. Thus while work in

zebrafish (Zhang et al., 2004) and mice (Lin et al., 2001; Yang et al., 2001) shows that MuSK is required for the formation of prepatterned AChR clusters, cell-cell signals that are colocalized with prepatterned AChR clusters mediate initial neuromuscular synaptogenesis.

*Formation and fate of prepatterned AChR clusters*

Our previous observations in zebrafish embryos showed that initially diffuse, elongated prepatterned AChR clusters are present throughout the myotome prior to motor axon outgrowth from the spinal cord (Panzer et al., 2005). The mechanism by which AChRs are clustered in the absence of innervation has been the subject of much speculation. Prepatterned AChR clusters are able to form in mice lacking motor neurons and thus muscle fiber innervation, as well as in mice lacking agrin, but do not form in mice lacking MuSK or rapsyn (Lin et al., 2001; Burden, 2002). Thus MuSK signaling may be activated independently of agrin, perhaps by an alternate, muscle derived ligand, in order to establish prepatterned AChRs. Alternatively, sufficient MuSK activation that leads to the formation of prepatterned AChR clusters might not require ligand binding. In the absence of agrin, MuSK is active at low levels (Gillespie et al., 1996; Apel et al., 1997; Watty et al., 2000) and activated MuSK can recruit and cluster additional MuSK molecules (Jones et al., 1999). Thus, prepatterned AChR clusters may be formed by early expression and activation of MuSK in muscle fibers.

Initially diffuse prepatterned AChR clusters then coalesce and become more punctate. Some clusters are innervated, whereas others are not. Many of the

uninnervated AChR clusters disappear, while others persist for at least several hours. Interestingly, all neuromuscular synapses present at the completion of motor axon outgrowth across the myotome contain AChRs that can be labeled at the time of the original prepattern. This result suggests that AChRs from dispersed clusters may, in fact, be redistributed and eventually incorporated into newly formed synapses. It is unclear why many uninnervated AChR clusters are dispersed, whereas others persist uninnervated for at least several hours. Previous studies have suggested that prepatterned clusters are dispersed in a neuron and activity dependent manner, and that AChRs are subsequently reclustered beneath nascent motor nerve terminals via agrin-MuSK signaling (Misgeld et al., 2002; Brandon et al., 2003). In mice, AChR clusters are larger and more numerous in the absence of motor axons or in the absence of motor axons and agrin (Yang et al., 2001), compared to the absence of agrin alone (Lin et al., 2001; Lin et al., 2005). This suggests that axons may provide signals that disperse AChR clusters that are not stabilized by agrin (Lin et al., 2001; Yang et al., 2001; Lin et al., 2005; Misgeld et al., 2005). One such signal has been proposed to be presynaptic ACh release. In mutant mice lacking choline acetyltransferase and thus ACh release, neuromuscular synapses are distributed over a wider region of the muscle compared to wild type littermates (Misgeld et al., 2002; Brandon et al., 2003). This suggests that ACh release may lead to the dispersion of prepatterned AChR clusters. In recent work in which neuromuscular synapses were examined in mutant mice lacking agrin and choline acetyltransferase, synapses formed normally in the absence of agrin and ACh release. This suggested that ACh destabilizes postsynaptic AChR clusters, and that agrin counteracts this action, functioning as an anti-declustering signal. (Misgeld et al., 2005; see also Lin et al., 2005).

However, our results show that, in zebrafish, AChR blockade with αBTX does not affect prepatterned AChR cluster number, size or incorporation into synapses. In addition, blockade of activity with tricaine or TTX does not affect overall neuromuscular synaptogenesis. Thus, although presynaptic synthesis of ACh has been shown to be necessary for normal neuromuscular synapse formation in mice (Misgeld et al., 2002, 2005; Brandon et al., 2003, Lin et al., 2005), AChR mediated signaling and activity may not be essential for these early events in zebrafish.

*Motor axon growth cones and filopodia preferentially contact prepatterned AChR clusters*

Previous work *in vitro* showed that motor axon growth cones do not preferentially contact preexisting AChR clusters, but rather these are dispersed and new clusters are induced (Anderson and Cohen, 1977; Frank and Fischbach, 1979). We observed that motor axon growth cones and filopodia are preferentially extended toward prepatterned receptor clusters, demonstrating that the initial contact between motor axon growth cones and prepatterned receptor clusters is not random. Our observations further show that such receptor clusters are targeted by motor axons for subsequent synapse formation, because presynaptic synaptic vesicle clusters subsequently formed over prepatterned AChR clusters. As motor axon growth cones have been shown to release ACh *in vivo* (Hume et al., 1983), the fact that presynaptic terminals are formed over prepatterned AChR clusters would allow for synaptic transmission to begin rapidly after pre- and postsynaptic contact.

Our results show that motor axon outgrowth and neuromuscular synaptogenesis are not altered when AChRs are blocked or absent. This suggests that signaling through postsynaptic AChRs is not required for these events to occur. Similar results have been obtained in *nic-1* mutant zebrafish that lack AChRs (Westerfield et al., 1990) and in *twitch once* mutants in which rapsyn is defective and AChRs do not cluster (Ono et al., 2002). It seems likely that other cues are necessary to attract motor axon growth cones and filopodia, and our data suggest that such cues are patterned appropriately in the absence of AChR activity and in the complete absence of AChR clusters. One obvious candidate is MuSK or a downstream signaling component. In mouse, MuSK has been shown to be colocalized with prepatterned AChR clusters (Burden, 2002), and defects in motor axon outgrowth, branching and initial neuromuscular synaptogenesis are observed in MuSK mutant mice (Sanes and Lichtman, 1999) and in *unplugged* mutant zebrafish in which the zebrafish MuSK homolog is absent (Zhang et al., 2004). Alternatively, motor axon pathfinding might not require MuSK itself, but rather one of the many signaling components downstream of MuSK activation.

One might also argue that motor axon pathfinding is pre-programmed and that the muscle prepatterning reported here might simply be coincident with the future path of motor axons, but neither critical nor instructive. Given the precise contacts we observe between motor axon growth cones, their filopodia, and prepatterned AChR clusters, we feel that this explanation is highly unlikely. In addition, work from several groups supports the existence of prepatterned cues in muscle fibers that instruct motor axon pathfinding decisions (c.f. Zeller et al., 2002; Zhang et al., 2004). The striking pathfinding abnormalities in the zebrafish *unplugged* mutant further support the idea that

signaling molecules co-patterned with AChR clusters might play a key role in shaping the innervation of myotomal muscles (Zhang et al., 2004).

*Temporal order of synapse assembly*

The temporal order of pre- and postsynaptic differentiation during synaptogenesis has been the subject of much debate, largely because, to date, the imaging analyses required to definitively address these questions have not been performed *in vivo*. In zebrafish, previous time lapse observations *in vivo* have suggested that AChRs are clustered after motor axon contact, but these data have limited optical and temporal resolution (Liu and Westerfield, 1992). There is no evidence that motor axons extend into the myotome, induce AChR clusters and then retract, growing out again at later times (Liu and Westerfield, 1992; Zhang et al., 2004; Flanagan-Steet et al., 2005). Although we do observe rare instances where motor axon filopodia appear to induce AChR clusters, these represent a small minority of initial neuromuscular synapse formation events. This remains true even when the dynamics of this process are examined at finer temporal resolution than reported here (Y. Song, J. Panzer and R. Balice-Gordon, unpublished observations). Thus, it seems unlikely that axons or filopodia that might initially induce AChR clusters were underestimated. Rather, our data indicate that postsynaptic muscle fibers, by virtue of the existence of cues prepatterned with AChR clusters, determine the spatial location of initial synapses, and that postsynaptic AChR clustering temporally precedes synaptic vesicle clustering during initial synaptogenesis. It is likely that the accumulation of synaptic vesicles over AChR clusters represents the

formation of a functional synapse, as motor axon growth cones containing synaptic vesicles have been shown to release ACh *in vivo* (Hume et al., 1983). Future studies are required to confirm active vesicle cycling at these early synapses using, for example, genetically encoded markers of exocytosis, and to determine the order of accumulation of other additional synaptic components pre- and postsynaptically.

Although AChR clustering temporally precedes synaptic vesicle clustering during initial synaptogenesis, at later stages of synaptogenesis, presynaptic axons probably also induce additional postsynaptic AChR clusters, because the total number of neuromuscular synapses present at 72 hpf is larger than the number of prepatterned AChR clusters initially present. Thus there may be two distinct modes of synaptogenesis. In the first mode, initial synapses are formed at sites that contain preexisting neurotransmitter receptor clusters. In a second and possibly contemporaneous mode, additional synapses are formed by the clustering of receptors beneath presynaptic nerve terminals (Flanagan-Steet et al., 2005). In skeletal muscle, these latter events are mediated by agrin-MuSK and other signaling (Sanes and Lichtman, 1999). In the CNS, most studies in culture have indicated that presynaptic differentiation precedes and may initiate postsynaptic differentiation (Rao et al., 1998; Friedman et al., 2000; Okabe et al., 2001; Washbourne et al., 2002; Bresler et al., 2004). Clearly, additional experiments are necessary *in vitro* as well as *in vivo* to resolve these issues in the CNS and to determine whether one or both modes of synapse formation do indeed occur. That prepatterning of postsynaptic targets plays a previously unappreciated and important role in neuromuscular synaptogenesis suggests this process may also be important during CNS synaptogenesis, and thus be a general mechanism that shapes neural circuitry during

development.

**References**

Anderson MJ, Cohen MW (1977) Nerve-induced and spontaneous redistribution of acetylcholine receptors on cultured muscle cells. J Physiol 268:757-773.

Aoki C, Venkatesan C, Go CG, Mong JA, Dawson TM (1994) Cellular and subcellular localization of NMDA-R1 subunit immunoreactivity in the visual cortex of adult and neonatal rats. J Neurosci 14:5202-5222.

Apel ED, Glass DJ, Moscoso LM, Yancopoulos GD, Sanes JR (1997) Rapsyn is required for MuSK signaling and recruits synaptic components to a MuSK-containing scaffold. Neuron 18:623-635.

Arber S, Burden SJ, Harris AJ (2002) Patterning of skeletal muscle. Curr Opin Neurobiol 12:100-103.

Bloch RJ (1988) Molecular events in synaptogenesis: nerve-muscle adhesion and postsynaptic differentiation. Am J Physiol 254:C345-364.

Brandon EP, Lin W, D'Amour KA, Pizzo DP, Dominguez B, Sugiura Y, Thode S, Ko CP, Thal LJ, Gage FH, Lee KF (2003) Aberrant patterning of neuromuscular synapses in choline acetyltransferase-deficient mice. J Neurosci 23:539-549.

Bresler T, Shapira M, Boeckers T, Dresbach T, Futter M, Garner CC, Rosenblum K, Gundelfinger ED, Ziv NE (2004) Postsynaptic density assembly is fundamentally different from presynaptic active zone assembly. J Neurosci 24:1507-1520.

Burden SJ (2002) Building the vertebrate neuromuscular synapse. J Neurobiol 53:501-511.

Cooper RL, Fernandez-de-Miguel F, Adams WB, Nicholls JG (1992) Anterograde and retrograde effects of synapse formation on calcium currents and neurite outgrowth in cultured leech neurons. Proc R Soc Lond B Biol Sci 249:217-222.

Eisen JS, Myers PZ, Westerfield M (1986) Pathway selection by growth cones of identified motoneurones in live zebra fish embryos. Nature 320:269-271.

Feng G, Laskowski MB, Feldheim DA, Wang H, Lewis R, Frisen J, Flanagan JG, Sanes JR (2000) Roles for ephrins in positionally selective synaptogenesis between motor neurons and muscle fibers. Neuron 25:295-306.

Fischbach GD, Cohen SA (1973) The distribution of acetylcholine sensitivity over uninnervated and innervated muscle fibers grown in cell culture. Dev Biol 31:147-162.

Flanagan-Steet H, Fox MA, Meyer D, Sanes JR (2005b) Neuromuscular synapses can form in vivo by incorporation of initially aneural postsynaptic specializations. Development 132:4471-4481.

Frank E, Fischbach GD (1979) Early events in neuromuscular junction formation in vitro: induction of acetylcholine receptor clusters in the postsynaptic membrane and morphology of newly formed synapses. J Cell Biol 83:143-158.

Friedman HV, Bresler T, Garner CC, Ziv NE (2000) Assembly of new individual excitatory synapses: time course and temporal order of synaptic molecule recruitment. Neuron 27:57-69.

Gillespie SK, Balasubramanian S, Fung ET, Huganir RL (1996) Rapsyn clusters and activates the synapse-specific receptor tyrosine kinase MuSK. Neuron 16:953-962.

Goda Y, Davis GW (2003) Mechanisms of synapse assembly and disassembly. Neuron 40:243-264.

Harris AJ (1981) Embryonic growth and innervation of rat skeletal muscles. III. Neural regulation of junctional and extra-junctional acetylcholine receptor clusters. Phil Trans R Soc Lond B 293:287-314.

Hume RI, Role LW, Fischbach GD (1983) Acetylcholine release from growth cones detected with patches of acetylcholine receptor-rich membranes. Nature 305:632-634.

Javaherian A, Cline HT (2005) Coordinated motor neuron axon growth and neuromuscular synaptogenesis are promoted by CPG15 in vivo. Neuron 45:505-512.

Jin Y (2002) Synaptogenesis: insights from worm and fly. Curr Opin Neurobiol 12:71-79.

Jones G, Moore C, Hashemolhosseini S, Brenner HR (1999) Constitutively active MuSK is clustered in the absence of agrin and induces ectopic postsynaptic-like membranes in skeletal muscle fibers. J Neurosci 19:3376-3383.

Jontes JD, Emond MR, Smith SJ (2004) In vivo trafficking and targeting of N-cadherin to nascent presynaptic terminals. J Neurosci 24:9027-9034.

Lefebvre JL, Ono F, Puglielli C, Seidner G, Franzini-Armstrong C, Brehm P, Granato M (2004) Increased neuromuscular activity causes axonal defects and muscular degeneration. Development 131:2605-2618.

Lin W, Burgess RW, Dominguez B, Pfaff SL, Sanes JR, Lee KF (2001) Distinct roles of nerve and muscle in postsynaptic differentiation of the neuromuscular synapse. Nature 410:1057-1064.

Lin W, Dominguez B, Yang J, Aryal P, Brandon EP, Gage FH, Lee KF (2005) Neurotransmitter acetylcholine negatively regulates neuromuscular synapse formation by a Cdk5-dependent mechanism. Neuron 46:569-579.

Liu DW, Westerfield M (1992) Clustering of muscle acetylcholine receptors requires motoneurons in live embryos, but not in cell culture. J Neurosci 12:1859-1866.

Lupa MT, Hall ZW (1989) Progressive restriction of synaptic vesicle protein to the nerve terminal during development of the neuromuscular junction. J Neurosci 9:3937-3945.

Misgeld T, Burgess RW, Lewis RM, Cunningham JM, Lichtman JW, Sanes JR (2002) Roles of neurotransmitter in synapse formation. Development of neuromuscular junction lacking choline acetyltransferase. Neuron 36:635-648.

Misgeld T, Kummer TT, Lichtman JW, Sanes JR (2005) Agrin promotes synaptic differentiation by counteracting an inhibitory effect of neurotransmitter. PNAS 102:11088-11093.

Morris JK, Lin W, Hauser C, Marchuk Y, Getman D, Lee KF (1999) Rescue of the cardiac defect in ErbB2 mutant mice reveals essential roles of ErbB2 in peripheral nervous system development. Neuron 23:273-283.

Myers PZ, Eisen JS, Westerfield M (1986) Development and axonal outgrowth of identified motoneurons in the zebrafish. J Neurosci 6:2278-2289.

Okabe S, Miwa A, Okado H (2001) Spine formation and correlated assembly of presynaptic and postsynaptic molecules. J Neurosci 21:6105-6114.

Ono F, Higashijima S, Shcherbatko A, Fetcho JR, Brehm P (2001) Paralytic zebrafish lacking acetylcholine receptors fail to localize rapsyn clusters to the synapse. J Neurosci 21:5439-5448.

Ono F, Shcherbatko A, Higashijima S, Mandel G, Brehm P (2002) The Zebrafish motility mutant twitch once reveals new roles for rapsyn in synaptic function. J Neurosci 22:6491-6498.

Panzer JA, Gibbs SM, Dosch R, Wagner D, Mullins MC, Granato M, Balice-Gordon RJ (2005) Neuromuscular synaptogenesis in wild-type and mutant zebrafish. Developmental Biology 285:340-357.

Park HC, Kim CH, Bae YK, Yeo SY, Kim SH, Hong SK, Shin J, Yoo KW, Hibi M, Hirano T, Miki N, Chitnis AB, Huh TL (2000) Analysis of upstream elements in the HuC promoter leads to the establishment of transgenic zebrafish with fluorescent neurons. Dev Biol 227:279-293.

Rao A, Kim E, Sheng M, Craig AM (1998) Heterogeneity in the molecular composition of excitatory postsynaptic sites during development of hippocampal neurons in culture. J Neurosci 18:1217-1229.

Sabo SL, McAllister AK (2003) Mobility and cycling of synaptic protein-containing vesicles in axonal growth cone filopodia. Nat Neurosci 6:1264-1269.

Saito Y, Murakami F, Song WJ, Okawa K, Shimono K, Katsumaru H (1992) Developing corticorubral axons of the cat form synapses on filopodial dendritic protrusions. Neurosci Lett 147:81-84.

Sanes JR, Lichtman JW (1999) Development of the vertebrate neuromuscular junction. Annu Rev Neurosci 22:389-442.

Sytkowski AJ, Vogel Z, Nirenberg MW (1973) Development of acetylcholine receptor clusters on cultured muscle cells. Proc Natl Acad Sci U S A 70:270-274.

Washbourne P, Bennett JE, McAllister AK (2002) Rapid recruitment of NMDA receptor transport packets to nascent synapses. Nat Neurosci 5:751-759.

Watty A, Neubauer G, Dreger M, Zimmer M, Wilm M, Burden SJ (2000) The in vitro and in vivo phosphotyrosine map of activated MuSK. Proc Natl Acad Sci U S A 97:4585-4590.

Westerfield M, McMurray JV, Eisen JS (1986) Identified motoneurons and their innervation of axial muscles in the zebrafish. Journal of Neuroscience 6:2267-2277.

Westerfield M, Liu DW, Kimmel CB, Walker C (1990) Pathfinding and synapse formation in a zebrafish mutant lacking functional acetylcholine receptors. Neuron 4:867-874.

Yang X, Li W, Prescott ED, Burden SJ, Wang JC (2000) DNA topoisomerase IIbeta and neural development. Science 287:131-134.

Yang X, Arber S, William C, Li L, Tanabe Y, Jessell TM, Birchmeier C, Burden SJ (2001) Patterning of muscle acetylcholine receptor gene expression in the absence of motor innervation. Neuron 30:399-410.

Zeller J, Schneider V, Malayaman S, Higashijima S, Okamoto H, Gui J, Lin S, Granato M (2002) Migration of zebrafish spinal motor nerves into the periphery requires multiple myotome-derived cues. Dev Biol 252:241-256.

Zhang J, Lefebvre JL, Zhao S, Granato M (2004) Zebrafish unplugged reveals a role for muscle-specific kinase homologs in axonal pathway choice. Nat Neurosci 7:1303-1309.

**Figures and Legends**

**Fig. 1 Location of prepatterned AChR clusters in myotomal muscle.**

Presynaptic vesicles in motor axons and terminals were labeled with an antibody against SV2 (green) and postsynaptic AChR clusters were labeled with rhodamine αBTX (red) in 24 hpf embryos. Except where indicated, all images are oriented so that rostral is to the left and dorsal is at the top. The dashed line in each panel indicates the edge of the spinal cord. Higher magnification views of the boxed regions in A are shown in B-D.

**A:** In rostral segments (left), primary motor axons have grown past the choice point and have begun to extend along the medial surface of the myotome. In middle segments, motor axons have just reached the choice point. In the most caudal segments (right), motor axons have not yet exited the spinal cord. Prepatterned AChR clusters are visible throughout the dorsal and ventral extent of the myotome and along the lateral myosepta. Scale bar = 10 μm.

**B:** In rostral segments, as motor axons form the initial neuromuscular synapses at the choice point (bracket), and extend beyond it along the medial surface of the myotome, some prepatterned AChR clusters dorsal and ventral to the choice point have disappeared.

**C:** In middle segments, as motor axons enter the myotome, prepatterned AChR clusters are reduced in number, smaller, and more punctate in appearance.

**D:** In caudal segments, prepatterned AChR clusters are elongated and diffuse along each muscle fiber, well in advance of outgrowing motor axons. Scale bar = 10 μm.

**Fig. 1 Location of prepatterned AChR clusters in myotomal muscle.**

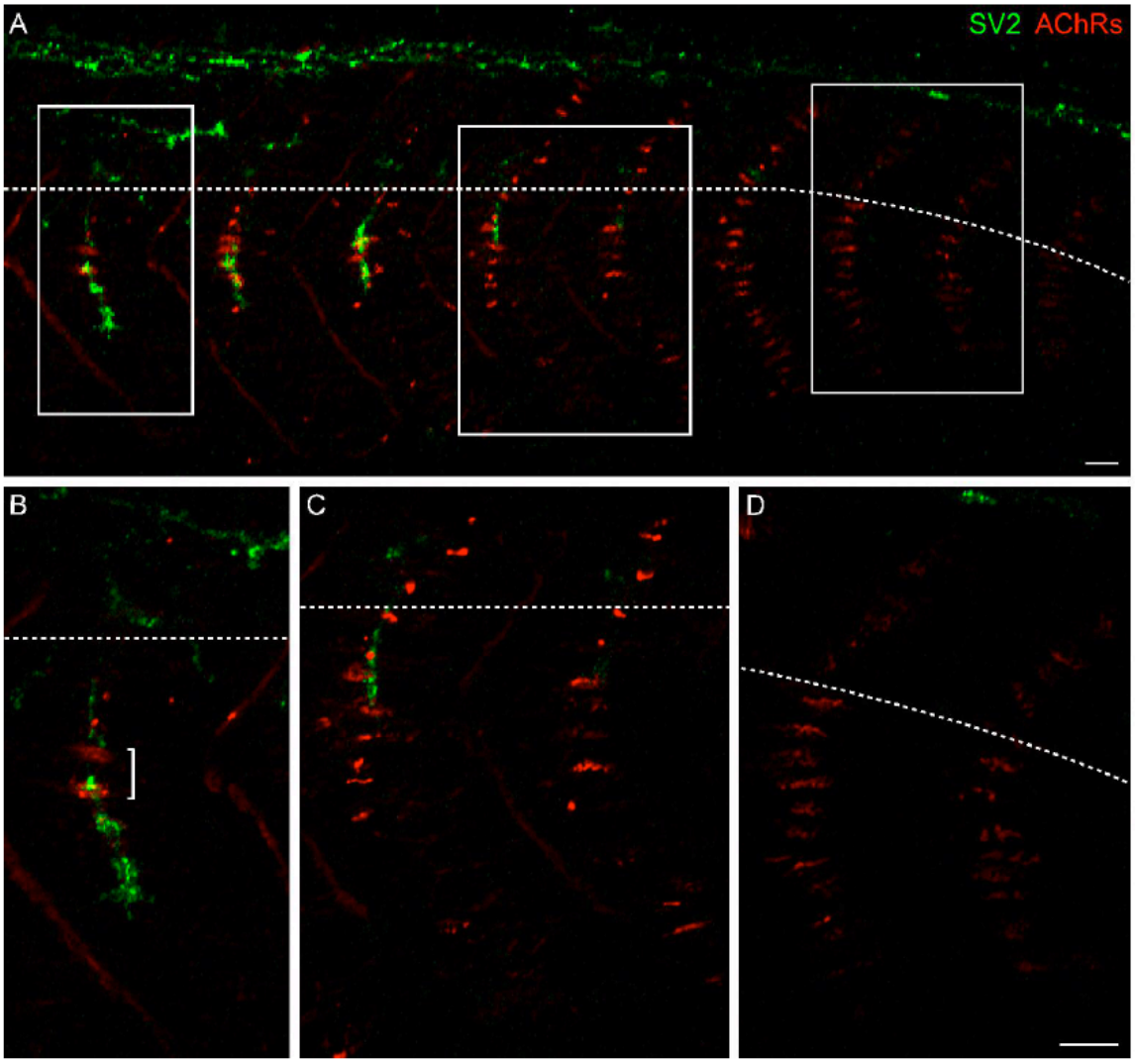

**Fig. 2 Dynamics of prepatterned AChR clusters.**

Rhodamine αBTX labeled AChRs (red) imaged in transgenic embryo expressing GFP in neurons to visualize motor axons (HuC:GFP, green) from 20-26 hpf at 1 hour intervals (Supplemental Movie 1).

**A:** Time lapse images of prepatterned AChR clusters. The first movie plane was taken at time 0:00, prior to motor axon outgrowth from the spinal cord. Boxed regions in the first panel are shown at higher magnification in B and D. Prepatterned AChR clusters are initially elongated and diffuse and coalesce over time (e.g., compare panels 1:00 and 3:00). The final panel is post-imaging immunostaining for presynaptic vesicles (SV2; green) that demonstrates that motor axons have grown to and synapses have been established at the choice point (bracket) by 6:00. Scale bar = 10 μm.

**B:** Higher magnification of boxed region in A. As motor axons exit the spinal cord and innervate the choice point, many pre-patterned AChR clusters disappear (disappearing cluster indicated by arrow). In this small region, many pre-patterned AChRs disappear over the six hour imaging interval (compare cluster marked with an arrow from panels 0:00 to 6:00). However, throughout the myotome, 20% of prepatterned AChR clusters disappear over a 6 hour imaging interval. Scale bar = 10 μm.

**C:** Line scan (8 μm in length) through the cluster marked with an arrow in B shows that cluster fluorescence intensity (arbitrary units) and length decrease gradually over the 6 hour imaging interval.

**D:** Higher magnification of boxed region in A. In this small region, 2 of the 4 prepatterned AChR clusters present at the first views are incorporated into synapses (compare cluster marked with an arrow in panels 0:00 to 6:00) as evidenced by the appearance of a GFP+ axon over the AChR cluster at panel 5:00 (asterisk) that persists to 6:00. However, throughout the myotome, 30% of prepatterned AChR clusters are incorporated into synapses. D': Post-imaging immunostaining demonstrating an SV2+ vesicle cluster formed at this AChR cluster. D''-D''': single channel images of the boxed region in D', demonstrating colocalization of the SV2+ vesicle cluster (indicated by dashed line) with the AChR cluster. Scale bar = 10 μm.

**E:** Line scan (11 μm) through the AChR cluster marked with an arrow in D shows that cluster width gradually decreases and that fluorescence persists throughout the 6 hour imaging interval.

**F:** Quantification of AChR cluster length at 0:00 and 6:00, demonstrating that prepatterned AChR clusters coalesce and become significantly reduced in length over time (N = 4 fish, 19 myotome segments; Komolgorov-Smirnoff test, $p < 0.001$).

**G:** Quantification of AChR cluster intensity at 0:00 and 6:00, determined by measuring the average pixel intensity along a line scan, demonstrating that prepatterned AChR clusters significantly increase in fluorescence over time (N = 4 fish, 19 myotome segments; Komolgorov-Smirnoff test, $p < 0.001$).

**H:** Quantification of the fate of prepatterned AChR clusters. Of all prepatterned AChR clusters, 20% disappeared; 30% become synaptic during the 6 hour imaging

interval; and 50% remain non-synaptic during the imaging interval (N = 4 fish, 14 myotome segments).

**Fig. 2 Dynamics of prepatterned AChR clusters.**

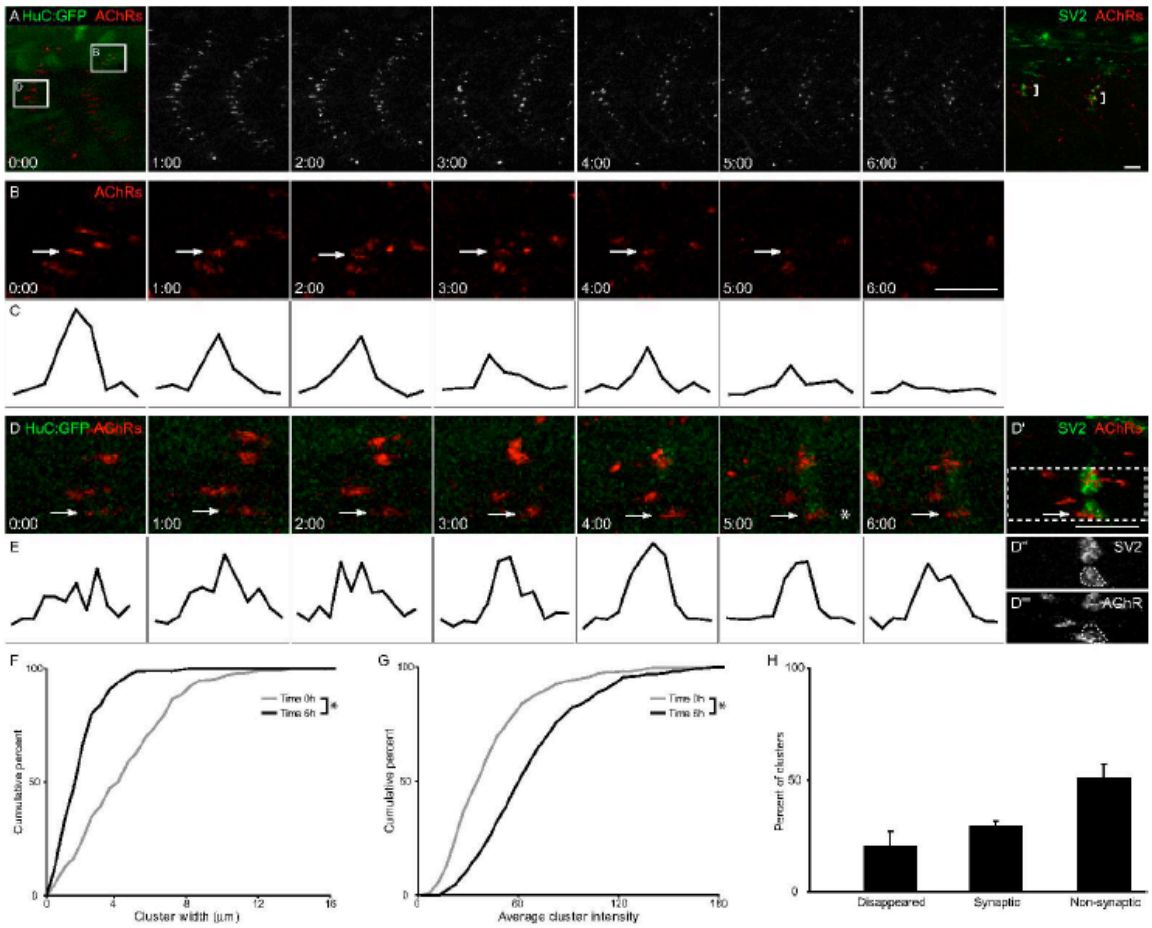

**Fig. 3 Motor axon growth cones preferentially extend toward prepatterned AChR clusters.**

**A-C:** A primary motor neuron, MiP, expressing VAMP-GFP (green) and AChR clusters labeled with rhodamine αBTX (red) from a ca. 24 hpf embryo were imaged for more than 4 hours at intervals of 20 minutes (Supplemental Movie 2). The dashed line indicates the edge of the spinal cord. In this series of images, the position of AChRs is fixed, while a single motor axon growth cone advances across the field of view. In the supplemental movie, AChR clusters near the bottom of the frame appear to move because the embryo is growing. Since we did not attempt to focus on this region during image capture, these clusters come in and out of the field of view on several occasions.

**A:** At the start of time lapse imaging, MiP has extended to the choice point (bracket), and a dorsal axon branch is growing toward prepatterned AChR clusters (arrow). The boxed region is shown at higher magnification in B.

**B:** Time lapse images of the MiP growth cone extending toward, contacting, and then extending beyond, prepatterned AChR clusters. In some cases, VAMP-GFP+ clusters of presynaptic vesicles accumulate over prepatterned AChR clusters (panel 0:40, asterisks). In panels 3:00-4:20, the growth cone turns 65º toward prepatterned AChR clusters at the dorsal edge of the myotome and lateral myosepta (arrowhead). Scale bar = 10 μm.

**C:** At the end of time lapse imaging, the MiP axon has reached the dorsal edge of the myotome, and has just contacted AChR clusters located at the dorsal edge of the myosepta. The boxed region is the same as in A. Scale bar = 10 μm.

**D:** To quantify axon and growth cone outgrowth with respect to prepatterned AChR clusters, the position of a growth cone was determined from a point in its geometric center (arrow). The closest AChR cluster in advance of the growth cone was defined as a potential target AChR cluster (red oval). Three angles were then measured: angle 1, the angle between the actual growth cone trajectory (black line) and a straight trajectory toward the AChR cluster (red dashed line); angle 2, the angle between the actual trajectory and the initial trajectory if the growth cone were to grow in a straight line (blue dashed line); and angle 3, the angle between the initial trajectory and the target AChR cluster (N = 9 22-30 hpf embryos, 9 motor neurons, 38 growth cone outgrowth events).

**E:** The distribution of angles 1 and 2. Sixty-three percent of growth cones are extended with an angle ≤ 10º, and 95% are extended at an angle of ≤ 30º, with respect to a prepatterned AChR cluster (black bars). Growth cones were observed to turn toward a prepatterned AChR cluster over a wide range of angles, from 10º to 130º (grey bars).

**F:** Angle 2 was plotted against angle 3 and their relationship was analyzed by linear regression. A significant correlation exists between the location of a prepatterned AChR cluster with respect to the motor axon's initial trajectory (angle 3), and the angle (angle 2) that the growth cone eventually turns toward that cluster (r = 0.91).

**Fig. 3 Motor axon growth cones preferentially extend toward prepatterned AChR clusters.**

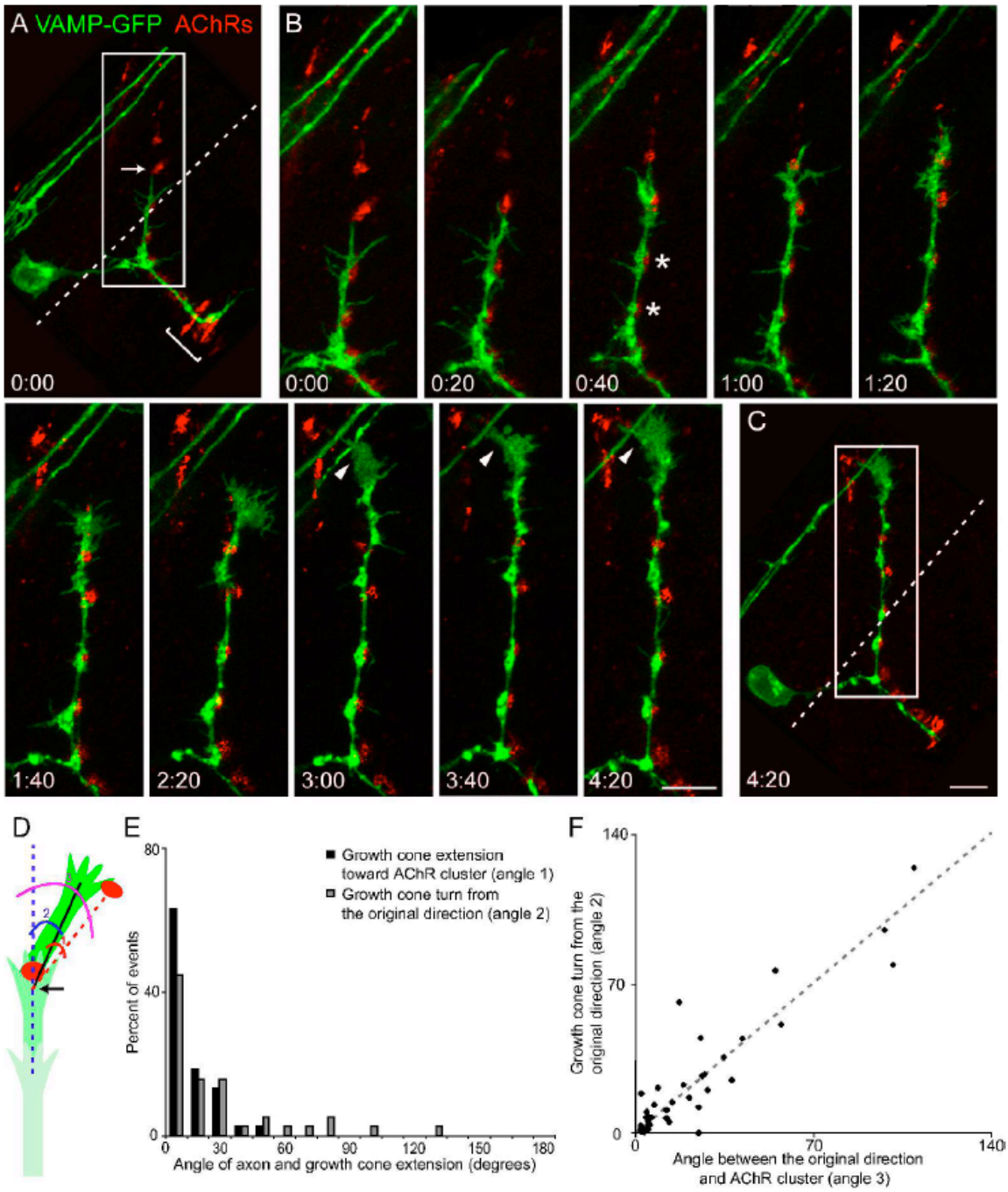

**Fig. 4 Motor axon filopodia preferentially extend toward and contact prepatterned AChR clusters.**

**A-C:** A primary motor neuron, RoP, expressing VAMP-GFP (green) and prepatterned AChR clusters labeled with rhodamine αBTX (red) from a ca. 24 hpf embryo imaged for over 5 hours at intervals of 10 minutes (Supplemental Movie 3). Due to focal plane drift the leftmost AChR cluster in Supplemental Movie 3 briefly disappears for the first 5 frames at the beginning of the movie.

**A:** The growth cone pauses at the choice point (bracket), and forms a rostrally extending branch (panel 5:00). Two areas containing prepatterned AChRs are present (panel 0:00; rostral area, arrowhead; caudal and ventral area, arrow). Scale bar = 5 μm.

**B:** Many filopodia are extended toward the caudal area containing prepatterned AChR clusters (panel 0:00, arrow). Filopodia contact this AChR cluster twice (panel 0:10 and 3:30, asterisk) and retract. Scale bar = 5 μm.

**C:** Filopodia are also extended toward the rostral area containing prepatterned AChR clusters (panel 3:20, arrowhead). A filopodia contacts an AChR cluster (panel 4:00, asterisk) and then retracts (panel 4:10), contacts the cluster again (panel 4:20, asterisk), and persists until the end of the imaging session. Scale bar = 5 μm.

**D:** Quantification of filopodial extension. The upper panel illustrates a segment of a motor axon with 3 filopodia (green) and a prepatterned AChR cluster (red) off to the side of the axon. In the bottom panel, the dashed line indicates the shortest distance between the base of each filopodia at the axon and the AChR cluster. The solid line

indicates the actual direction of filopodial extension. The angle between these two lines was measured for each filopodia.

**E:** Distribution of the angle of filopodial extension with respect to prepatterned AChR clusters for the RoP axon shown in A-C. The location of prepatterned AChR clusters was aligned at 0° (red dot). Each line represents one filopodia, the length of the line represents filopodial length, and the angle represents the angle of filopodial extension with respect to a prepatterned AChR cluster. The majority of filopodia are extended at an angle ≤ 30° with respect to prepatterned AChR clusters.

**F:** Distribution of the angle of filopodial extension with respect to a control area 15 μm away from the axon. Filopodia are extended randomly if an AChR cluster is not present.

**G:** Summary plot of cumulative percent of angles of filopodial extension with respect to prepatterned AChR clusters (gray line; N = 6 22-30 hpf embryos, 6 motor neurons, 230 filopodia) or control areas (black line; N = 167 filopodia) for all filopodia from all motor neurons imaged (significantly different, Kolmogorov-Smirnov test, $p < 0.0001$).

**Fig. 4 Motor axon filopodia preferentially extend toward and contact prepatterned AChR clusters.**

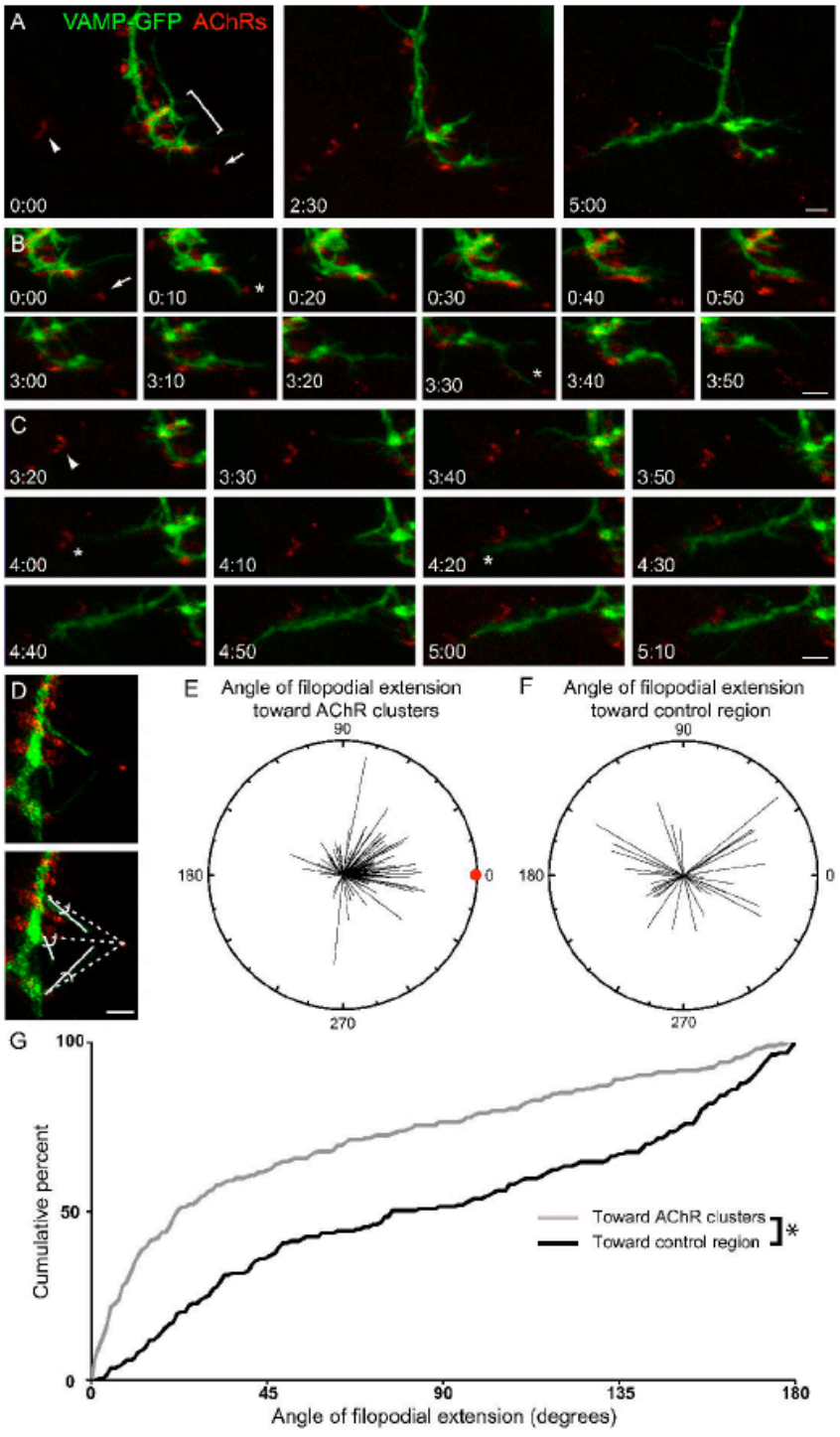

**Fig. 5 Filopodia are preferentially extended from synapses.**

Examples of filopodia extended from primary motor neurons expressing VAMP-GFP (green) and prepatterned AChR clusters labeled with rhodamine αBTX (red) from ca. 22-30 hpf embryos.

**A-A":** Filopodia are extended from VAMP-GFP+ clusters of presynaptic vesicles (A) that are apposed to AChR clusters (A') and are thus synapses (A").

**B-B":** Filopodia are extended from VAMP-GFP+ vesicle clusters (B) that are not apposed to AChR clusters (B', B").

**C-C":** Relatively few filopodia are extended from axon regions lacking VAMP-GFP+ clusters. Scale bar = 10 μm.

**D:** Quantification of the percent of filopodia extended from VAMP-GFP+ vesicle clusters (90%), from synapses (63%) or from the axon (10%).

**Fig. 5 Filopodia are preferentially extended from synapses.**

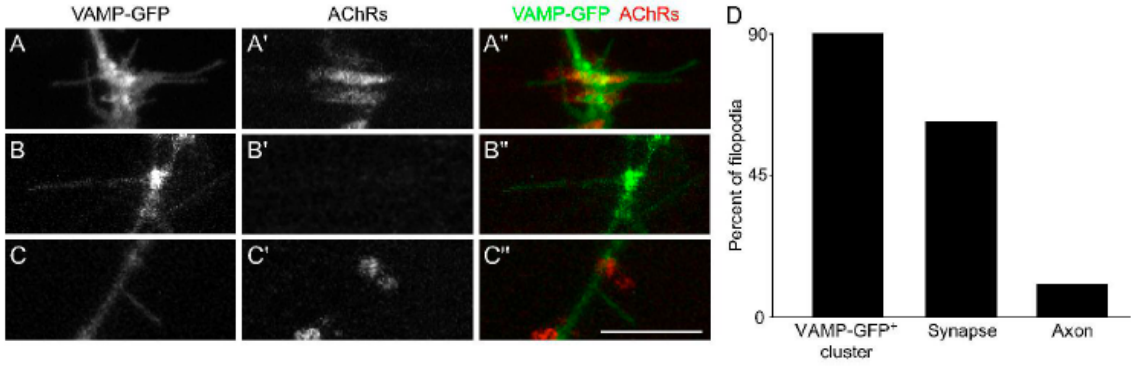

**Fig. 6 Postsynaptic AChR clusters precede presynaptic vesicle clusters during initial neuromuscular synaptogenesis.**

Primary motor neurons (CaP) expressing VAMP-GFP (green) and prepatterned AChR clusters labeled with rhodamine αBTX (red) from a ca. 24 hpf embryos imaged for 2-5 hours at intervals of 20 minutes.

**A:** At the beginning of the imaging session, a prepatterned AChR cluster is present in advance of the growth cone. The boxed region is shown at higher magnification in B. Scale bar = 10 μm.

**B:** Time lapse images of the growth cone extending toward, contacting, and then extending beyond, the AChR cluster. In panels 1:20 and 1:40, clusters of VAMP-GFP+ vesicles have accumulated over the AChR cluster. Scale bar = 10 μm.

**C, D:** The fluorescence intensity of postsynaptic AChRs (C) and presynaptic VAMP-GFP (D) are displayed as bars whose height and color are proportional to intensity (white, high; purple, low). This analysis shows that VAMP-GFP gradually accumulates over the AChR cluster.

**E:** At the beginning of the imaging session, a prepatterned AChR cluster is present in advance of the growth cone (arrow). The boxed region is shown at higher magnification in F and G. Scale bar = 10 μm.

**F, G:** Time lapse images of the growth cone contacting and growing past a prepatterned AChR cluster and the subsequent appearance of an AChR cluster beneath a filopodia. AChR labeling alone is shown in G for clarity. The cluster that was present in

advance of the growth cone is marked in F, panel 3:00 with an arrow. A VAMP-GFP+ cluster is subsequently induced over this AChR cluster (panel 4:00, asterisk). In addition, a cluster subsequently appears beneath a filopodia (F, G, panel 3:20, arrowhead). This AChR cluster becomes larger and increases in intensity over time (G, panel 4:40). A VAMP-GFP+ cluster appears at this site (panel 3:40) and persists throughout the imaging period (F, panel 4:40, open arrowhead). Scale bar = 10 μm.

**Fig. 6 Postsynaptic AChR clusters precede presynaptic vesicle clusters during initial neuromuscular synaptogenesis.**

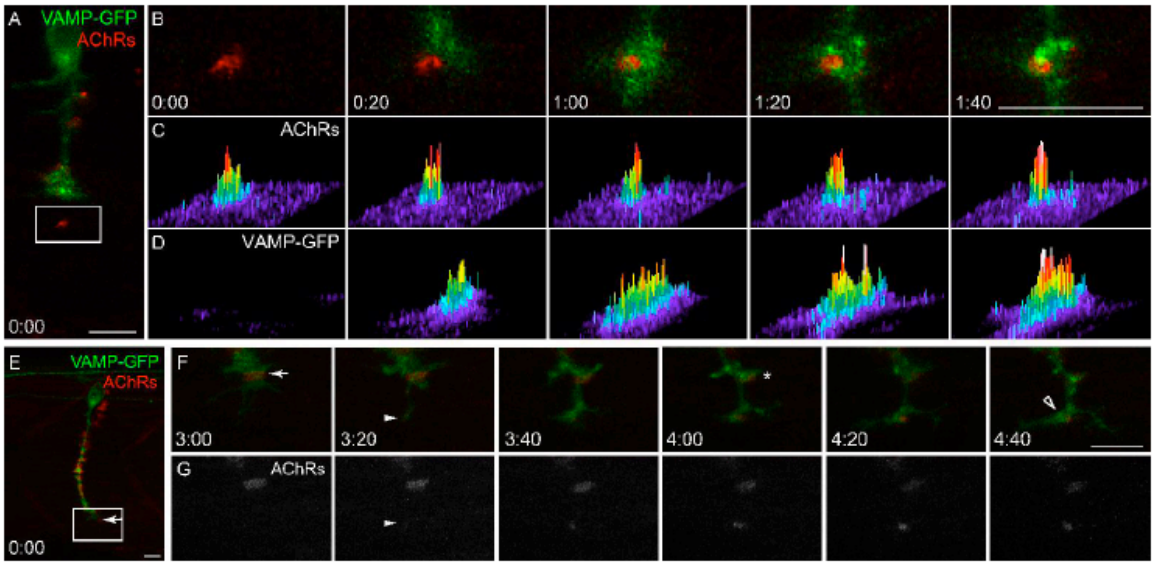

**Fig. 7 Insertion of new AChRs and redistribution of prepatterned AChRs during initial neuromuscular synaptogenesis.**

All AChRs were optically saturated with rhodamine αBTX at 20 hpf, and 2, 4 or 7 hours later, embryos were fixed and newly inserted AChRs were labeled with Cy5 αBTX. The location of existing (old; red) AChRs and receptors inserted since the initial rhodamine αBTX labeling (new; blue) was compared to the location of motor axons and terminals visualized after immunostaining for SV2 (green).

**A-A':** Prepatterned AChRs present prior to motor axon outgrowth at 20 hpf.

**B-B":** In embryos relabeled with Cy5 αBTX four hours after initial labeling of old AChRs with rhodamine αBTX, all prepatterned AChRs have coalesced and some have disappeared, consistent with immunostaining and *in vivo* imaging observations. The majority of synaptic AChR clusters were composed of both old (B') and new (B") AChRs. The majority of non-synaptic sites (B, arrows) were composed only of old AChRs. Few if any AChR clusters are composed only of newly inserted AChRs.

**C-C":** In embryos relabeled with Cy5 αBTX seven hours after initial labeling, old AChRs labeled with rhodamine αBTX were colocalized with new AChRs in clusters beneath presynaptic nerve terminals throughout the myotome. Scale bar = 10 μm.

**D:** Quantification of the percent of AChR clusters containing old, new or both old and new receptors in synaptic and non-synaptic sites (N = 6 22-24 hpf embryos, 170 clusters).

**Fig. 7 Insertion of new AChRs and redistribution of prepatterned AChRs during initial neuromuscular synaptogenesis.**

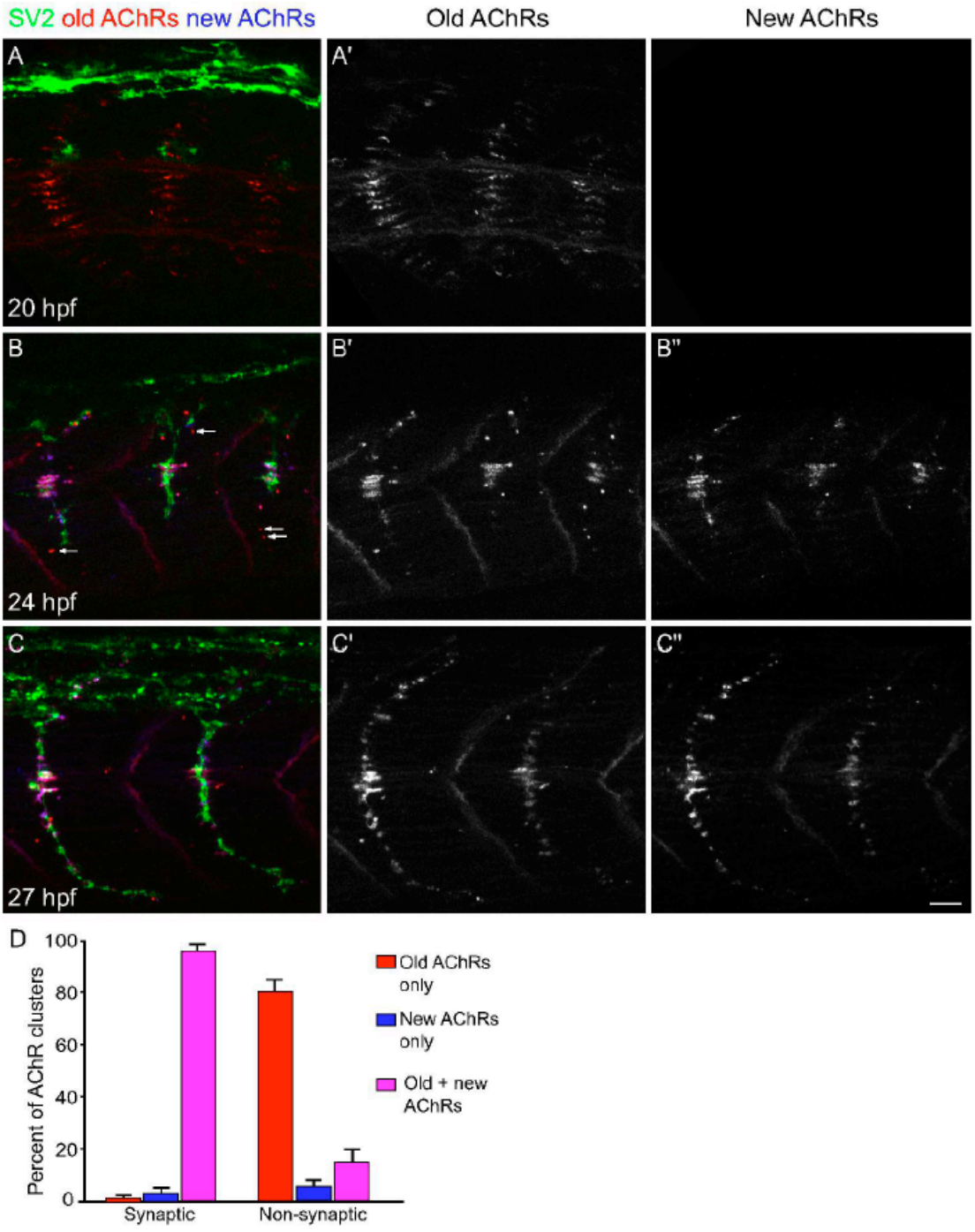

**Fig. 8. AChR activity or AChR clusters are not required for motor axon outgrowth or neuromuscular synaptogenesis.**

**A-C:** 24 hpf embryos in which SV2+ presynaptic axons and terminals (green) and rhodamine αBTX labeled AChRs (red) were analyzed in rostral (A, B, C), middle (A', B', C') and caudal (A", B", C") segments. Brackets indicate the location of the first neuromuscular synapses formed at the choice point.

**A:** Motor axon outgrowth, prepatterned AChRs and initial neuromuscular synaptogenesis in wild type, unmanipulated control embryos (N = 4 24 hpf embryos; 8 myotome segments).

**B:** Motor axon outgrowth, prepatterned AChRs and initial neuromuscular synaptogenesis in embryos in which AChRs were blocked with rhodamine αBTX from 12-24 hpf (N = 4 24 hpf embryos; 8 myotome segments). The dorsal and ventral extent of motor axon outgrowth, prepatterned AChRs and initial synaptogenesis are similar to control embryos.

**C:** Motor axon outgrowth and formation of SV2+ presynaptic vesicle clusters in *sop* embryos (N = 7 24 hpf embryos, 14 myotome segments). Although AChRs are absent, the dorsal and ventral extent of motor axon outgrowth is similar to normal siblings (N = 6 24 hpf embryos, 12 myotome segments; not shown). Presynaptic vesicle clusters are present all along the length of axons, but clusters at the choice point (bracket) are enlarged. Scale bar = 10 μm.

**D:** Quantification of motor axon outgrowth, normalized to myotome width, for rostral and middle myotomes in control and αBTX blocked embryos, *sop* mutants and normal siblings. Mean values ± s.e.m. are not significantly different (Student's t test).

**E:** Quantification of SV2+ cluster number and total area in control and αBTX blocked embryos, *sop* mutants and normal siblings, and of AChR cluster and synapse number and total area in control and αBTX blocked embryos. Number and total area measurements were normalized to axon length. Mean values ± s.e.m. are not significantly different between control and αBTX blocked embryos or between *sop* mutants and normal siblings (Student's t test).

**F:** Cumulative percent of the area of individual SV2+ clusters in control and αBTX blocked embryos, *sop* mutants and normal siblings. While the mean values for total area are not different among these groups (E), the distribution of the area of individual SV2+ clusters is shifted toward larger values in αBTX blocked compared to control embryos (Komolgorov-Smirnoff test, $p = 0.002$) and in *sop* mutants compared to normal siblings ($p < 0.0001$), probably reflecting the enlarged presynaptic SV2+ cluster area at 3-4 choice point synapses in each myotome.

**G:** Quantification of prepatterned AChR cluster number and total area from caudal segments of control and αBTX blocked embryos, normalized to myotome width. Mean values ± s.e.m. are not significantly different (Student's t test).

**Fig. 8. AChR activity or AChR clusters are not required for motor axon outgrowth or neuromuscular synaptogenesis.**

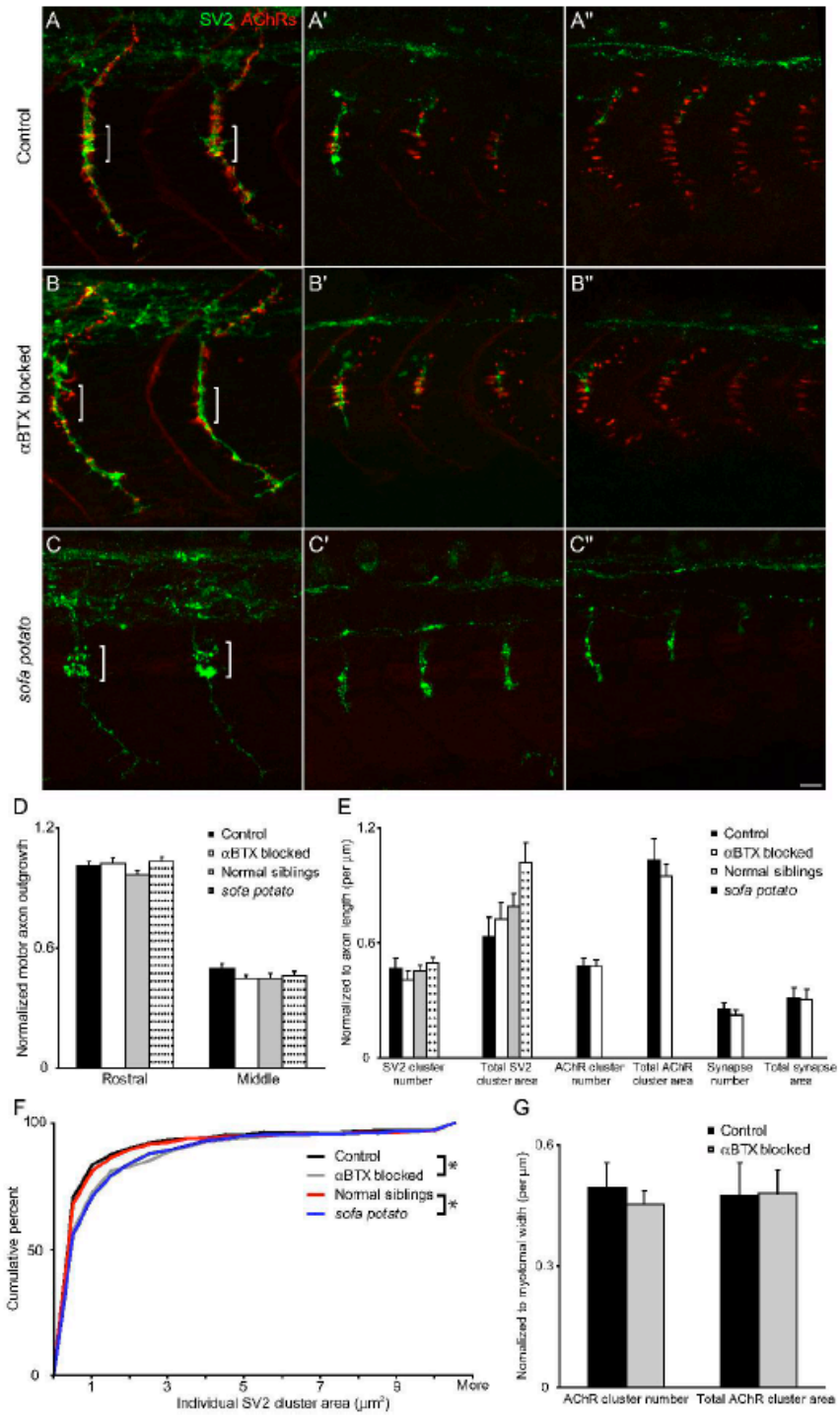

**Supplemental Fig. 1 VAMP-GFP marks sites of presynaptic vesicle clusters and does not alter motor axon outgrowth.**

Transient transgenic embryos at 24 hpf in which some motor neurons express VAMP-GFP (green) and postsynaptic AChRs are labeled with rhodamine αBTX (red).

**A:** VAMP-GFP+ CaP primary motor neurons (green), one in each of two adjacent caudal segments. The boxed regions 1 and 2 are shown at higher magnification to the right. Post-imaging immunostaining shows that VAMP-GFP is colocalized with SV2 (blue), demonstrating that VAMP-GFP marks clusters of synaptic vesicles. Scale bar = 10 μm.

**B:** The left of 2 adjacent rostral segments is innervated by a VAMP-GFP+ CaP motor neuron (green). Comparison with segments innervated by GFP- motor neurons (right) immunostained for SV2 to mark axons and presynaptic terminals (blue) shows that the extent of motor axon outgrowth and branching is unaffected by VAMP-GFP expression. Scale bar = 10 μm.

**C:** VAMP-GFP+ primary motor neuron CaP imaged over time at 24-72 hpf. At ca. 24 hfp, relatively few motor axon branches or neuromuscular synapses are present, whereas by ca. 72 hpf axons have branched into their appropriate, cell specific territory and many neuromuscular synapses are present. These data show that the imaging procedures used do not interfere with axon outgrowth or neuromuscular synaptogenesis. Scale bar = 10 microns.

**Supplemental Fig. 1 VAMP-GFP marks sites of presynaptic vesicle clusters and does not alter motor axon outgrowth.**

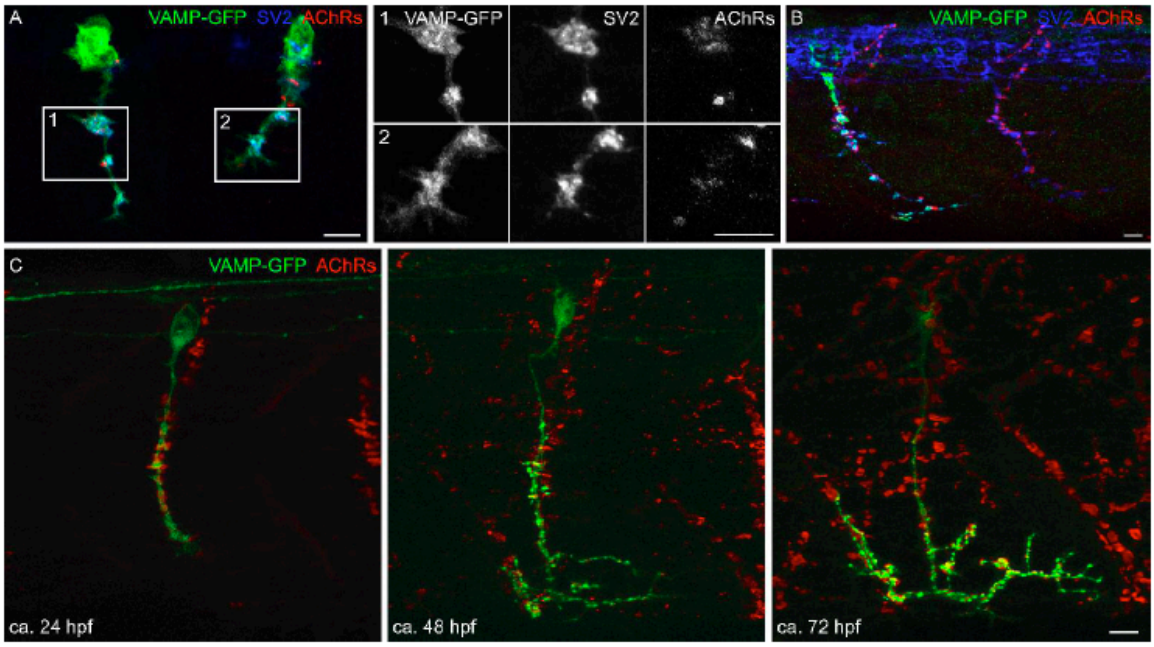

**Supplemental Fig. 2 Blockade of sodium channels with tricaine does not affect dispe rsal of prepatterned AChR clusters or initial motor axon outgrowth.**

A-B: Presynaptic vesicles in motor axons and terminals were labeled with an anti body against SV2 (green) and postsynaptic AChR clusters were labeled with rhodamine a BTX (red) in 24 hpf embryos**.**

**A:** Motor axon outgrowth, prepatterned AChRs and initial neuromuscular synaptogenesis in wild type, unmanipulated control embryos at 21 hpf.

**B:** Motor axon outgrowth, prepatterned AChRs and initial neuromuscular synaptogenesis in embryos in which AChRs were blocked with tricaine from 10-21 hpf. Motor axon outgrowth, number and area of prepatterned AChRs, and dispersal of prepatterned AChRs were indistinguishable from that observed in control embryos.

**Supplemental Fig. 2 Blockade of sodium channels with tricaine does not affect dispersal of prepatterned AChR clusters or initial motor axon outgrowth.**

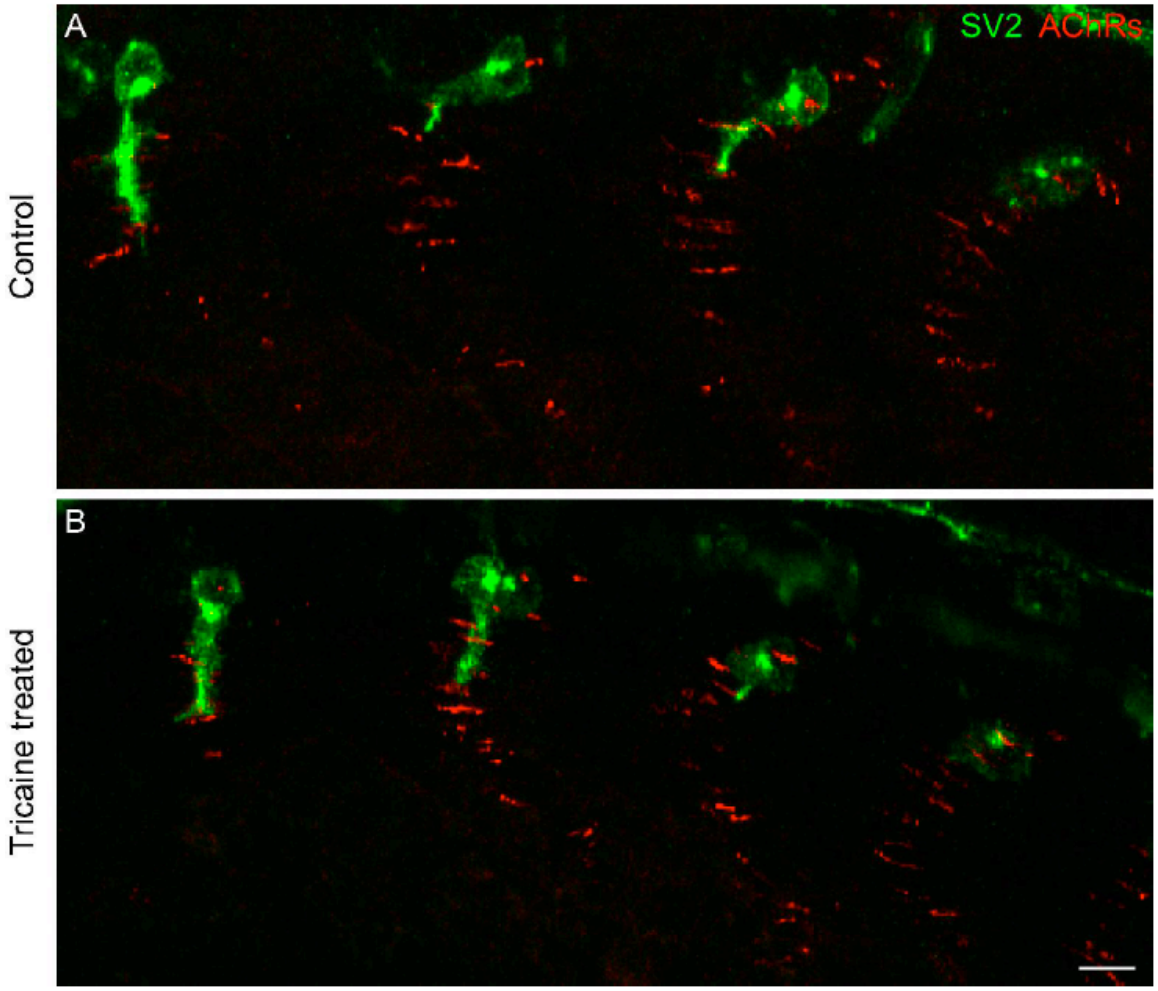

# Chapter 3

## Notch-dependent and -independent mechanisms underlie neural and synaptic defects in *slytherin*, a zebrafish model for human congenital disorders of glycosylation

In revision in Development

# Notch-dependent and -independent mechanisms underlie neural and synaptic defects in *slytherin*, a zebrafish model for human congenital disorders of glycosylation

Y. Song[1], J. R. Willer[3], P. C. Scherer[1], J. A. Panzer[1], A. Kugath[1], E. Skordalakes[2], R. G. Gregg[3], G. B. Willer[3] and R. J. Balice-Gordon[1]

[1]Dept. of Neuroscience, University of Pennsylvania School of Medicine, Philadelphia, PA; [2]Wistar Institute, Philadelphia, PA; [3]Dept. of Biochemistry and Molecular Biology, University of Louisville, Louisville, KY

**Running title:** Neural and synaptic phenotypes in *srn*

**Summary / Figs. / Tables / Sup. Figs. and Tables:** 169 words / 9 / 0 / 6+1

**Key words:** glycosylation, fucosylation, neurogenesis, synaptogenesis, neuromuscular, axon, retina, optic tectum

**Address correspondence to:**

Rita Balice-Gordon, Dept. of Neuroscience, University of Pennsylvania School of Medicine, 215 Stemmler Hall, Philadelphia, PA 19104-6074. (215) 898-1037 Fax: (215) 573-9122 Email: rbaliceg@mail.med.upenn.edu

**Abstract**

Congenital disorder of glycosylation type IIc (CDG IIc) is characterized by mental retardation, slowed growth and severe immunodeficiency, attributed to the lack of fucosylated glycoproteins. While impaired Notch signaling has been implicated in some aspects of CDG IIc pathogenesis, the molecular and cellular mechanisms remain poorly understood. We have identified a zebrafish mutant *slytherin* (*srn*), which harbors a missense point mutation in GDP-mannose 4,6 dehydratase (GMDS), the rate-limiting enzyme in protein fucosylation, including that of Notch. Here we report that some of the mechanisms underlying the neural phenotypes in *srn* and in CGD IIc are Notch-dependent, while others are Notch-independent. We show, for the first time in a vertebrate *in vivo,* that defects in protein fucosylation leads to defects in neuronal differentiation, maintenance, axon branching, and synapse formation. *Srn* is thus a useful and important vertebrate model for human CDG IIc that has provided new insights into the neural phenotypes that are hallmarks of the human disorder and has also highlighted the role of protein fucosylation in neural development.

## Introduction

Congenital disorder of glycosylation, type IIc (CDG IIc), also known as leukocyte adhesion deficiency II (LAD II) or Rambam-Hasharon syndrome (RHS), is an autosomal recessive syndrome, characterized by recurrent infections, persistent leukocytosis, severe mental retardation and slowed growth (Becker and Lowe, 1999; Etzioni et al., 2002). The immunodeficiency that is a hallmark of these syndromes is believed to be caused by dysregulated fucose metabolism, resulting in the absence of all fucosylated glycans on the cell surface (Becker and Lowe, 1999; Etzioni et al., 2002). The gene responsible for CDG IIc has been identified as GDP-fucose transporter (*FUCT1*) (Lubke et al., 2001; Luhn et al., 2001), which translocates GDP-fucose from the cytosol into the Golgi lumen for fucosyltransferase-catalyzed reactions during the modification of glycans.

Several animal models have been generated to study the pathogenesis of CDG IIc: *FX* locus null mice, lacking an enzyme in the *de novo* GDP-fucose synthesis pathway (Smith et al., 2002), *Gfr* (homologous to *FUCT1*) null flies (Ishikawa et al., 2005) and *Fuct1* null mice (Hellbusch et al., 2007). *Gfr* null flies display *Notch*-like phenotypes during wing development and reduced Notch fucosylation, suggesting that Notch deficiency may be responsible for some of the developmental defects in CDG IIc patients (Ishikawa et al., 2005). However, despite the neurodevelopmental and cognitive dysfunction prominent in CDG IIc patients, the anatomical, cellular and molecular abnormalities within the nervous system have not been well documented, and the mechanisms underlying this and other neural phenotypes remain unexplored.

A huge body of literature has demonstrated an important role for Notch-Delta signaling in neuronal and glial specification, neuronal maturation and learning and memory (Yoon and Gaiano, 2005). Specifically, in zebrafish, Notch-Delta signaling has been shown to regulate neurogenesis and gliogenesis. For instance, deficiency of Notch1a as in *deadly seven* (*des*) mutants resulted in increased primary motor neurons and Mauthner neurons (Gray et al., 2001); deficiency of Delta A as in *dla* mutant caused excessive primary motor neuron genesis at the expense of secondary motor neurons, some ventral interneurons and oligodendrocytes (Appel and Eisen, 1998; Appel et al., 2001; Park and Appel, 2003); mutation of *Mind Bomb* (an E3 ubiquitin ligase for Delta) as in *mib* resulted in a severe neurogenic phenotype together with the loss of oligodendrocytes (Itoh et al., 2003; Park and Appel, 2003). Other studies have supported the involvement of Notch signaling in the balance of excitatory/inhibitory synaptic input to hippocampal neurons (Salama-Cohen et al., 2006) and during synaptic plasticity (Wang et al., 2004). However, whether Notch-Delta signaling modulates synaptogenesis is unknown.

Here we report the genetic, cellular and molecular characterization of a zebrafish mutant *slytherin* (*srn*). Previously, we have identified *srn* as a synaptogenic mutant that exhibits abnormal swimming behavior, has increased number of primary motor neurons and aberrant neuromuscular synaptogenesis (Panzer et al., 2005). We have found that the *srn* mutation resides in GDP-mannose 4, 6-dehydratase (GMDS), the first and rate-limiting enzyme in the fucose metabolism pathway. Because dysfunction of the same pathway is responsible for human CDG IIc, we performed cellular and molecular analyses that suggest that *srn* has Notch-Delta dependent and independent defects,

consistent with a general defect in protein fucosylation. Our work suggests that several aspects of neural development are regulated by protein fucosylation, including the formation of synaptic circuitry, consistent with previous studies that have shown that protein fucosylation is a highly regulated process in the nervous system.

## Materials and Methods

### Zebrafish maintenance and mutants

Zebrafish were raised and maintained under standard conditions. The *srn* allele was previously described (Panzer et al., 2005). The *des*$^{b420}$ allele was obtained from Dr. Christine Beattie, *Tg(hsp70l:GAL4)* and *Tg(UAS:myc-notch1a-intra)* (Scheer et al., 2002) from Dr. Bruce Appel, and *dla*$^{hi781}$ and *mib*$^{hi904}$ alleles from Zebrafish International Resource Center, University of Oregon.

### Positional cloning of *srn*

Genetic mapping of mutant loci was performed as described (Willer et al., 2005). New simple sequence repeat (SSR) markers DKEY-25E12-SSR2 (forward, 5'-gcacacatgcatacgttcag-3'; reverse, 5'-tcccaaagtgaaagggtgag-3') and DKEY-177P2-SSR4 (forward, 5'-cctgagggtcaggagagtaatg-3'; reverse, 5'-gaactaacactttcacaaacaccaa-3') were used to define the interval that contained the mutation. PCR products containing the entire ORF of *gmds* (accession # NM_200489) were generated with the primers 5'-cggatgtgtttgcatccgta-3' and 5'-tcacatgaattaaacggcat-3' for both mutant and WT (WT) cDNAs, cloned into pCR 4-TOPO (Invitrogen), and sequenced to verify the presence of the mutation and for use in rescue experiments.

### GDP-fucose rescue

GDP-fucose (50 mM in water (pH = 7) with 0.1% phenol red as a tracer) was injected directly into 1-2 cell stage embryos collected from crosses of *srn* carriers.

**mRNA and morpholino injection**

*Gmds-gfp* mRNAs (WT and *srn*) were injected into embryos from WT and *srn* incrosses at the 1-2 cell stage at ~200 pg. The morpholino antisense oligonucleotide (Gene Tools) targeting the *gmds* exon5-intron5 junction (CGTATGTTTGCTGACCATAAGGCGA) was injected at the 1-2 cell stage at ~4 ng.

**RNA extraction and quantitative RT-PCR (qRT-PCR)**

RNA was extracted from a pool of 20 embryos with the RNeasy kit (Qiagen, Inc.). *hes5*, *neurod*, *her4*, *heyl*, *deltaC* and *b-actin1* were amplified with specific primers (Sup. Table 1). qRT-PCR was performed with the SuperScript® III Platinum® SYBR® Green One-Step qPCR Kit w/ROX (Invitrogen) and data was analyzed with 7500 Real-Time PCR System software (Applied Biosystems) using the $2^{-\Delta CT}$ method.

**Expression of Notch1a by heat-shock induction**

To induce expression of constitutively active Notch1a (Notch1a intracellular domain—NICD), embryos were collected from matings of heterozygous *Tg(hsp70l:GAL4)* and *Tg(UAS:myc-notch1a-intra)* adults and raised at 28.5°C. At 11

hpf, embryos were heat-shocked at 39°C for 30 minutes and then returned to 28.5°C until the desired stage of development (Shin et al., 2007).

**DAPT treatment**

Embryos were dechorionated with forceps at 6 hpf and placed in DAPT (N-[N-(3,5-Difluorophenacetyl-l-alanyl]-S-phenylglycine-t-butyl ester; Calbiochem) solution at 28.5°C until the appropriate stage, as previously described (Geling et al., 2002). For experiments, 50 μM (medium dose) and 100 μM (high dose) DAPT in embryo medium containing 1% DMSO was used. Control embryos were incubated in an equivalent concentration (1%) of DMSO.

**Immunostaining, AAL staining and labeling of retinotectal projections**

Embryos were anesthetized, fixed and immunostained as described previously (Panzer et al., 2005) using antibodies against SV2, Zn5, 3A10, F59 (all from Developmental Studies Hybridoma Bank, Univ. of Iowa) and/or goldfish GFAP (Nona et al., 1989) (gift from Drs. S. Nona and J. Scholes, Univ. of Sussex, United Kingdom) and a fluorescently conjugated secondary antibody (Jackson Labs, Inc.). To label AChRs, fluorescently conjugated a-bungarotoxin (Molecular Probes, Inc.) was used (Panzer et al., 2005). TUNEL staining was performed according to the manufacturer's instructions (Chemicon, Inc.). Fucosylated proteins were visualized in 48 hpf embryos using a biotinylated fucose-specific lectin, *Aleuria Aurantia* lectin (AAL; 20 μg/ml; Vector Labs) which recognizes fucose residues (Kochibe and Furukawa, 1980; Luhn et al., 2004) followed by Alexa 488 conjugated strepavidin (20 μg/mL; Molecular Probes). Retinal

ganglion cell axon projections to the optic tectum were labeled as described (Lee et al., 2004).

Unless otherwise stated, each immunostaining or dye labeled figure panel is a single plane projection of a confocal z-stack of 20-160 1 mm thick planes (Leica TCS 4D). Presynaptic vesicles, AChR clusters and the co-localization of these two markers were measured from using interactive software (Metamorph).

**Acknowledgements**

We thank Dr. Christine Beattie for providing the *deadly seven* mutant line, Dr. Bruce Appel for providing the *Tg(hsp70l:GAL4)* and *Tg(UAS:myc-notch1a-intra)* transgenic lines, Dr. Chi-Bin Chien for help with analyses of retinal ganglion cell axon targeting and branching, Drs. Sam Nona and John Scholes for providing the goldfish GFAP antibody, Ethan Hughes for help with quantification of neuromuscular synapses, Mrs. Marion Scott for technical assistance, and members of the Balice-Gordon lab for helpful discussions. Supported by NIH grant NS050524 to R. B.-G.

## Results

### *External phenotype, genetic cloning and mRNA rescue of slytherin*

From a small-scale genetic screen for defects in synaptogenesis, we previously identified *srn* due to its abnormal swimming behavior and increased number of neuromuscular synapses (Panzer et al., 2005). Externally, *srn* mutants exhibit a bent tail as early as 24 hpf, a phenotype that becomes progressively more severe (Fig. 1A), as well as a malformation of the hindbrain, which becomes apparent at 48 hpf (Fig. 1A, brackets).

The *srn* locus was mapped between SSLP markers z49730/z14955 and z14614 on chromosome 20, with marker z10756 having no recombinants (Fig. 1B). *Gmds* was found to contain a G to T transversion in the nucleotide sequence that produces a nonconservative glycine (G) to valine (V) substitution of amino acid 178 (G178V) in the short-chain dehydrogenase/reductase (SDR) domain (Fig. 1C, D, E). GMDS is highly conserved among various species at the amino acid level; for instance, the fish and human proteins are 87% identical.

RT-PCR analyses suggested that at least two splice variants exist in zebrafish *gmds*, with or without exon 4, which we name *gmds-L* and *gmds-S* respectively. Both splice variants are expressed in *srn* mutants and WT embryos (Fig. 1F). To confirm that *gmds* is the gene responsible for *srn* phenotypes, both splice variants of the WT and mutant *gmds* cDNAs were fused with *gfp* and were *in vitro* transcribed into mRNA and were injected into 1-2 cell stage embryos collected from *srn* incrosses. Compared to uninjected embryos, in which 29% of the embryos were mutants scored by external

abnormalities, the percentage of mutants dramatically decreased, to 5%, in embryos injected with WT *gmds-gfp* mRNAs (Fig. 1G; one-way ANOVA, followed by Dunn's pairwise comparison, $p < 0.05$). The percentage of mutants was unchanged in embryos injected with mutant *gmds-gfp* mRNAs (Fig. 1G). Moreover, when GMDS function was perturbed in WT embryos with a splice-blocking morpholino against exon5-intron5 junction, it phenocopied all the defects seen in *srn* mutants (see below and Sup. Fig. 3). These experiments confirm that *gmds* is the gene mutated in *srn*.

To examine the expression pattern of *gmds* mRNA, *in situ* hybridization was performed in embryos from 6 to 72 hours post fertilization (hpf; see Supplemental Information). From 6 to 12 hpf, *gmds* transcripts are expressed throughout the embryo (Sup. Fig. 1A). By 24 hpf, *gmds* transcripts are highly enriched in the CNS and are also present in somites (Sup. Fig. 1B). *Gmds* mRNA expression is present in the CNS at 48 and 72 hpf, with transcripts more abundant in brain than spinal cord (Sup. Fig. 1C, D). *Gmds* mRNA is also expressed in the PNS at 72 hpf, including in lateral line neuromasts (data not shown; (Thisse and Thisse, 2004)). The widespread expression of *gmds* during early embryogenesis suggests that this gene plays a role in many different tissues during development, while its localization in the CNS and PNS at later stages suggests that *gmds* also plays a role in neural development.

***Slytherin mutants exhibit reduced protein fucosylation***

GMDS is the first enzyme in the *de novo* fucose metabolism pathway, and it catalyzes the conversion of GDP-D-mannose to GDP-4-keto-6-D-deoxymannose, which

is further processed into GDP-fucose (Smith et al., 2002). GDP-fucose is then transported into the Golgi where it is used to fucosylate proteins, including Selectins, Notch and many others (Lowe, 2001; Moloney et al., 2000; Smith et al., 2002). Given the known function of GMDS in the protein fucosylation pathway, we reasoned that protein fucosylation in *srn* mutants would be compromised. Therefore, we performed AAL staining in 48 hpf WT and mutant embryos (Fig. 2).

In WT embryos, AAL staining was detected in many tissues (Fig. 2A). Interestingly, but not surprisingly, AAL staining is particularly strong in various neural tissues including olfactory bulb, retina, optic tectum, hindbrain and spinal cord (Fig. 2B-E), which prompted us to examine the potential phenotypes in these structures in *srn*. Moreover, at the neuromuscular junction (NMJ), AAL staining co-localizes with markers for pre- and postsynaptic specializations, such as SV2 and acetylcholine receptors (AChRs) (Fig. 2K-N). In contrast, AAL staining is strongly reduced in *srn* mutants (Fig. 2F-J, O-R), consistent with analyses of cells from CDG IIc patients (Lubke et al., 2001; Luhn et al., 2001), and of *Drosophila Gfr* mutants (Ishikawa et al., 2005). These studies show that protein fucosylation is dramatically reduced in the CNS and other tissues in *srn*, consistent with a loss of function of GMDS, confirming a prediction based on the modeling of the protein crystal structure (Supplemental Information and Sup. Fig. 2).

***Supplementation with GDP-fucose rescues slytherin phenotypes***

Since GMDS functions early in the fucose metabolism pathway, we reasoned that exogenous supply of its downstream products may circumvent the genetic defect in *srn*.

Therefore, 50 mM GDP-fucose was injected into 1-2 cell stage embryos collected from *srn* incrosses. Compared to uninjected embryos, the percentage of mutant embryos, as scored by external phenotypes (Fig. 3A), was dramatically reduced in GDP-fucose injected embryos (Fig. 3B). Moreover, AAL staining was similar to that in WT embryos at 48 hpf in many if not all tissues (Fig. 3C). Detailed phenotypic analyses further showed that GDP-fucose supplementation is sufficient to rescue neural defects in *srn* mutants (see below and Sup. Fig. 3). These strongly suggest that the absence of GDP-fucose, as a result of GMDS dysfunction, is the cause of the *srn* mutant phenotypes, rather than the accumulation of the substrate, GDP-mannose. Thus *srn* mutants display dysregulated protein fucosylation, as is seen in human CDG IIc patients, and that GDP-fucose supplementation restores fucosylation and rescues defects in *srn*.

***Slytherin mutants exhibit defects in neuron and glia number, patterning and axon outgrowth due to Notch-Delta signaling reduction***

Our previous work suggested that *srn* exhibited a neurogenic phenotype, specifically an increased number of primary motor neurons (Panzer et al., 2005), similar to that observed in Notch-Delta mutants. Analyses of *Drosophila Gfr* mutants suggested that Notch fucosylation is reduced, and that a reduction in Notch signaling might contribute to the pathogenesis in CDG IIc (Ishikawa et al., 2005). Therefore, we asked which if any neural defects in *srn* were similar to those observed in Notch-Delta mutants or in embryos treated with the g-secretase inhibitor DAPT to reduce Notch signaling.

We compared *srn* phenotypes with known Notch-Delta mutants, *des*$^{b420}$ (*deadly seven*, a nonsense mutation in *notch1a* yielding a truncated protein; Dr. C. Beattie, personal communication), *dla*$^{hi781}$ (*delta A*, an insertion in *delta A*, predicted to result in a truncated protein (Amsterdam et al., 2004)) and *mib*$^{hi904}$ (*mind bomb*, an insertion in an E3 ligase that targets Delta and other proteins for ubiquitination (Itoh et al., 2003), predicted to result in a truncated protein (Golling et al., 2002)). Below we describe phenotypes in each mutant in this order, which corresponds roughly to increasing disruption of Notch-Delta signaling.

First, we examined secondary motor neuron cell body number and patterning in the spinal cord, and axon projections in muscle. In *srn* mutants at 48 hpf and 72 hpf, while secondary motor neuron number is similar between *srn* mutant and WT embryos (Sup. Fig. 4), the patterning of these cells is aberrant. Secondary motor neuron cell bodies are clumped in *srn* mutants (Fig. 4A, B, second panel, dashed blue bracket), compared to the even spacing of cell bodies observed in WT embryos (Fig. 4A, B, top, solid blue bracket). The dorsally projecting secondary motor neuron nerve also is absent in *srn* mutants (Fig. 4A, B, second panel, dashed pink oval), consistent with increased secondary motor neuron cell death (Panzer et al., 2005). *des* mutants do not have defects in secondary motor neuron number or patterning, but do have motor axon pathfinding errors, possibly due to aberrant formation of somite boundary (Fig. 4A; (Gray et al., 2001)). *dla* mutants do not have defects in secondary motor neuron number, but have similar aberrant secondary motor neuron patterning as in *srn* mutants, without the loss of the dorsal projecting nerve (Fig. 4A, B, dashed blue bracket and solid pink oval,

respectively). *mib* mutants have aberrant secondary motor neuron number and patterning that is apparent at 48 and 72 hpf, as well as loss of the dorsal projecting nerve.

In the hindbrain and retina, similar defects in neuron number and patterning are present. In the hindbrain at 48 hpf, an increase in Mauthner neurons is observed in *srn*, *des* (as previously reported (Gray et al., 2001)), *dla* and *mib*, with the largest increase in Mauthner neuron number observed in *mib* (Fig. 4C, red brackets). Moreover, neuronal patterning in the hindbrain is severely perturbed in *srn* and in *mib* (data not shown). In the retina at 72 hpf, cell number and patterning appear grossly normal in *srn*, *des* and *dla*, but in *mib*, retinal ganglion cell number is reduced (Sup. Fig. 5A), probably due to increased cell death, as previously reported (Bernardos et al., 2005). These data suggest that reduced Notch-Delta signaling may account for some of the CNS and PNS phenotypes observed in *srn*.

Because deficiencies in Notch-Delta signaling have been shown to result in reduced gliogenesis (Appel and Eisen, 1998; Appel et al., 2001; Itoh et al., 2003; Park and Appel, 2003), we examined glial cells in the spinal cord, hindbrain and retina with GFAP immunostaining. In the spinal cord and hindbrain, the number of GFAP+ glial cells is reduced in *srn* mutants compared to WT embryos at 48-72 hpf (Fig. 4D and data not shown). A similar reduction in GFAP+ glial cells is also observed in *dla* and *mib*, but not in *des* (Fig. 4D and data not shown). In the retina, the number of radially oriented GFAP+ Muller cells is decreased in *srn* and *mib*, but not in *des* or *dla* (Sup. Fig. 5B). These results suggest that a reduction in Notch-Delta signaling may account for the reduction in glia observed in *srn* mutants.

We then compared *srn* phenotypes with those caused by Notch signaling inhibitor DAPT, a g-secretase inhibitor, that prevents intramembrane proteolysis of Notch and thus decreases the downstream signaling dependent on the Notch intracellular domain (Geling et al., 2002). While high dose of DAPT treatment resulted in phenotypes resembling those seen in *mib* (Fig. 4 and Sup. Fig. 5), medium dose DATP treatment closely recapitulated *srn* phenotypes, including the secondary motor neuron patterning defects and the reduction of GFAP+ glial cells in the spinal cord and retina (Fig. 4 and Sup. Fig. 5). These results substantiate the conclusion that a reduction in Notch-Delta signaling may account for the observed neural defects in *srn* mutants.

In order to test the synergy between *srn* and Notch-Delta deficiency, we initially sought to examine embryos double heterozygous for *srn* and *mib*, but these embryos did not show any obvious defects, likely because both single heterozygous embryos are haploid sufficient. Then we examine embryos double homozygous for *srn* and *mib*, reasoning since Notch signaling is mostly if not completely absent in *mib*,(Itoh et al., 2003), if *srn* defects are also caused by Notch signaling deficiency, introducing *srn* into *mib* background would not result in addictive effects, i.e. would not be more sever then *mib*. Indeed, *srn* and *mib* double mutants showed reduced secondary motor neurons and GFAP+ glial cells in the spinal cord, closely resembling those seen in *mib* (Fig. 5). Furthermore, using the same reasoning, we tested the synergy between *srn* and DAPT treatment. Similarly, in DAPT high dose treated embryos, in which Notch signaling is mostly if not completely blocked, *srn* did not add to the defects caused by DAPT alone, i.e. DAPT treated *srn* mutants resembled DAPT treated WT embryos showing similar reduced secondary motor neurons and GFAP+ glial cells in the spinal cord (Fig. 5).

These results are consistent with the hypothesis that Notch signaling deficiency underlies the neurogenesis and gliogenesis defects in *srn*.

In addition, we reasoned if the observed neural defects in *srn* results from reduced Notch signaling, overexpressing constitutively active Notch would be able to rescue these phenotypes. We utilized transgenic lines in which a constitutively active form of Notch, Notch1a intracellular domain (NICD) is overexpressed under the heat-shock promoter (*Tg(hsp70l:GAL4)*; *Tg(UAS:myc-notch1a-intra)*) (Scheer et al., 2002), recapitulated *srn* phenotypes in these embryos by morpholino knockdown of *gmds* transcripts, and examined whether NICD rescued the neural defects. Indeed, NICD overexpression rescued the secondary motor neuron patterning and reduced GFAP+ glial cells phenotypes in *gmds* morphants (Fig. 6). This result strongly suggests that Notch signaling deficiency underlies the neurogenesis and gliogenesis defects in *srn*.

To further assess whether Notch-Delta signaling is deficient in *srn* mutants, we examined the expression of several Notch effective genes, including *hes5*, *neurod*, *heyl*, *her4* and *deltaC* as direct readout of Notch transcriptional activation, using real time quantitative RT-PCR. It is known that *mib* embryos display a strong reduction in Notch signaling (Itoh et al., 2003) and *hes5*, *neurod*, *heyl*, *her4* and *deltaC* were collectively shown to be reduced in *mib* mutant fish and/or mice (Bae et al., 2005; Hegde et al., 2008; Koo et al., 2005; Zecchin et al., 2007). We found that, at 48 hpf, *hes5*, *neurod*, *heyl*, *her4* expression were significantly reduced in *srn* mutants, similar as in *mib* mutants, although to a lesser extent with *hes5*, *heyl* and *her4* (Fig. 7). This analysis confirms that Notch-Delta signaling is deficient in *srn*.

These results demonstrate important roles for protein fucosylation in neuro- and gliogenesis and patterning. Because these data show that defects in neuron and glia number, patterning and Notch effective genes expression in *srn* mutants are similar to those observed in Notch-Delta mutants, a reduction in Notch-Delta signaling caused by the lack of fucosylation accounts for these *srn* phenotypes.

***Slytherin mutants exhibit defects in neuromuscular synaptogenesis due to Notch-Delta signaling reduction***

Because *srn* was first identified in a screen for mutants with defects in neuromuscular synaptogenesis, we assessed the role of protein fucosylation and Notch-Delta signaling in neuromuscular synapse formation, particularly at the choice point where the first neuromuscular synapses are made(Panzer et al., 2005), using immunostaining. Choice point neuromuscular synapse size was increased at 24 hpf in *srn*, *des*, *dla*, *mib* and DAPT treated embryos (Fig. 8). At 48 hpf, *mib* and DAPT treated embryos showed no enlargement of choice point neuromuscular synapses, likely due to a reduced number of secondary motor neurons (Sup. Fig. 4). These defects are not due to defects in muscle fiber integrity or number (Sup. Fig. 6 and (Panzer et al., 2005)). These results show that dysregulated protein fucosylation in *srn* mutants resulted in an aberrant neuromuscular synaptogenesis that was phenocopied in Notch-Delta signaling deficient embryos, suggesting that Notch-Delta signaling plays an important and previously unappreciated role in modulating neuromuscular synapse formation.

***Slytherin mutants exhibit defects in CNS axon branching and synaptic connectivity that are independent of Notch-Delta signaling***

Phenotypic analyses showed that *srn* has several defects that are not present in the Notch-Delta mutants *des*, *dla* or *mib*, or DAPT treated embryos. In the retina, while overall cellular lamination is grossly normal in *srn* mutants (Fig. 9E, bottom left panel), the synaptic connections in the outer and inner plexiform layers (OPL and IPL) are dramatically altered, as shown by presynaptic labeling with SV2 antibody (Fig. 9A). In *srn* mutants at 48-72 hpf, the OPL and IPL synaptic layers are disorganized, and this is not seen in *des*, *dla* or medium dose DAPT treated embryos (Fig. 9A). In *mib* and high dose DAPT treated embryos, retinal ganglion and other cells die, resulting in a reduction in synapses throughout the retina (Fig. 9A). Thus *srn* displayed unique defects in CNS synaptic connectivity that are not phenocopied by Notch signaling deficient embryos, suggesting fucosylation of proteins other than those involved in Notch-Delta signaling are required to shape this neural circuitry.

Given that AAL staining showed high levels of protein fucosylation in optic tectum (Fig. 2), we examined whether retinal ganglion cell axon outgrowth to and branching within the optic tectum was affected in *srn* and other mutants. In *srn* mutants, retinal ganglion axons grow to the correct location within optic tectum (Fig. 9B), but their axons are aberrantly branched within the tectum (Fig. 9B, dashed white circle) and medial axon projections are shifted towards the midline (Fig. 9B, compare solid arrow and dashed arrow). These phenotypes are not present in *des*, *dla* or medium dose DAPT treated embryos (Fig. 9B). In *mib* and high dose DAPT treated embryos, the retinal

ganglion cell axon projection to optic tectum is dramatically reduced due to retinal ganglion cell death (Fig. 9B). *Mib* and high dose DAPT treated embryos also displayed retinal ganglion axon pathfinding errors at the optic chiasm (Fig. 9B, dashed square) and decreased branching within the optic tectum (Fig. 9B, dashed white circle). Furthermore, topographic mapping analyses, in which the dorsonasal (DN) and ventrotemporal (VT) retinal ganglion cell projections were differentially labeled (Fig. 9C, D) showed that, in *srn* mutants, the location of the DN and VT axon projections in the optic tectum is aberrant, and that these projections overlap aberrantly dorsally and laterally (Fig. 9D). Moreover, the cellular lamination and cell viability in the optic tectum was similar between *srn* and WT embryos at 72 hpf (Fig. 9E, middle left panels). These results suggest that signaling independent of the Notch-Delta pathway, but requiring protein fucosylation, modulates axon branching and synaptic patterning in the CNS.

## Discussion

We report that the *srn* mutation causes a loss of GMDS function, leading to a severe reduction in protein fucosylation, including that of Notch among many others. *Srn* displays increased neurogenesis, decreased gliogenesis, increased neuronal cell death, abnormal neuronal patterning, abnormal axon arborization, and abnormal neuromuscular and CNS synaptic connectivity, indicating that protein fucosylation plays an important role in several aspects of neural development.

### Notch-Delta signaling reduction underlies some but not all *srn* neural phenotypes

Our results suggest that both Notch-dependent and -independent mechanisms contribute to the neural phenotypes observed in *srn*. *Srn* mutants showed reduced Notch transcriptional activity, as assayed by *hes5*, *neurod*, *heyl*, and *her4* expression, increased primary motor neuron and Mauthner neuron number, decreased gliogenesis and abnormal neural patterning. These defects are phenocopied by Notch-Delta mutants and in embryos with reduced Notch signaling. That *mib* and Notch signaling inhibition by DAPT occlude *srn* defects, and that NICD overexpression rescues these *srn* phenotypes, strongly suggest that the dysregulated fucosylation of proteins in the Notch-Delta pathway accounts for these prominent neural defects in *srn* mutants. While the lack of anti-zebrafish Notch antibodies prevented direct analysis of Notch fucosylation, Notch is known to be fucosylated, and other proteins in the Notch-Delta pathway, including Delta, Serrate and Jagged, contain consensus sequence(s) for O-linked fucose modification (Harris and Spellman, 1993; Harris et al., 1993; Moloney and Haltiwanger, 1999). Notch

is also N-fucosylated, in which fucose is added to N-linked glycan side chains (Ishikawa et al., 2005; Jaeken and Matthijs, 2007; Sturla et al., 2003). Notch O- and N-fucosylation has been shown to be reduced in the Drosophila *Gfr* null (Ishikawa et al., 2005). It thus seems highly likely that the fucosylation of proteins in the Notch-Delta pathway is aberrant in *srn* mutants and that this accounts for some, but not all, *srn* neural phenotypes.

Interestingly, there is a hierarchy in the spectrum of *srn* and Notch-Delta mutant phenotypes. Phenotypes in *des*, except for the axon pathfinding errors, are weaker than those in *dla*, and both of these are weaker than *srn*. This is consistent with the hypothesis that many Notch-Delta factors, including Notch, Delta, Serrate and Jagged, require proper protein fucosylation and compromised fucosylation of these proteins may account for the wider spectrum of defects seen in *srn*. *Mib* mutants also displayed a wide range of defects, not seen in the other three mutants, consistent with the fact that mammalian Mib1 interacts with a number of proteins besides Delta and may serve as an integrator of multiple neuronal developmental pathways (Choe et al., 2007).

Moreover, our observation that *srn* and Notch-Delta mutants have increased neuromuscular synapses supports a previously underappreciated role for Notch-Delta signaling during synaptogenesis. Because primary motor neuron number is increased in *srn*, it is difficult to separate direct effects of Notch-Delta signaling on presynaptic differentiation from indirect effects on neurogenesis. The total number of motor neurons innervating trunk muscles actually decreases due to secondary motor neuron cell death (Panzer et al., 2005), while the increase in neuromuscular synapse number and size

persists. This strongly suggests that Notch-Delta signaling plays a role in synaptogenesis, independent of its role in neurogenesis.

Recent work has shown that reduced protein fucosylation, as a result of *gmds* mutation in *twohead* (*twd*) mutants, results in defects in the migration of vagus motor neuron progenitors (Ohata et al., 2009). Ohata and colleagues concluded that Notch signaling is unaltered in *twd* mutants, based on analyses of *her4* expression and analyses of hindbrain patterning and neuron number. However, neural phenotypes in *twd* were not compared with those in the Notch-Delta signaling mutants as assayed here, and analyses of additional Notch target genes in *twd* and migration phenotypes in Notch-Delta pathway mutants may be informative.

While deficiencies in Notch-Delta signaling underlie some *srn* phenotypes, other *srn* phenotypes are independent of this pathway. *Srn* mutants exhibit prominent defects in retinotectal connectivity that are quite different from those observed in Notch-Delta mutants such as *des* and *dla* in which no defects in retinotectal axon branching are observed, and from the dramatic reduction in retinal ganglion cell number and axon pathfinding observed in *mib.* We present several lines of evidence that strongly support the conclusion that some, but clearly not all, of the mechanisms underlying the neural phenotypes in *srn* are Notch-dependent. Future work will focus on identifying the fucosylated proteins that mediate the neural deficits that are independent of Notch-Delta signaling.

**_Srn_ as a zebrafish model for congenital disorders of glycosylation**

Over the last decade, a large number of human genetic diseases with aberrant glycoprotein synthesis have been identified and grouped as congenital disorders of glycosylation (CDG). Since glycosylation is essential for the function of many proteins, it is not surprising that disruption of glycosylation can lead to severe, multi-systemic phenotypes, including neurodevelopmental and cognitive disorders. In *srn* mutants, the *gmds* mutation largely abolishes the synthesis of GDP-fucose, resulting in reduction or elimination of both O-linked and N-linked fucosylation of Notch and many other proteins. Thus it is possible that disruption of O- as well as N-linked glycosylation of Notch and other proteins contributes to CDG IIc pathogenesis, although this has not been examined extensively in humans.

There are several reports of neural deficits in CDGIIc patients, including severe mental retardation, microcephaly, cortical atrophy, seizures, psychomotor retardation and hypotonia (Frydman et al. 1992; Lubke et al., 1999; Etzioni et al., 2002). These clinical observations are consistent with the CNS and PNS cellular phenotypes observed in *srn*. Given the advantage of performing imaging, genetic and pharmacological manipulations in zebrafish, *srn* will be a useful tool to guide future analyses in human CDG IIc patients and contribute to a better understanding of the mechanisms responsible for this devastating disorder that affects nervous system and other organ development.

## References

**Amsterdam, A., Nissen, R. M., Sun, Z., Swindell, E. C., Farrington, S. and Hopkins, N.** (2004). Identification of 315 genes essential for early zebrafish development. *Proc Natl Acad Sci U S A* **101**, 12792-7.

**Appel, B. and Eisen, J. S.** (1998). Regulation of neuronal specification in the zebrafish spinal cord by Delta function. *Development* **125**, 371-80.

**Appel, B., Givan, L. A. and Eisen, J. S.** (2001). Delta-Notch signaling and lateral inhibition in zebrafish spinal cord development. *BMC Dev Biol* **1**, 13.

**Bae, Y. K., Shimizu, T. and Hibi, M.** (2005). Patterning of proneuronal and inter-proneuronal domains by hairy- and enhancer of split-related genes in zebrafish neuroectoderm. *Development* **132**, 1375-85.

**Becker, D. J. and Lowe, J. B.** (1999). Leukocyte adhesion deficiency type II. *Biochim Biophys Acta* **1455**, 193-204.

**Bernardos, R. L., Lentz, S. I., Wolfe, M. S. and Raymond, P. A.** (2005). Notch-Delta signaling is required for spatial patterning and Muller glia differentiation in the zebrafish retina. *Dev Biol* **278**, 381-95.

**Choe, E. A., Liao, L., Zhou, J. Y., Cheng, D., Duong, D. M., Jin, P., Tsai, L. H. and Peng, J.** (2007). Neuronal morphogenesis is regulated by the interplay between cyclin-dependent kinase 5 and the ubiquitin ligase mind bomb 1. *J Neurosci* **27**, 9503-12.

**Etzioni, A., Sturla, L., Antonellis, A., Green, E. D., Gershoni-Baruch, R., Berninsone, P. M., Hirschberg, C. B. and Tonetti, M.** (2002). Leukocyte adhesion deficiency (LAD) type II/carbohydrate deficient glycoprotein (CDG) IIc founder effect and genotype/phenotype correlation. *Am J Med Genet* **110**, 131-5.

**Geling, A., Steiner, H., Willem, M., Bally-Cuif, L. and Haass, C.** (2002). A gamma-secretase inhibitor blocks Notch signaling in vivo and causes a severe neurogenic phenotype in zebrafish. *EMBO Rep* **3**, 688-94.

**Golling, G., Amsterdam, A., Sun, Z., Antonelli, M., Maldonado, E., Chen, W., Burgess, S., Haldi, M., Artzt, K., Farrington, S. et al.** (2002). Insertional mutagenesis in zebrafish rapidly identifies genes essential for early vertebrate development. *Nat Genet* **31**, 135-40.

**Gray, M., Moens, C. B., Amacher, S. L., Eisen, J. S. and Beattie, C. E.** (2001). Zebrafish deadly seven functions in neurogenesis. *Dev Biol* **237**, 306-23.

**Harris, R. J. and Spellman, M. W.** (1993). O-linked fucose and other post-translational modifications unique to EGF modules. *Glycobiology* **3**, 219-24.

**Harris, R. J., van Halbeek, H., Glushka, J., Basa, L. J., Ling, V. T., Smith, K. J. and Spellman, M. W.** (1993). Identification and structural analysis of the tetrasaccharide NeuAc alpha(2-->6)Gal beta(1-->4)GlcNAc beta(1-->3)Fuc alpha 1-->O-linked to serine 61 of human factor IX. *Biochemistry* **32**, 6539-47.

**Hegde, A., Qiu, N. C., Qiu, X., Ho, S. H., Tay, K. Q., George, J., Ng, F. S., Govindarajan, K. R., Gong, Z., Mathavan, S. et al.** (2008). Genomewide expression

analysis in zebrafish mind bomb alleles with pancreas defects of different severity identifies putative Notch responsive genes. *PLoS ONE* **3**, e1479.

**Hellbusch, C. C., Sperandio, M., Frommhold, D., Yakubenia, S., Wild, M. K., Popovici, D., Vestweber, D., Grone, H. J., von Figura, K., Lubke, T. et al.** (2007). Golgi GDP-fucose transporter-deficient mice mimic congenital disorder of glycosylation IIc/leukocyte adhesion deficiency II. *J Biol Chem* **282**, 10762-72.

**Ishikawa, H. O., Higashi, S., Ayukawa, T., Sasamura, T., Kitagawa, M., Harigaya, K., Aoki, K., Ishida, N., Sanai, Y. and Matsuno, K.** (2005). Notch deficiency implicated in the pathogenesis of congenital disorder of glycosylation IIc. *Proc Natl Acad Sci U S A* **102**, 18532-7.

**Itoh, M., Kim, C. H., Palardy, G., Oda, T., Jiang, Y. J., Maust, D., Yeo, S. Y., Lorick, K., Wright, G. J., Ariza-McNaughton, L. et al.** (2003). Mind bomb is a ubiquitin ligase that is essential for efficient activation of Notch signaling by Delta. *Dev Cell* **4**, 67-82.

**Jaeken, J. and Matthijs, G.** (2007). Congenital disorders of glycosylation: a rapidly expanding disease family. *Annu Rev Genomics Hum Genet* **8**, 261-78.

**Kochibe, N. and Furukawa, K.** (1980). Purification and properties of a novel fucose-specific hemagglutinin of Aleuria aurantia. *Biochemistry* **19**, 2841-6.

**Koo, B. K., Lim, H. S., Song, R., Yoon, M. J., Yoon, K. J., Moon, J. S., Kim, Y. W., Kwon, M. C., Yoo, K. W., Kong, M. P. et al.** (2005). Mind bomb 1 is essential for generating functional Notch ligands to activate Notch. *Development* **132**, 3459-70.

**Lee, J. S., von der Hardt, S., Rusch, M. A., Stringer, S. E., Stickney, H. L., Talbot, W. S., Geisler, R., Nusslein-Volhard, C., Selleck, S. B., Chien, C. B. et al.** (2004). Axon sorting in the optic tract requires HSPG synthesis by ext2 (dackel) and extl3 (boxer). *Neuron* **44**, 947-60.

**Lowe, J. B.** (2001). Glycosylation, immunity, and autoimmunity. *Cell* **104**, 809-12.

**Lubke, T., Marquardt, T., Etzioni, A., Hartmann, E., von Figura, K. and Korner, C.** (2001). Complementation cloning identifies CDG-IIc, a new type of congenital disorders of glycosylation, as a GDP-fucose transporter deficiency. *Nat Genet* **28**, 73-6.

**Luhn, K., Laskowska, A., Pielage, J., Klambt, C., Ipe, U., Vestweber, D. and Wild, M. K.** (2004). Identification and molecular cloning of a functional GDP-fucose transporter in Drosophila melanogaster. *Exp Cell Res* **301**, 242-50.

**Luhn, K., Wild, M. K., Eckhardt, M., Gerardy-Schahn, R. and Vestweber, D.** (2001). The gene defective in leukocyte adhesion deficiency II encodes a putative GDP-fucose transporter. *Nat Genet* **28**, 69-72.

**Moloney, D. J. and Haltiwanger, R. S.** (1999). The O-linked fucose glycosylation pathway: identification and characterization of a uridine diphosphoglucose: fucose-beta1,3-glucosyltransferase activity from Chinese hamster ovary cells. *Glycobiology* **9**, 679-87.

**Moloney, D. J., Panin, V. M., Johnston, S. H., Chen, J., Shao, L., Wilson, R., Wang, Y., Stanley, P., Irvine, K. D., Haltiwanger, R. S. et al.** (2000). Fringe is a glycosyltransferase that modifies Notch. *Nature* **406**, 369-75.

**Nona, S. N., Shehab, S. A., Stafford, C. A. and Cronly-Dillon, J. R.** (1989). Glial fibrillary acidic protein (GFAP) from goldfish: its localisation in visual pathway. *Glia* **2**, 189-200.

**Ohata, S., Kinoshita, S., Aoki, R., Tanaka, H., Wada, H., Tsuruoka-Kinoshita, S., Tsuboi, T., Watabe, S. and Okamoto, H.** (2009). Neuroepithelial cells require fucosylated glycans to guide the migration of vagus motor neuron progenitors in the developing zebrafish hindbrain. *Development* **136**, 1653-63.

**Panzer, J. A., Gibbs, S. M., Dosch, R., Wagner, D., Mullins, M. C., Granato, M. and Balice-Gordon, R. J.** (2005). Neuromuscular synaptogenesis in wild-type and mutant zebrafish. *Dev Biol* **285**, 340-57.

**Park, H. C. and Appel, B.** (2003). Delta-Notch signaling regulates oligodendrocyte specification. *Development* **130**, 3747-55.

**Salama-Cohen, P., Arevalo, M. A., Grantyn, R. and Rodriguez-Tebar, A.** (2006). Notch and NGF/p75NTR control dendrite morphology and the balance of excitatory/inhibitory synaptic input to hippocampal neurones through Neurogenin 3. *J Neurochem* **97**, 1269-78.

**Scheer, N., Riedl, I., Warren, J. T., Kuwada, J. Y. and Campos-Ortega, J. A.** (2002). A quantitative analysis of the kinetics of Gal4 activator and effector gene expression in the zebrafish. *Mech Dev* **112**, 9-14.

**Shin, J., Poling, J., Park, H. C. and Appel, B.** (2007). Notch signaling regulates neural precursor allocation and binary neuronal fate decisions in zebrafish. *Development* **134**, 1911-20.

**Smith, P. L., Myers, J. T., Rogers, C. E., Zhou, L., Petryniak, B., Becker, D. J., Homeister, J. W. and Lowe, J. B.** (2002). Conditional control of selectin ligand expression and global fucosylation events in mice with a targeted mutation at the FX locus. *J Cell Biol* **158**, 801-15.

**Sturla, L., Rampal, R., Haltiwanger, R. S., Fruscione, F., Etzioni, A. and Tonetti, M.** (2003). Differential terminal fucosylation of N-linked glycans versus protein O-fucosylation in leukocyte adhesion deficiency type II (CDG IIc). *J Biol Chem* **278**, 26727-33.

**Thisse, B. and Thisse, C.** (2004). Fast Release Clones: A High Throughput Expression Analysis. *ZFIN Direct Data Submission*.

**Wang, Y., Chan, S. L., Miele, L., Yao, P. J., Mackes, J., Ingram, D. K., Mattson, M. P. and Furukawa, K.** (2004). Involvement of Notch signaling in hippocampal synaptic plasticity. *Proc Natl Acad Sci U S A* **101**, 9458-62.

**Willer, G. B., Lee, V. M., Gregg, R. G. and Link, B. A.** (2005). Analysis of the Zebrafish perplexed mutation reveals tissue-specific roles for de novo pyrimidine synthesis during development. *Genetics* **170**, 1827-37.

**Yoon, K. and Gaiano, N.** (2005). Notch signaling in the mammalian central nervous system: insights from mouse mutants. *Nat Neurosci* **8**, 709-15.

**Zecchin, E., Filippi, A., Biemar, F., Tiso, N., Pauls, S., Ellertsdottir, E., Gnugge, L., Bortolussi, M., Driever, W. and Argenton, F.** (2007). Distinct delta and jagged genes control sequential segregation of pancreatic cell types from precursor pools in zebrafish. *Dev Biol* **301**, 192-204.

**Figures and Legends**

**Figure 1. *Slytherin* external phenotype, genotype, cloning and mRNA rescue of *srn* mutants.**

**A.** External *srn* phenotypes at 48 hpf include a bent tail (80% bent dorsally (N = 534 embryos, 8 carrier pairs) and aberrant hindbrain formation (brackets). Scale bar = 100 μm. **B.** Genetic and physical map of the *srn* locus (red arrow), including SSLP markers, number of recombinants, BAC clones and megabase positions from Ensembl Zv7. **C, D.** *Gmds* mutation in *srn* is a G to T mutation (C, red box) resulting in a Glycine to Valine conversion (D, red box). The amino acid sequence of GMDS is highly conserved among several species, from E. coli to human. **E.** Schematic location of *srn* mutation in the short-chain dehydrogenase/reductase (SDR) domain of GMDS. **F.** Two splice variants exist in *gmds* mRNA, with (*gmds-L,* 377 aa) or without (*gmds-S*, 370 aa) exon 4. *Gmds* alternative splicing is not altered in *srn* mutants. **G.** Injection of *gmds* mRNA rescues *srn* mutants. Compared to uninjected embryos, 28.6 ± 1.2% of the embryos were mutant when scored by external phenotypes (N = 3413 embryos, 27 carrier pairs). In embryos injected with WT *gmds-gfp* mRNA, the percentage of mutants scored by external phenotypes was significantly decreased, to ca. 5% (*gmds-wtL-gfp* 5.4 ± 2.5%, N = 401 embryos, 3 carrier pairs; *gmds-wtS-gfp* 5.1 ± 0.6%, N = 587 embryos, 4 carrier pairs; one-way ANOVA, followed by Dunn's pairwise comparison, $p < 0.05$). The percentage of embryos with mutant external phenotypes was unchanged in embryos injected with mutant *gmds-gfp* mRNA (*gmds-srnL-gfp* 30.2 ± 0.9%, N = 387 embryos, 3

carrier pairs; *gmds-wtS-gfp* 25.1 ± 1.9%, N = 516 embryos, 4 carrier pairs). This mRNA rescue experiment confirms that *gmds* is the gene responsible for *srn* mutation.

**Figure 1. *Slytherin* external phenotype, genotype, cloning and mRNA rescue of *srn* mutants.**

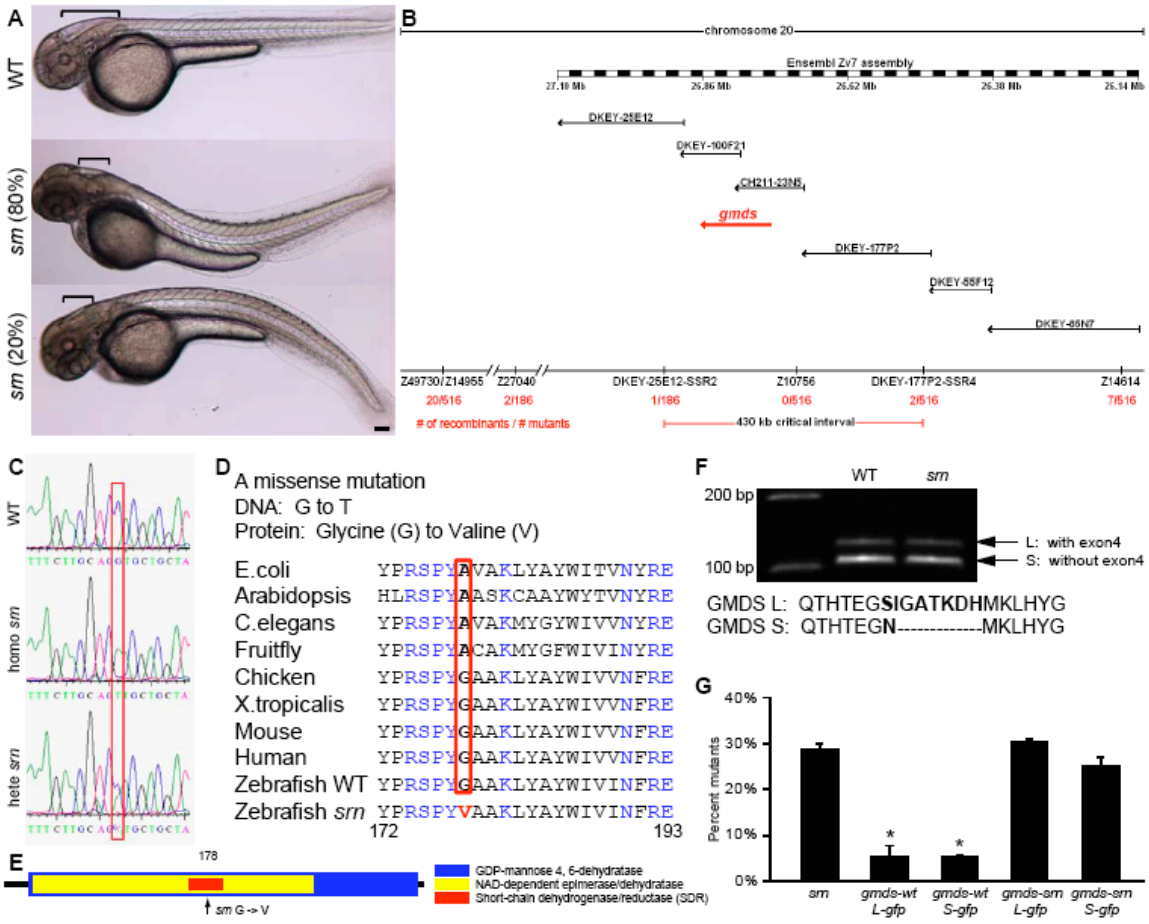

**Figure 2. *slytherin* mutants exhibit reduced protein fucosylation as measured by AAL staining.**

**A.** AAL staining of WT embryos at 48 hpf showed that protein fucosylation is present throughout the embryo (10-15 embryos / 2-3 adult pairs for all analyses). **B-E**. Protein fucosylation is prominent in neural tissues such as the retina (lateral view), optic tectum (dorsal view), hindbrain (lateral view), spinal cord (lateral view) and neuromuscular synapses (lateral view of axial muscle). **F.** Protein fucosylation is dramatically reduced in *srn* mutants. Scale bar = 20 μm. **G-J**. Reduced protein fucosylation in retina, optic tectum, hindbrain, spinal cord and neuromuscular synapses, as well as in other tissues. Scale bar = 20 μm. **K**. Protein fucosylation at neuromuscular synapses in WT embryos at 48 hpf, as shown by the colocalization of AAL staining (green) with markers for presynaptic axons and nerve terminals (SV2, red) and postsynaptic AChR clusters (a-bungarotoxin, blue). **L-N.** Higher magnification of boxed region in **K.** **O.** Protein fucosylation is reduced in *srn* neuromuscular synapses. Scale bar = 20 μm. **P-R**. Higher magnification of boxed region in **O.** Synapse area is significantly increased in *srn* mutants, especially at the choice point (compare dashed bracket in Q to solid bracket in M). Scale bar = 20 μm.

**Figure 2. *slytherin* mutants exhibit reduced protein fucosylation as measured by AAL staining.**

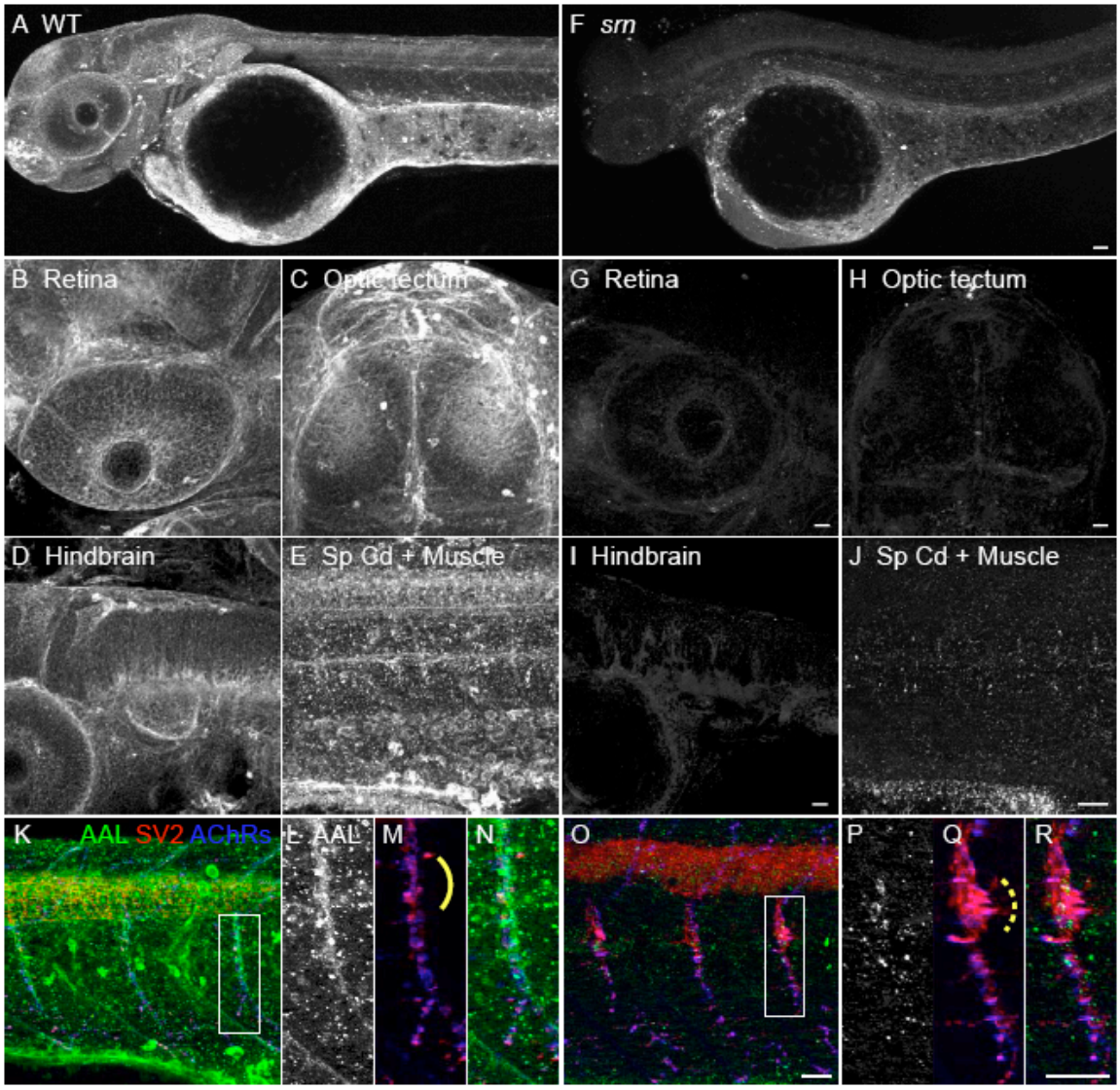

**Figure 3. Supplementation with exogenous GDP-fucose rescues *srn* external phenotypes and restores AAL staining.**

**A.** External *srn* phenotypes including bent tail and aberrant hindbrain formation (bracket) are rescued by GDP-fucose supplementation (N = 3 embryos). Scale bar = 100 µm. **B.** GDP-fucose injection significantly reduced the percentage of mutants from 28.6 ± 1.2% to 8.4 ± 2.7% (N = 576 embryos, 4 carrier pairs; Student's test, $p < 0.0001$). **C.** After GDP-fucose supplementation (N = 2 embryos), protein fucosylation as assessed by AAL staining at 48 hpf is rescued throughout *srn* embryos, to levels similar to those seen in WT embryos. Scale bar = 100 µm.

**Figure 3. Supplementation with exogenous GDP-fucose rescues *srn* external phenotypes and restores AAL staining.**

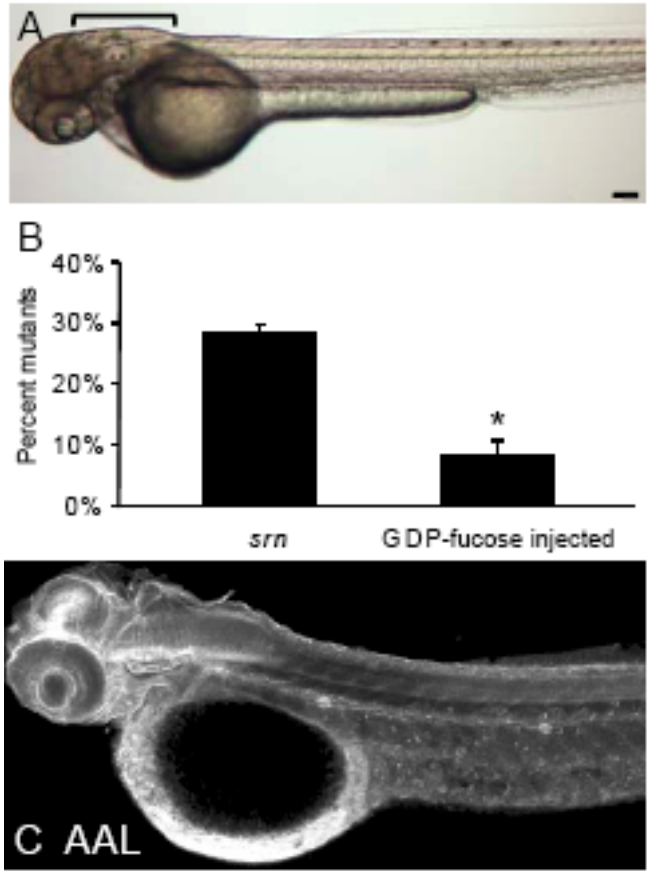

**Figure 4. Reduction in Notch-Delta signaling accounts for some *srn* phenotypes.**

**A, B.** Secondary motor neuron cell body number and patterning assayed with Zn-5 immunostaining (18 embryos / 3 carrier pairs for each). **B.** Higher magnification of boxed region in **A.** At 48 - 72 hpf, secondary motor neuron number is similar in *srn* and WT (Sup. Fig. 4), but the patterning of these cells is aberrant in *srn* embryos. Secondary motor neuron cell bodies are clumped in *srn* mutants (dashed blue bracket) compared to WT embryos (solid blue bracket). *dla* mutants do not have defects in secondary motor neuron number (Sup. Fig. 4), and have aberrant secondary motor neuron patterning as in *srn* mutants (dashed blue bracket). *mib* mutants and high dose DAPT treated embryos have aberrant secondary motor neuron number (Sup. Fig. 4) and patterning (dashed blue bracket). Medium dose DAPT treated embryos show aberrant secondary motor neuron patterning defects (dashed blue bracket), without an obvious change in cell number (Sup. Fig. 4), as in *srn*. The dorsal secondary motor neuron is absent in *srn* mutants (dashed pink oval) compared to WT (solid pink oval), consistent with increased secondary motor neuron cell death; is present in *dla* and *des* mutants (solid pink oval); *des* also has other motor axon pathfinding errors. In *mib* mutants and high and medium dose DAPT treated embryos, the dorsal projecting nerve is absent (dashed pink oval). **C.** In WT embryos at 48 hpf, a pair of Mauthner neurons is present (dorsal view of hindbrain). In *srn*, *des*, *dla*, *mib* and high dose DAPT treated embryos, Mauthner neuron number is increased (dashed red brackets), with the largest increase observed in *mib* (12 embryos, 3 carrier pairs for each). **D.** In the spinal cord, the number of GFAP+ glial cells is reduced in *srn* and *dla* mutants and medium dose DAPT treated embryos compared to WT and *des* embryos at

48-72 hpf. In *mib* and high dose DAPT treated embryos, a more dramatic reduction is observed. 18 embryos / 3 carrier pairs for each. Scale bars = 40 μm.

**Figure 4. Reduction in Notch-Delta signaling accounts for some *srn* phenotypes.**

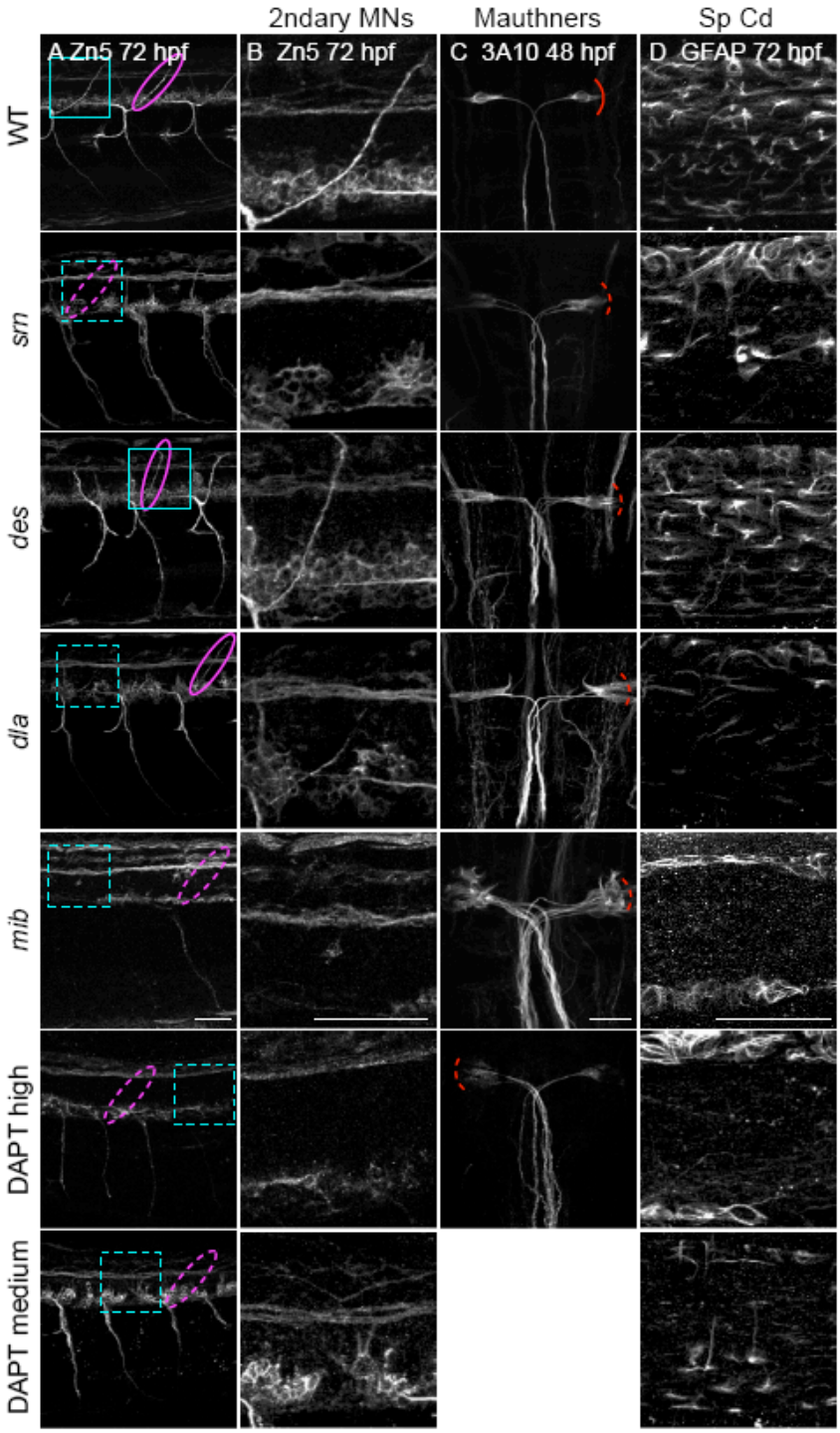

**Figure 5. *mib* and DAPT treatment exclude *srn* phenotypes.**

**A-C.** *mib* excludes *srn* phenotypes. **A.** AAL staining is reduced in *srn* and *srn* + *mib* double mutants, but not in *mib*. **B.** *srn* + *mib* double mutants showed reduction of secondary motor neurons, more severe than *srn* but similar to *mib* alone. **C.** *srn* + *mib* double mutants have reduced GFAP+ glia, more severe than *srn*, but similar to *mib* alone. 15 embryos / 2 carrier pairs for each. Scale bar = 40 μm. **D-F.** DAPT treatment excludes *srn* phenotypes. **D.** AAL staining is reduced in *srn* and *srn* mutants treated with DAPT, but not in DAPT treated embryos. **E.** *srn* mutants treated with DAPT showed reduction of secondary motor neurons, more severe than *srn* but similar to DAPT treated embryos. **F.** *srn* mutants treated DAPT showed reduction of GFAP+ glia, more severe than *srn*, but similar to DAPT treated embryos. 10 embryos / 2 carrier pairs for each. Scale bar = 40 μm.

**Figure 5. *mib* and DAPT treatment exclude *srn* phenotypes.**

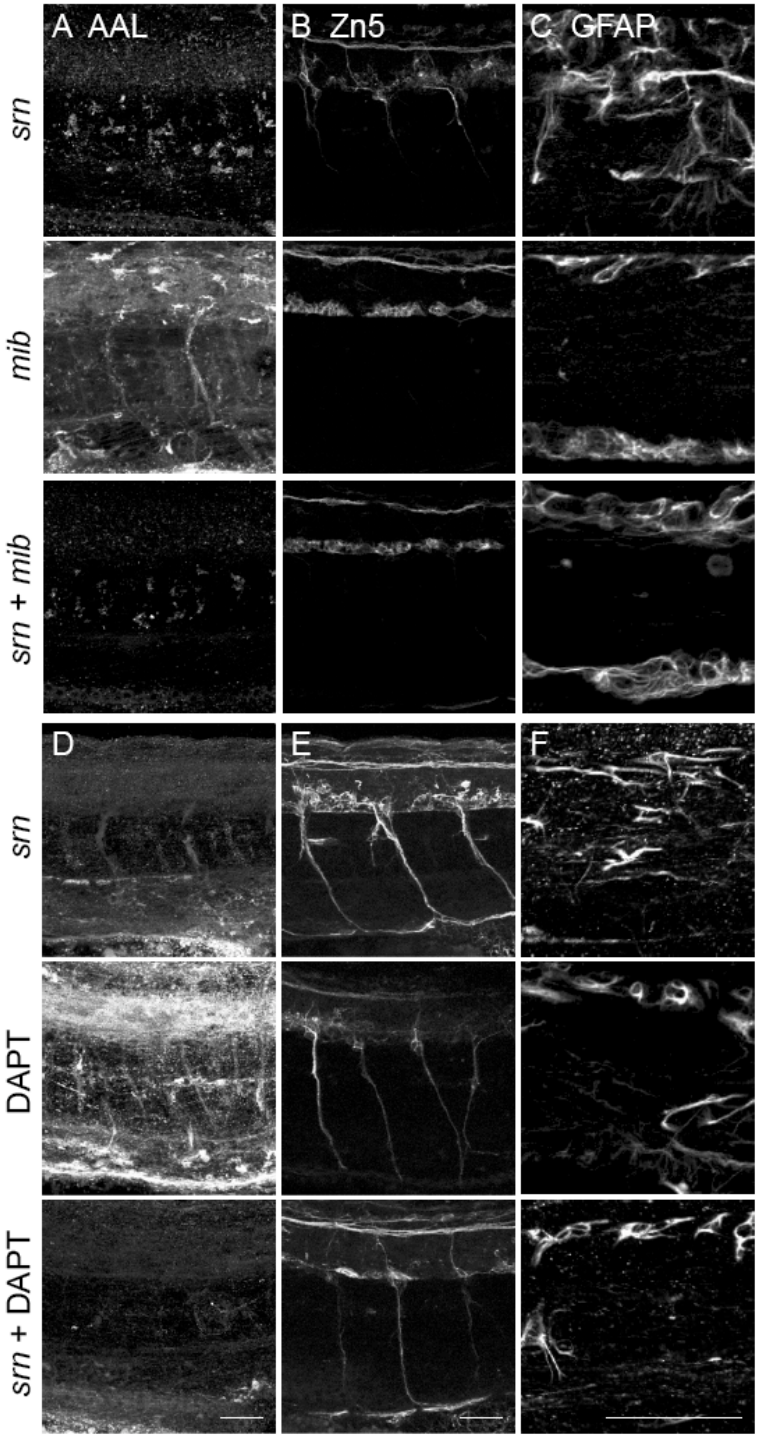

**Figure 6. NICD rescues *srn* neuro- and gliogenesis phenotypes.**

**A.** AAL staining is reduced in *srn*, *gmds* morphants and *gmds* morphants overexpressing NICD, but not in WT embryos or WT embryos overexpressing NICD. **B.** WT and WT overexpressing NICD had normal secondary motor neuron patterning. *srn* and *gmds* MO showed secondary motor neuron patterning defects which was rescued by NICD overexpression in *gmds* morphants. **C.** WT and WT overexpressing NICD had normal GFAP+ glia cells in spinal cord. *srn* and *gmds* morphants had reduced GFAP+ glia cells, which was rescued by NICD overexpression in *gmds* morphants. At least 10 embryos in each experiment were assessed. Scale bar = 40 μm.

**Figure 6. NICD rescues *srn* neuro- and gliogenesis phenotypes.**

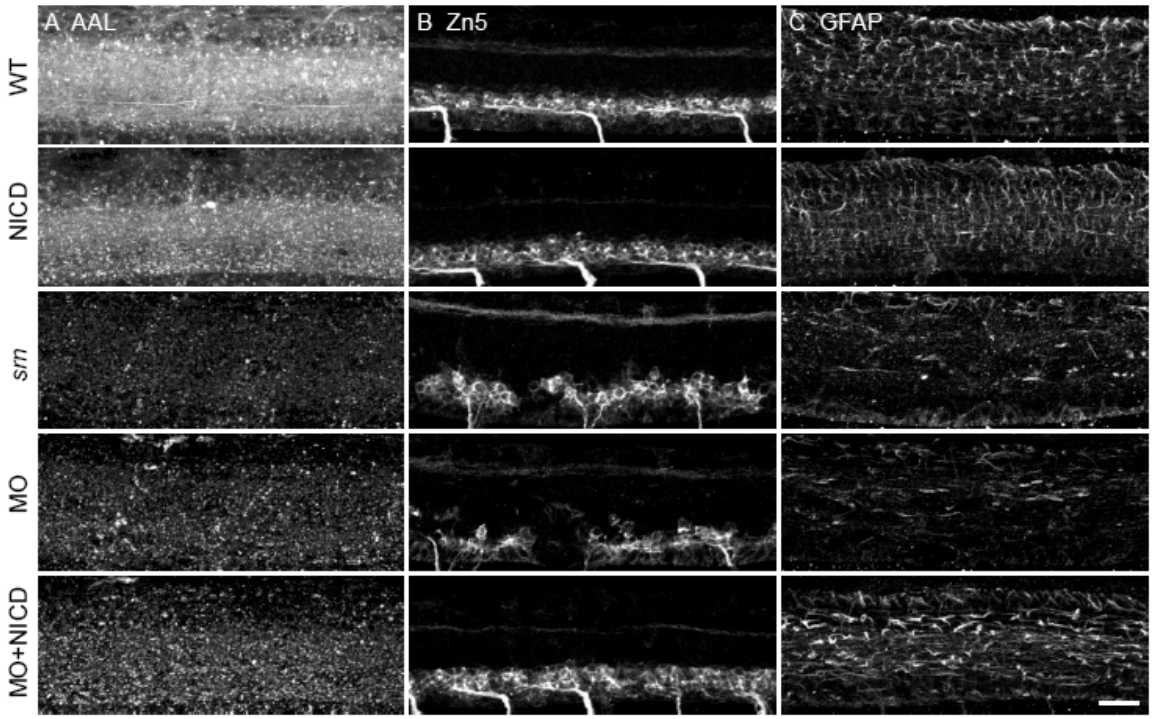

**Figure 7. *srn* mutants showed aberrant expression of Notch responsive genes similar to *mib* mutants.**

qRT-PCR assessment of fold change in *hes5*, *neurod*, *heyl*, *her4* and *deltaC* expression in WT, *srn* and *mib* mutant embryos at 48 hpf, normalized to *b-actin1*. *hes5*, *neurod*, *heyl*, and *her4* expression is dramatically reduced in *srn*, similar to those in *mib*. The reduction in *hes5*, *heyl* and *her4* is more dramatic in *mib*. (N = 3-5 experiments, 20 embryos each, one-way ANOVA, Bonferroni's Multiple Comparison Test, ** $p < 0.001$, * $p < 0.5$).

**Figure 7. *srn* mutants showed aberrant expression of Notch responsive genes similar to *mib* mutants.**

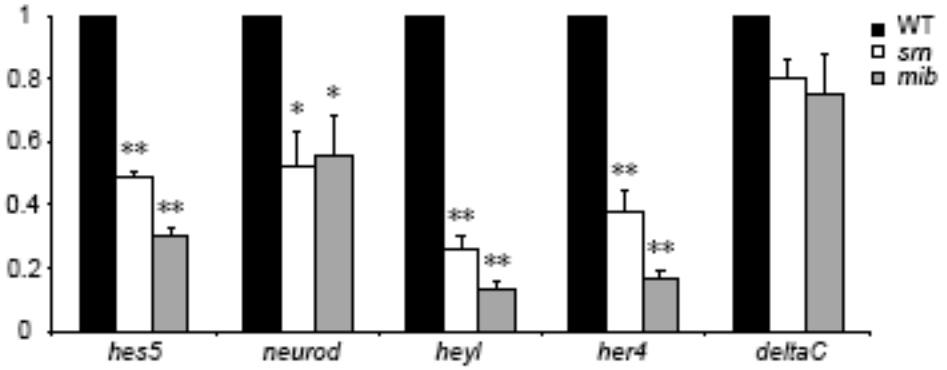

**Figure 8. *Slytherin* mutants exhibit defects in neuromuscular synaptogenesis due in part to reduction in Notch-Delta signaling.**

**A- X.** Presynaptic terminals (green) and postsynaptic AChR clusters (red) in 24 and 48 embryos from WT (A, G, M, S), *srn* (B, H, N, T), *des* (C, I, O, U), *dla* (D, J, P, V), *mib* (E, K, Q, W) and DAPT treated embryos (F, L, R, X). Boxed regions are shown at higher magnification in the panels below at 24 (G – L) and 48 hpf (S - X). 3 hemisegments in each of 20 embryos / 3 carrier pairs for each. Scale bar = 20 mm. **Y.** Presynaptic terminal, axon and synapse area at the choice point was significantly increased in all mutants, except in *mib* and DAPT treated embryos at 48 hpf, compared to WT (one-way ANOVA, Bonferroni's Multiple Comparison Test, ** $p < 0.01$, *** $p < 0.001$).

**Figure 8.** ***Slytherin*** **mutants exhibit defects in neuromuscular synaptogenesis due in part to reduction in Notch-Delta signaling.**

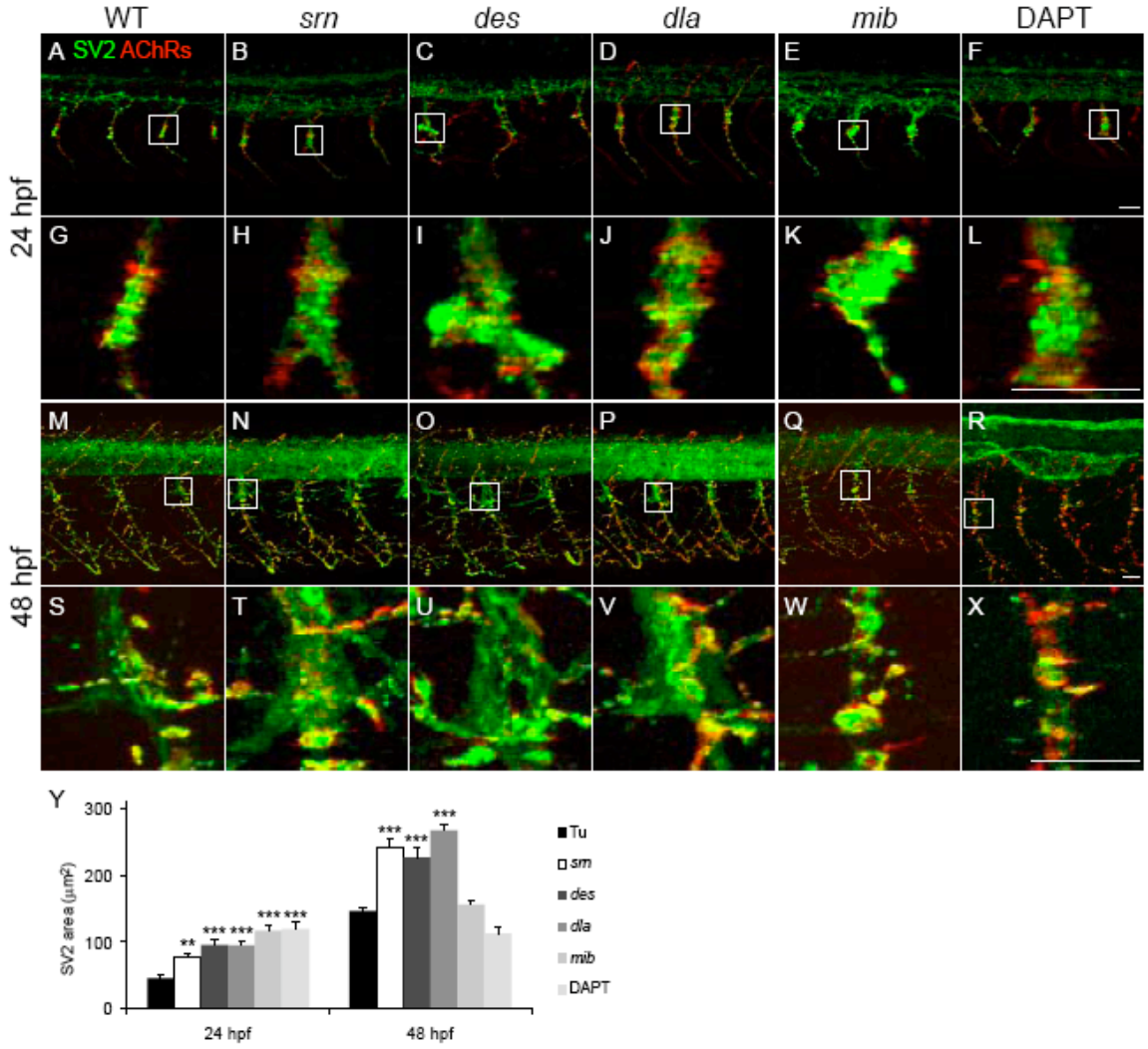

**Figure 9. *Slytherin* mutants exhibit defects in axon branching and CNS synaptic connectivity that are independent of Notch-Delta signaling.**

**A.** In *srn* mutants at 72 hpf, the OPL and IPL are disorganized, and this is not seen in *des* or *dla* mutants. In *mib* mutants, retinal ganglion and other cells die, resulting in a reduction in synapses throughout the retina (rightmost panel). 8 embryos / 2 carrier pairs for each. Scale bar = 20 mm. **B.** In *srn* mutants, retinal ganglion cell axons grow out to the optic chiasm and to optic tectum, but axon branches are aberrantly distributed within optic tectum (dashed white circle). Virtually all of the retina was dye labeled, and this labeling pattern was consistent from experiment to experiment, suggesting that this pattern is not due to incomplete dye uptake or labeling in *srn* mutants. In addition, medial axon projections are shifted towards the midline (compare solid arrow and dashed arrow). These phenotypes are not present in *des* or *dla* mutants, and are also different from *mib* mutants, in which retinal ganglion cell axonal projections to optic tectum are dramatically reduced, as a consequence of retinal ganglion cell death. *Mib* mutants also displayed retinal ganglion axon pathfinding errors at the optic chiasm, and axons were observed to branch in regions anterior to the optic chiasm (dashed square) while branching within optic tectum was dramatically reduced (dashed white circle). 15 embryos / 3 carrier pairs for each. Scale bar = 20 mm. **C, D.** Topographic mapping of the retinal ganglion cell axon projection to optic tectum, in which the dorsonasal (DN) and ventrotemporal (VT) retinal ganglion cell projections are differentially labeled with DiI and DiD, showed that the location of the DN and VT axon projections within the optic tectum is aberrant in *srn* mutants, and that these projects overlap aberrantly both dorsally (C) and laterally (D). 8 embryos / 2 carrier pairs for each. Scale bar = 20 mm. **E.** In the

retina and optic tectum (white circle), the overall cellular lamination pattern as assessed by DAPI staining is grossly normal in *srn* mutants (compare bottom left panels, WT and *srn*). TUNEL staining showed that increased cell death was observed in the retina of *srn* mutants compared to WT embryos at 72 hpf, and no difference in cell death in the optic tectum was observed in *srn* mutants compared to WT embryos at 72 hpf (color overlay, right most panels; 2-3 embryos / 1 carrier pair). Scale bar = 20 mm.

**Figure 9. *Slytherin* mutants exhibit defects in axon branching and CNS synaptic connectivity that are independent of Notch-Delta signaling.**

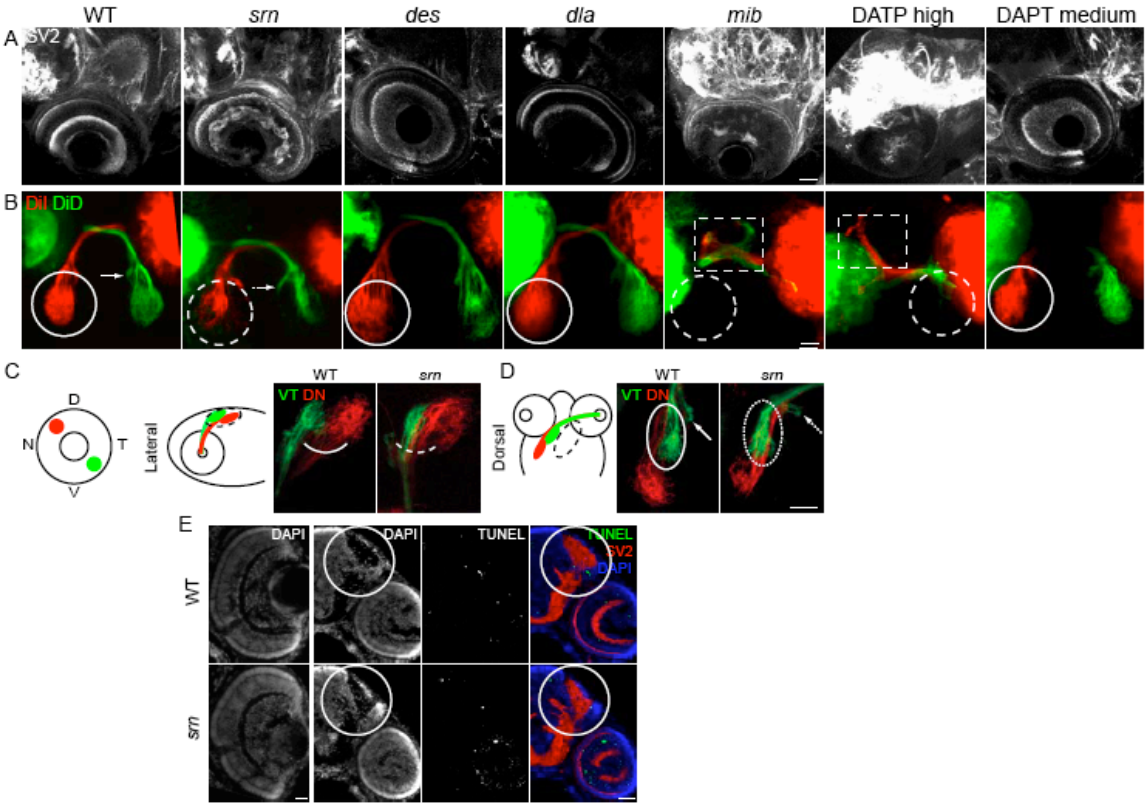

## Supplemental Materials and Methods, Results and Figure Legends

### Materials and Methods

#### *Analysis of GMDS structure*

In the absence of a three dimensional structure of zebrafish GMDS, we used a model constructed using molecular modeling to explain the effects of the Glycine 178 to Valine mutation on the activity of the enzyme. A search of the Protein Data Bank database (www.pdb.org) with either the wild type or mutant zebrafish GMDS sequence, using the software MODELLER (Sali and Blundell, 1990; Sali and Blundell, 1993; Sali et al., 1990), identified the unpublished crystal structure of the human GMDS/GDP/NDP complex as its closest homologue (87% sequence identity) and produced the corresponding zebrafish GMDS models. To understand how the *srn* mutation causes what appears to be a near-complete loss of function, the wild type zebrafish GMDS was overlain with the mutant zebrafish GMDS structures using PYMOL.

## Results

### *Structure of wild type and mutant GMDS*

Because of this high degree of amino acid sequence conservation between zebrafish and human GMDS, we reasoned that it would be informative to superimpose the zebrafish GMDS sequence onto the human GMDS crystal structure. Human GMDS was co-crystallized with GDP (www.pdb.org), and several ordered waters were evident in the structure that seem to co-ordinate GDP to Glu158 to hold GDP-mannose in place (Sup. Fig. 2). When Gly178 was mutated to Valine, recapitulating the *srn* mutation, the R group from the Valine appears to come into close proximity with the carbonyl backbone of Glu158. To determine whether this would disrupt the location of this amino acid, a local energy minimization computer simulation was performed to compare wild type zebrafish GMDS with the *srn* mutation, mapped onto the human crystal structure. The mutant zebrafish GMDS shows that the insertion of the larger hydrophobic side chain of Valine in this position displaces E158 towards the GDP molecule, thus disrupting the canonical interactions made between the protein and GDP (Sup. Fig. 2). This shift may impact the binding of GDP-mannose, providing a clue to the molecular dysfunction of the protein.

**Supplemental Figures and Legends**

**Supplemental Table 1. Primers used for qRT-PCR.**

| Gene name | Forward primer | Reverse Primer |
|---|---|---|
| *hes5* | gaaagccagtggtggaaaag | gaaagccagtggtggaaaag |
| *neurod* | tccgtacggtacaatggaca | taaggggtccgtcaaatgag |
| *her4* | cctggagatgacgcttgatt | cactgggcactgagacagaa |
| *heyl* | gcgatacctcagctctttgg | ggagaggatccagctcactg |
| *deltaC* | gcgactgccagatctttttc | gaaagccagtggtggaaaag |
| *b-actin1* | tgaatcccaaagccaacagagaga | tcacgaccagctagatccagacg |

**Supplemental Figure 1. *Gmds* mRNA localization by *in situ* hybridization in wild type zebrafish embryos from 12 to 72 hpf.**

*In situ* hybridization was performed as described previously (Panzer et al., 2005), with anti-sense (A – E) *gmds* probe; sense probe was used as a control (F). Several hundred embryos from several carrier pairs were used from 6 – 72 hpf.

**A.** From 6 to 12 hpf, *gmds* transcripts are expressed throughout the embryo.

**B.** By 24 hpf, *gmds* transcripts are highly expressed in the CNS and are also expressed in somites at lower levels.

**C, D.** *Gmds* mRNA expression is present in the CNS at 48 (C) and 72 (D) hpf, with transcripts more abundant in brain than spinal cord.

**Supplemental Figure 1. *Gmds* mRNA localization by *in situ* hybridization in wild type zebrafish embryos from 12 to 72 hpf.**

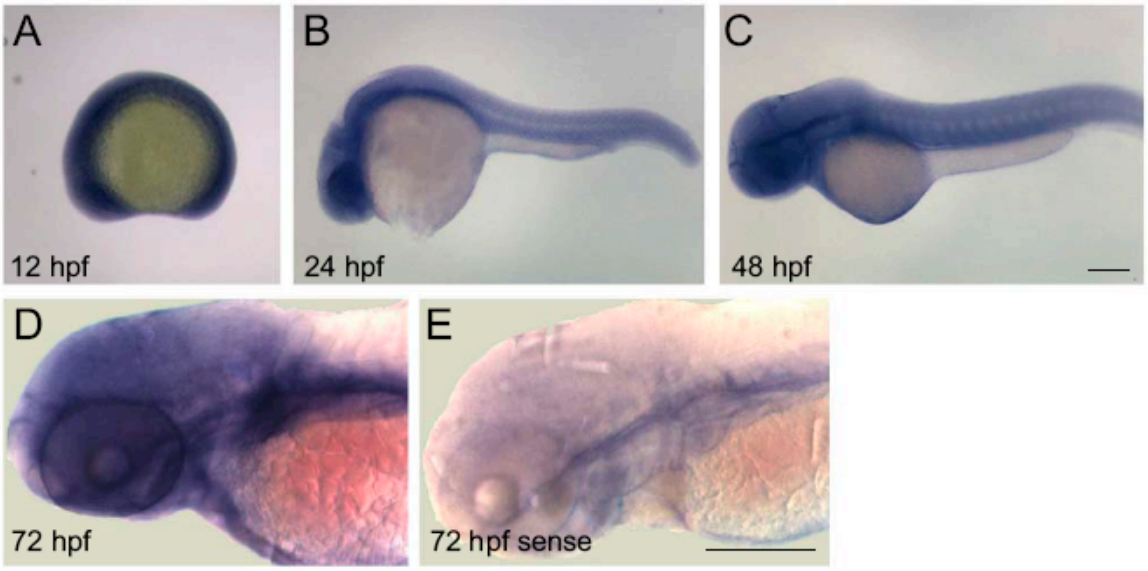

**Supplemental Figure 2. Modeling of zebrafish GMDS protein structure.**

The wild type (brown rods) and *srn* (blue rods) primary amino acid sequence was modeled onto the human GMDS protein crystal structure.

**A:** As in the *srn* mutation, Valine was substituted for Glycine at residue 178 and an energy minimization calculation was performed. When the *srn* mutation is present, the Valine deforms a nearby Glutamate residue, Glu155. This change is predicted to push away the substrate GDP-manose, resulting in loss of function.

**B:** To understand how the movement of Glu155 could affect surrounding amino acids, the wild type structure (brown sticks) was examined in more detail. Three ordered $H_2O$ molecules exist between the negatively charged group on Glu155 and the negatively charged phosphate group on GDP. The bond lengths between water oxygens and phosphate or carboxylic acid oxygens are appropriate to form hydrogen bonds to coordinate GDP to Glu155.

**Supplemental Figure 2. Modeling of zebrafish GMDS protein structure.**

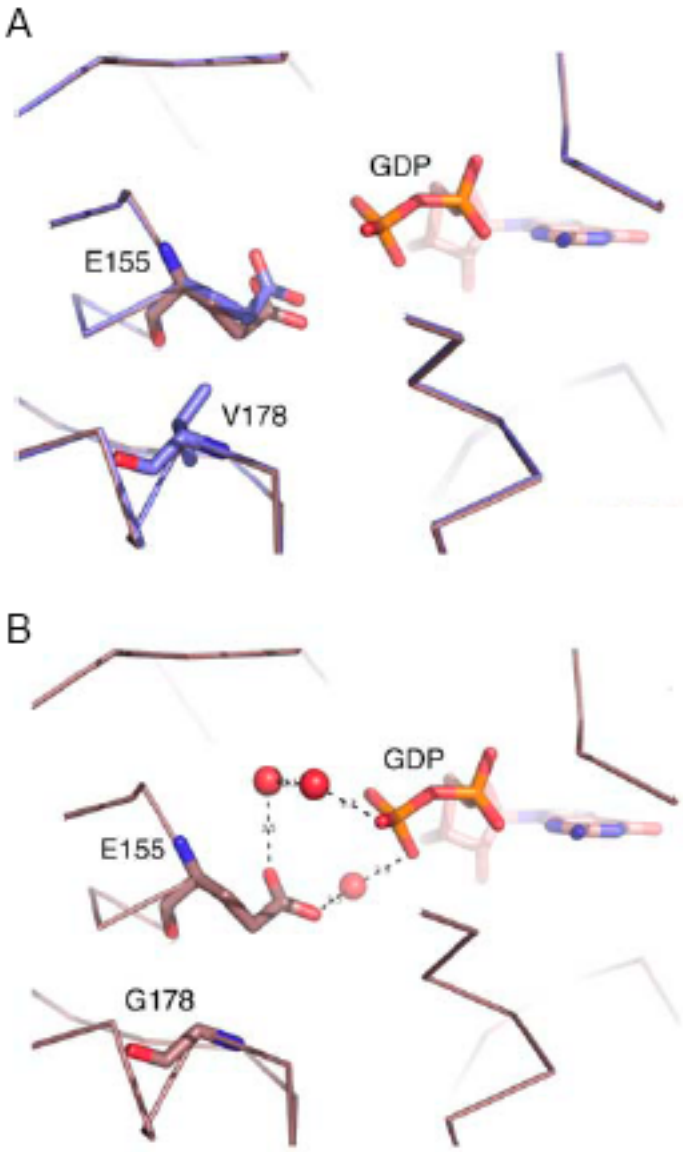

**Supplemental Figure 3. GDP-fucose rescue of *srn* and morpholino knockdown of *gmds*.**

**A.** RT-PCR showed >80% of *gmds* transcript was mis-spliced after *gmds* morpholino (4 ng) injection.

**B-E.** External phenotypes in *srn* and *gmds* morphants (E) include tail bend (compare B, wild type with C, *srn*) which is rescued after GDP-fucose supplementation (D).

**F-I.** *srn* (G) and *gmds* morphants (I) showed reduced AAL staining compared to wild type (F) which is rescued after GDP-fucose supplementation (H).

**J-M.** *srn* (K) and *gmds* morphants (M) showed increased Mauthner neuron number compared to wild type (J) a phenotype that is rescued after GDP-fucose supplementation (L).

**N-Q.** *srn* (O) and *gmds* morphants (Q) showed reduced GFAP+ glia in the spinal cord compared to wild type (N), a phenotype that is rescued after GDP-fucose supplementation (P).

**R-U.** *srn* (S) and *gmds* morphants (U) showed increased neuromuscular synapses compared to wild type (R), a phenotype that is rescued after GDP-fucose supplementation (T). Scale bar = 40 μm.

In each experiment, at least 10 *srn*, normal siblings, *gmds* morphants or GDP-fucose rescued *srn* mutant embryos were assessed at 48 hpf. These results show that

GDP-fucose rescues external and neural defects in *srn* mutants and that *gmds* knockdown by morpholino phenocopies *srn* phenotypes. Together, these further support the conclusions that *gmds* is the gene mutated in *srn,* that the fucose metabolism pathway is deficient in *srn* mutants, and that the resulting lack GDP-fucose is the cause of the *srn* mutant phenotypes, rather than the accumulation of the substrate, GDP-mannose.

**Supplemental Figure 3. GDP-fucose rescue of *srn* and morpholino knockdown of *gmds*.**

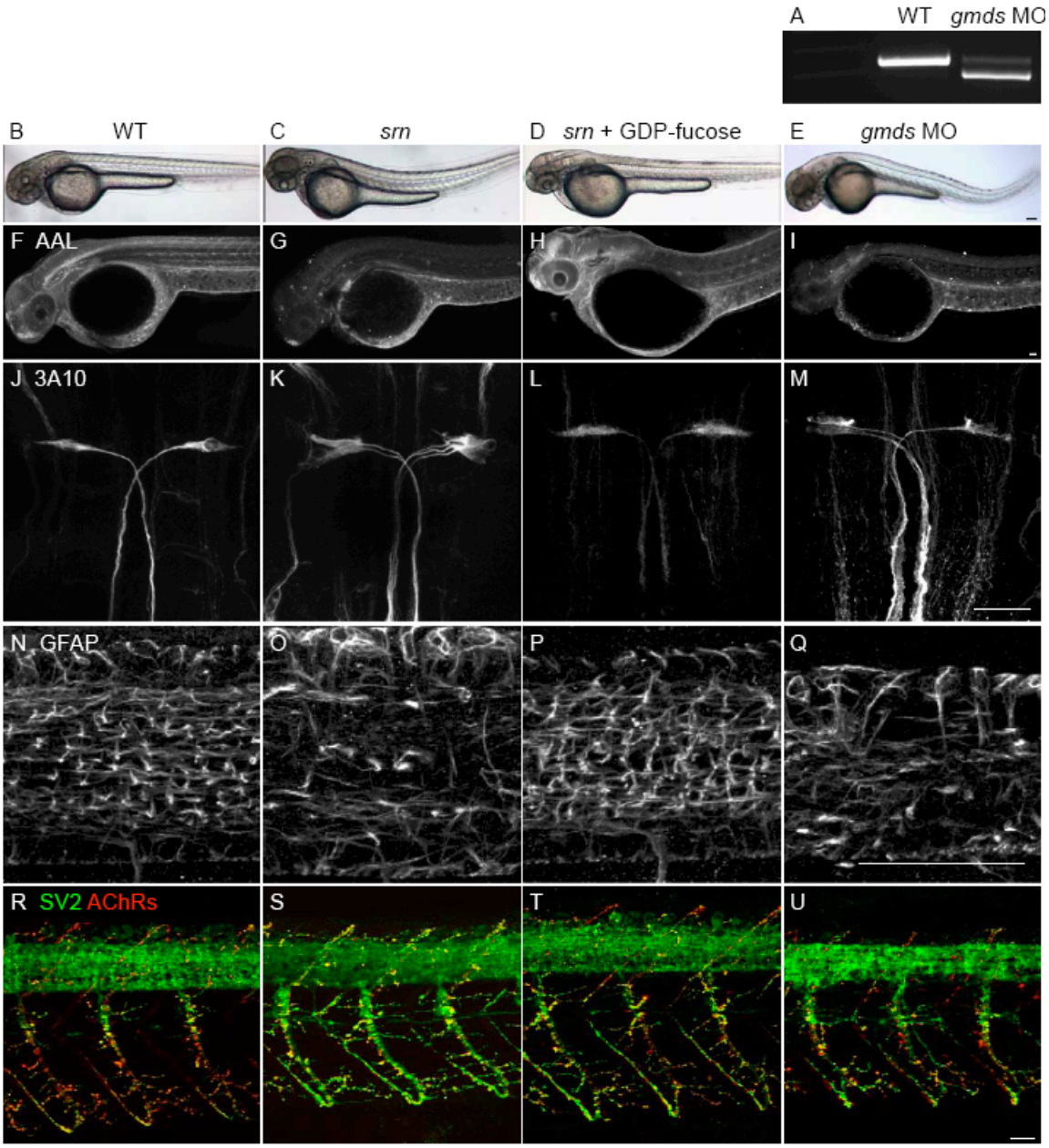

**Supplemental Figure 4. Secondary motor neuron number is reduced in *mib* but not *srn*, *des* or *dla* compared to wild type embryos.**

The number of secondary motor neurons was counted from embryos at 48 and 72 hpf after immunostaining with Zn-5 antibody and confocal reconstruction of the motor neuron pool. At 48 hpf, secondary motor neuron number per hemisegment was similar among wild type (46 ± 2), *srn* (49 ± 1), *des* (52 ± 2) and *dla* (46 ± 2) embryos, and is significantly reduced in *mib* mutant embryos (27 ± 2) (N = 1 hemisegments in each of 6-9 48 hpf embryos counted of each genotype; one-way ANOVA, Bonferroni's Multiple Comparison Test, only *mib* is significantly different compared to other mutants and wild type, $p < 0.001$). At 72 hpf, secondary motor neuron number per hemisegment was similar among wild type (63 ± 2), *srn* (62 ± 1), *des* (63 ± 2) and *dla* (61 ± 2) embryos, and is significantly reduced in *mib* mutant embryos (36 ± 2) (N = 1hemisegments in each of 6-10 72 hpf embryos counted of each genotype; one-way ANOVA, Bonferroni's Multiple Comparison Test; only *mib* is significantly different compared to other mutants and wild type, * $p < 0.001$).

**Supplemental Figure 4. Secondary motor neuron number is reduced in *mib* but not *srn*, *des* or *dla* compared to wild type embryos.**

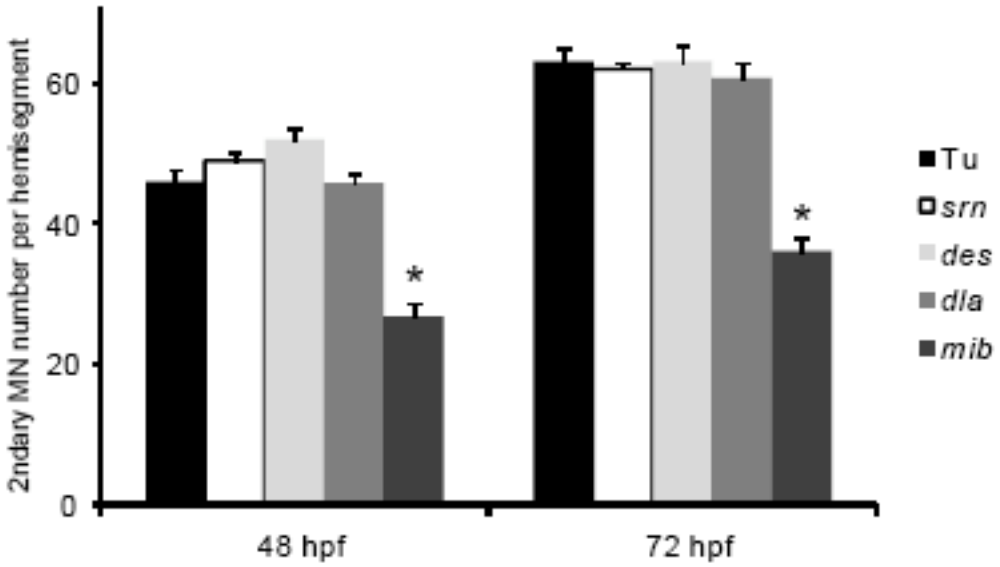

**Supplemental Figure 5. Reduction in Notch-Delta signaling accounts for some *srn* phenotypes in the retina.**

A. Retina patterning was examined with immunostaining using antibody Zn5 at 72 hpf. Retina cell patterning appears grossly normal in *srn*, *des*, *dla* and medium dose DAPT treated embryos, but in *mib* and high does DAPT treated embryos retinal ganglion cell number is reduced, probably due to increased cell death, as previously reported (Bernardos et al., 2005). 8 embryos / 2 carrier pairs were examined. Scale bar = 40 μm.

**B.** Glial cells in the retina were examined after immunostaining with anti-GFAP antibody. In the retina, the number of radially oriented GFAP+ Muller cells is decreased in *srn* and *mib* and medium dose DAPT treated embryos, but not in *des* or *dla*. 8 embryos / 2 carrier pairs were examined. Scale bar = 40 μm.

These results suggest that a reduction in Notch-Delta signaling may account for the glial defects observed in *srn* mutants.

**Supplemental Figure 5. Reduction in Notch-Delta signaling accounts for some *srn* phenotypes in the retina.**

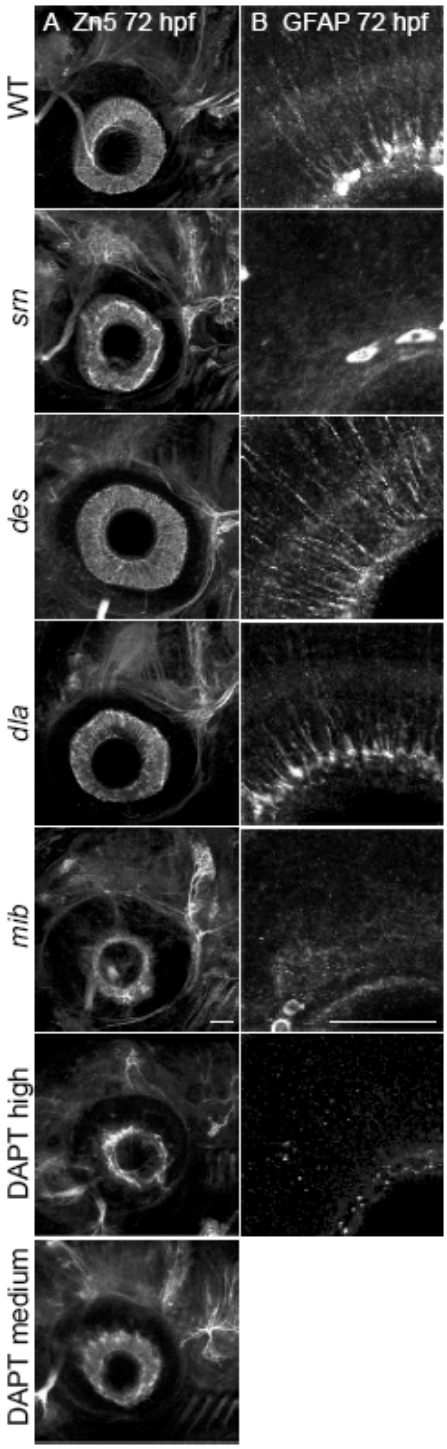

**Supplemental Figure 6. Muscle patterning is grossly normal in *srn* mutants.**

Slow muscle fibers were examined with F59 antibody and glia cells in the spinal cord were examined with GFAP antibody. While there is an obvious reduction of GFAP+ glia cells in the spinal cord in *srn* mutants, the patterning of slow muscle fibers is similar in *srn* and wild type embryos at 48 hpf. Previous work showed that fast muscle fiber number and patterning are unaltered in *srn* compared to wild type embryos at 48 hpf (Panzer et al., 2005). 3 embryos / 1 carrier pair were examined. Scale bar = 200 mm.

**Supplemental Figure 6. Muscle patterning is grossly normal in *srn* mutants.**

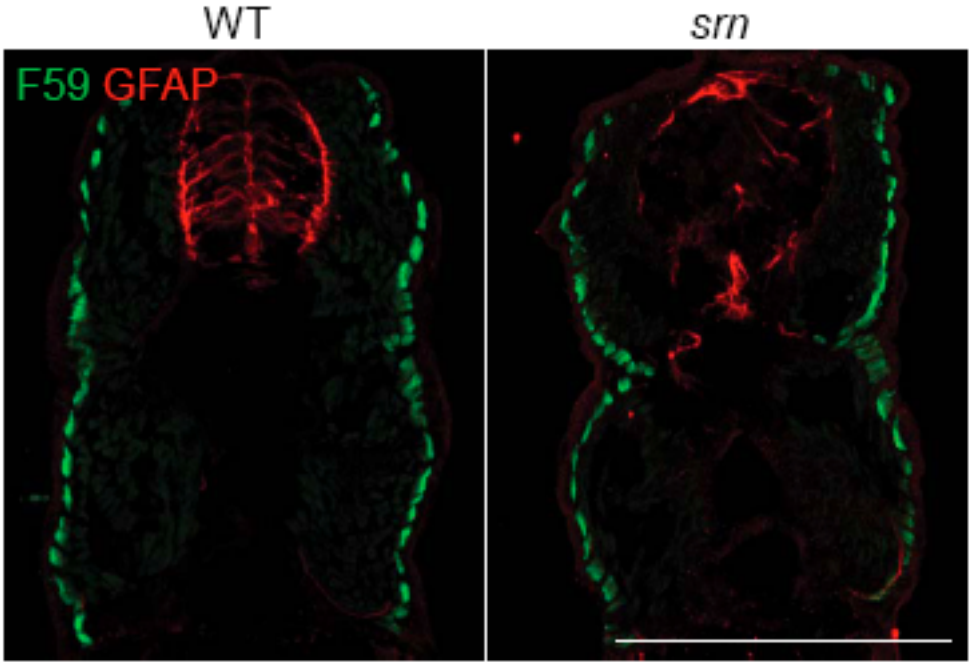

# Chapter 4

## Mutations in electron transfer flavoprotein (ETF) and electron transfer flavoprotein dehydrogenase (ETFDH), cause fatty acid metabolism and mitochondrial dysfunction, unbalanced oxidative phosphorylation and glycolysis, and lead to severe neural defects in zebrafish and humans

In preparation

# Mutations in electron transfer flavoprotein (ETF) and electron transfer flavoprotein dehydrogenase (ETFDH), cause fatty acid metabolism and mitochondrial dysfunction, unbalanced oxidative phosphorylation and glycolysis, and lead to severe neural defects in zebrafish and humans

Y. Song[1], M. A. Selak[2], C. T. Watson[3], C. Coutts[4], P. C. Scherer[1], J. A. Panzer[1], S. Gibbs[1], Marion O. Scott[1], G. Willer[3], R. G. Gregg[3], D. Ali[4], M. J. Bennett[5] and R. J. Balice-Gordon[1]

[1]Dept. of Neuroscience, Univ. of Pennsylvania Sch. Medicine, Philadelphia, PA; [2]Dept. of Pediatrics, Children's Hospital of Philadelphia; [3]Dept. of Biochemistry and Mol. Biology, Univ. of Louisville, Louisville, KY; [4]Dept. of Biological Sciences, Univ. of Alberta, Edmonton, Alberta, CA; [5]Dept. of Pathology & Laboratory Medicine, Children's Hospital of Philadelphia.

**Running title:** Metabolic and neural phenotypes in zebrafish and human MADD

**Figures / Tables / Supplemental Figs., Tables:** 6 / 0 / 9, 2

**Key words:** MADD, glutaric aciduria II, mitochondria, fatty acid β-oxidation, PPARG, aerobic glycolysis, neurogenesis, glia, synaptogenesis

**Address correspondence to:**

Rita Balice-Gordon, Ph.D., Dept. of Neuroscience, University of Pennsylvania School of Medicine, 215 Stemmler Hall, Philadelphia, PA 19104-6074. (215) 898-1037 Fax: (215) 573-9122 Email: rbaliceg@mail.med.upenn.edu

**Summary**

In humans, mutations in electron transfer flavoprotein (ETF) or electron transfer flavoprotein dehydrogenase (ETFDH) lead to multiple acyl-CoA dehydrogenase deficiency (MADD) / glutaric aciduria II, an autosomal recessively inherited disorder characterized by a broad spectrum of devastating neurological and other symptoms. We show that a zebrafish mutant in ETFDH, *xavier*, and fibroblast cells from MADD patients, have similar metabolic defects and mitochondrial dysfunction, in particular excessive aerobic glycolysis, and upregulation of the PPARG-ERK pathway. This metabolic dysfunction leads to aberrant neural proliferation in *xav*, in addition to other neural phenotypes and paralysis. Strikingly, a PPARG antagonist attenuates aberrant neural proliferation and alleviates paralysis in *xav*, while PPARG agonists increase neural proliferation in wild type embryos. These results provide new insights into the mechanisms coupling metabolism and neural development, showing for the first time that mitochondrial dysfunction leading to an increase in aerobic glycolysis affects neurogenesis through the PPARG-ERK pathway. Using *xav* as the first animal model for MADD, we now have a better understanding of the mechanisms underlying this rare but devastating human disorder, and have identified the PPARG-ERK pathway as a potential target for therapeutic intervention.

## Introduction

Mitochondria, the cellular power plants in most eukaryotic organisms, play pivotal roles in cell signaling, differentiation, and the control of cell cycle, growth and death. Particularly in the nervous system, mitochondrial function is essential in meeting the high energy demand in neurons and glia (reviewed in Knott et al., 2008; Mattson et al., 2008). During nervous system development, mitochondria regulate neural proliferation and differentiation by supporting the different bioenergetic requirements of highly proliferative neural stem cells compared to postmitotic neurons (Erecinska et al., 2004). Mitochondrial dysfunction has been implicated in various aspects of neuronal and glial dysfunction, aging, as well as in the pathogenesis of neurodegenerative diseases (reviewed in Knott et al., 2008; Mattson et al., 2008; Wallace, 2005). However, when mitochondria cause and compensate for physiological and pathological challenges, how this in turn affects neurogenesis, neural development, and nervous system function, remain poorly understood.

Multiple acyl-CoA dehydrogenase deficiency (MADD), also known as glutaric aciduria type II, is an autosomal-recessive inherited disorder caused by mutations in electron transfer flavoprotein (ETF) or electron transfer flavoprotein dehydrogenase (ETFDH) (Frerman and Goodman, 2001). In mitochondria, ETF, located in the matrix, receives electrons from several dehydrogenases involved in fatty acid oxidation and amino acid metabolism. ETF then transfers electrons to ETFDH, located in the inner mitochondrial membrane, and subsequently, electrons are passed to ubiquinone in the respiratory chain, leading to ATP production (McKean et al., 1983; Ruzicka and Beinert,

1977). As a result of ETF or ETFDH deficiency, the acyl-CoA dehydrogenases are unable to transfer the electrons generated by dehydrogenation reactions, resulting in the accumulation of various acyl-esters in blood and urine, giving the disease its name (Frerman and Goodman, 2001).

The clinical features of MADD are highly heterogeneous and have been classified as neonatal-onset form with (type I) or without (type II) congenital anomalies, and mild and/or late-onset form (type III). MADD consists of a large spectrum of symptoms, including hypotonia, hypoglycemia, cardiomyopathy, polycystic kidneys, and neurological manifestations such as symmetric warty dysplasia of the cerebral cortex, encephalopathy and leukodystrophy. While there have been case studies reporting the use of riboflavin (reviewed in Rinaldo et al., 2002) and sodium-3-hydroxybutyrate (Bonham et al., 1999; Van Hove et al., 2003) as treatment for MADD on a patient-by-patient basis, no systematic therapy has been validated. Moreover, despite the neurodevelopmental and cognitive dysfunction prominent in MADD patients, the anatomical, cellular and molecular abnormalities within the nervous system have not been well documented, and the mechanisms underlying neural phenotypes remain unexplored.

Here we report the genetic, cellular and molecular characterization of a zebrafish mutant *xav*. We had previously identified *xav* as a mutant that exhibits abnormal motility and aberrant neuromuscular synaptogenesis (Panzer et al., 2005). We found that the *xav* mutation resides in ETFDH, which is critical for fatty acid and choline metabolism. Because dysfunction of this gene is responsible for human MADD, we performed several

cellular and molecular analyses on *xav* mutants and fibroblast cells from MADD patients. Our results advance our understanding of how metabolism affects neural development, link mitochondrial dysfunction and the resulting increase in aerobic glycolysis to neurogenesis via the PPARG-ERK pathway, and suggest this pathway as a target for therapeutic intervention in human MADD.

## Experimental Procedures

### Zebrafish husbandry

Zebrafish were raised and maintained under standard conditions. The *xav* allele was previously described (Panzer et al., 2005). Wild type and mutant embryos were obtained from crosses between adult zebrafish.

### Fibroblasts from human MADD patients

Fibroblasts from a MADD patient, WH, were obtained from Dr. William J. Rhead, Department of Pediatrics, Children's Hospital of Wisconsin. Fibroblasts from an age-matched control patient (an infant, < 1 year of age, with no evident related disease) were obtained from Dr. Carsten Bonnemann, Children's Hospital of Philadelphia. Patient WH is a deceased newborn with severe MADD, whose acylcarnitine profile showed elevations of C5- and C16- intermediates, and extremely low C2-carnitines (Dr. Rhead, personal communication). We found that patient WH showed mis-splicing of *ETFA* transcript, lacking the long isoform that contains exon2. Gene sequencing showed that patient WH has a 52 C>T heterozygous mutation in exon2 that may cause the splicing defects. The same mutation has been reported in a MADD patient with neonatal neurological deterioration and metabolic acidosis (Schiff et al., 2006).

Fibroblasts from passages 6 – 12 were grown to 80-100% confluency and used for metabolic or gene expression analyses as indicated.

**Positional cloning of *xav***

Adult zebrafish heterozygous for the *xav* mutation were crossed to generate a panel for linkage mapping. DNA was isolated from *xav* homozygous mutant embryos, wild type siblings, and parental fin clips. Bulk segregant analysis was performed as described (Willer et al., 2005), using microsatellite markers (Knapik et al., 1998; Shimoda et al., 1999) (http://zebrafish.mgh.harvard.edu/zebrafish/index.htm). Once linkage was detected, 96 mutant individuals were genotyped to localize the mutation between two closely flanking markers. These analyses mapped *xav* to chromosome 14 between markers Z15804 and Z7108. An additional 749 *xav* mutant embryos were collected from two mapping crosses and used for further linkage analysis. New simple sequence repeat (SSR) markers were identified from sequenced BAC clones and primers were designed using the zebrafish SSR search web site (http://danio.mgh.harvard.edu/markers/ssr.html). Primer sequences for new markers are given in Supplemental Table 1. PCR reactions were run with 5 PRIME Taq DNA polymerase according to the manufacturer's instructions. Genotypes were determined by analyses of PCR products on 4% agarose E-Gels (Invitrogen). For genotyping large numbers of fish we used fluorescently labeled primers and analyzed products on ABI 3130xl Genetic Analyzer (Applied Biosystems).

To sequence the open reading frame (ORF) of candidate genes, RNA was isolated from pools of mutant and WT embryos using a VERSAGENE RNA isolation Tissue Kit (Gentra Systems). cDNA was synthesized using Oligo (dT) and Superscript III as

described by the manufacturer (Invitrogen). cDNA fragments of the entire ORF were obtained by PCR using Accuprime Taq polymerase and Buffer II (Invitrogen), 20mM of each primer (Sup. Table 1) and first strand cDNA. Amplified products were purified and sequenced using the ABI Big dye terminators and an ABI 3130xl Genetic Analyzer. When necessary, PCR products were cloned into pCR 4-TOPO (Invitrogen), plasmid DNA isolated with Wizard Plus SV Minipreps (Promega) and inserts sequenced as described above.

**Morpholino injection**

The morpholino antisense oligonucleotide (Gene Tools) targeting the *etfdh* intron2-exon3 junction (CTACCCCTGAAAACATTCAATTATA) was injected at the 1-2 cell stage at ~8 ng.

**Plasma acylcarnitine and organic acid profiling**

Sonicated fish (N = 40-80) were subjected to acylcarnitine and organic acid analysis. Acylcarnitines were analyzed by tandem mass spectrometry as butyl esters using the procedure initially developed for skin fibroblast acylcarnitine analysis (Shen et al., 2000). Organic acids were analyzed as their trimethylsilyl derivatives by capillary gas chromatography- electron impact mass spectrometry using a procedure that was initially developed for urine and vitreous humour analysis (Bennett et al., 1992).

**RNA extraction and quantitative RT-PCR (qRT-PCR)**

RNA was extracted from a pool of 20 embryos with the RNeasy kit (Qiagen). The primers for qRT-PCR are shown in Supplemental Table 2. qRT-PCR was performed with the SuperScript® III Platinum® SYBR® Green One-Step qPCR Kit w/ROX (Invitrogen) and data was analyzed with 7500 Real-Time PCR System software (Applied Biosystems) using the $2^{-\Delta CT}$ method, data were normalized to *β-actin1* for zebrafish and *ACTB* for fibroblasts.

**BrdU labeling and immunostaining**

BrdU labeling was performed as described previously (Zannino and Appel, 2009). In brief, at ~56-60 hpf, embryos were incubated with 10 mM BrdU in 10% DMSO in embryo medium for 30 min. on ice and then raised in embryo medium at 28.5°C for 30 min. The embryos were then fixed using 4% paraformaldehyde in PBS, pH = 7.4, followed by 2 hour incubation in 2 M HCl. Embryos were anesthetized, fixed and immunostained as described previously (Panzer et al., 2005) using antibodies against BrdU (mouse monoclonal Developmental Studies Hydrodermal Bank (DSHB); rabbit polyclonal, Abcam) and dp-ERK (Sigma) and the appropriate fluorescently conjugated secondary antibody (Jackson Labs). Unless otherwise stated, each figure panel showing immunostaining is a single plane projection of a confocal z-stack of 20-60 1 μm thick planes (Leica TCS 4D system) and was assessed using interactive software (Metamorph).

**Western blotting**

To prepare protein, embryos were triturated in lysis buffer (100mM pH 8 Tris, 1% SDS, 10mM EDTA, 50 mM DTT). Protein quantity was assessed ($D_c$ Protein Assay; Bio-Rad) and proteins were separated by SDS-PAGE (4-10% gradient gel), transferred to a nitrocellulose membrane and probed with antibodies against AMPKα (Cell Signaling), phospho-AMPKα (Thr172) (Cell Signaling), PPARG (Santa Cruz), dp-ERK (Sigma), phospho-STAT3 (Tyr705) (MBL) and/or actin (Sigma). After washing, blots were incubated in AP-conjugated secondary antibody (Jackson Labs), and then visualized using chemiluminescence (Western*Star* detection system; Applied Biosystems).

**ROS labeling**

Embryos were incubated in embryo medium containing 10 μM of dyhydrorhodamine123 (DHR123, Invitrogen) for 2 hrs at 28°C, then washed with embryo medium several times and examined with confocal microscopy.

**Polarographic analysis of oxygen consumption, mitochondrial membrane potential measurement,ATP and lactate quantification**

WT and xav embryos (50-100 embryos for each sample) were homogenized in a mitochondrial isolation buffer (MIB) (in mM, 210 mannitol, 70 sucrose, 10 HEPES (pH

7.2), 0.2 EGTA) freshly supplemented with 0.5% fatty acid- free BSA and 1/100 dilution of Sigma protease inhibitor cocktail. All operations and buffers were at 2-4$^{o}$C.

Oxygen consumption was measured polarographically using a Strathkelvin oxygen electrode at 28°C. Homogenates were suspended in a total volume of 0.15 mL of air-saturated buffer composed (in mM) of 220 mannitol, 70 sucrose, 5 HEPES, pH 7.2, 5 KH2PO4, 0.2 EGTA and 5 EDTA. Oxidation of carnitine esters was measured in the presence of 2 mM malate with either 0.10 mM palmitoylcarnitine or 0.2 mM octoylcarnitine followed by addition of 0.2 mM ADP. Oxygen consumption was also measured in the presence of 10 mM α-ketoglutarate + 2 mM malate or 10 mM succinate + 2 μM rotenone. Azide-sensitive cytochrome oxidase activity (complex IV) was measured in the presence of 2.5 mM ascorbate + 0,25 mM N,N,N′,N′-tetramethyl-p -phenylenediamine (TMPD). Rates of substrate oxidation with or without ADP were expressed as nanoatoms of oxygen consumed per minute per milligram homogenate protein. State 3 refers to oxygen consumption stimulated by a limiting amount of ADP and state 4 refers to oxygen consumption after phosphorylation of the added ADP to ATP.

Tetra-methyl rhodamine ester (TMRE, Invitrogen) was used to measure generation of mitochondrial transmembrane potential. Used in the quench mode, energization of mitochondria decreases and uncoupling increases TMRE fluorescence measured using excitation/emission wavelengths of 549 nm and 574 nm, respectively, in an Aminco-Bowman Series 2 spectrofluorometer. Homogenates were suspended in buffer composed (in mM) of 220 mannitol, 70 sucrose, 10 Hepes, pH 7.2, 5 KH2PO4, 0.2

EGTA and 200 nM TMRE. Fluorescence changes were monitored continuously while the sample was magnetically stirred at ambient temperature. Energization was achieved by addition of 2 mM malate with 0.40 mM palmitoylcarnitine or 0.2 mM octoylcarnitine, or 10 mM α-ketoglutamate + 2 mM malate; mitochondria were depolarized by addition of 5 μM ClCCP.

Measurement of intact cellular respiration was performed using the Seahorse XF24 analyser (Ferrick et al., 2008). Respiration was measured under basal condition, in the presence of the mitochondrial inhibitor oligomycin (0.5 μg/ml), in the presence of the mitochondrial uncoupler carbonyl cyanide *m*-chlorophenylhydrazone (CICCP) (3 μM) and in the presence of complex I inhibitor rotenone (100 nM) to assess maximal oxidative capacity as described previously.

For ATP quantification, fibroblasts or embryo homogenate were prepared in MIB. While continuously vortexing, 0.1 volume of 6N PCA was added to homogenates while vortexing to achieve a final concentration of 0.6 N PCA. Following a 15 min incubation on ice to facilitate full precipitation, samples were centrifuged at 15,000 g for 15 min. Extracts were transferred to a clean tube and sufficient 2M KHCO3 was added while vortexing to achieve a final concentration of 0.5M KHCO3. Extracts were centrifuged at 15,000 g for 15 min, transferred to a clean tube and frozen at -80°C until assayed using a ATP luminescence kit (Sigma). Luminescence was read using a Turner luminometer. Protein concentration was quantified using the BCA assay (Pierce) with BSA as a standard. For lactate measurement in fibroblasts, culture media was collected after 6 days *in vitro* and assayed with Lactate Assay Kit (Biovision) and a fluorometer. For lactate

measurement in embryos, embryos were prepared as for ATP measurement, and were assayed using Lactate Assay Kit (Biovision) with a spectrometer.

**PPARG pharmacology**

Embryos were incubated in 25 μ m PPARG antagonist BADGE (Wada et al., 2006) or agonist 10 μM Ciglitizone (Nam et al., 2007) at ~24 hpf until the desired developmental stage.

**Acknowledgements**

We thank Dr. William J. Rhead for providing MADD patient fibroblasts, Dr. Carsten Bonnemann for providing control patient fibroblasts, Drs. Marnie Halpern and Bill Saxton for providing the mito-GFP construct, Drs. Michael Granato and Dirk Meyer for providing the *hb9* construct, Drs. S. Nona and J. Scholes for providing the anti-GFAP antibody, Dr. Ethan Hughes for assisting with quantification of neuromuscular synapses, Dr. Ang Li for assistance with qRT-PCR analyses, Dr. Kevin Bittman for assistance with the analyses using the XF24 instrumentation, Ms. Amy Kugath for technical assistance, in particular with zebrafish husbandry, and members of the Balice-Gordon lab for helpful discussions. Supported by NIH grant NS050524 to R. B.-G.

## Results

### *External phenotypes, genetic cloning and morpholino phenocopy of xav*

We previously identified *xav* in a small scale genetic screen due to its abnormal swimming behavior and decreased number of neuromuscular synapses (Panzer et al., 2005). Externally, *xav* mutants cannot be distinguished from WT until after 48 hpf, when they start to exhibit a bent tail and slower heart beat, a phenotype that becomes progressively more severe (Fig. 1A, 1B).

Positional cloning strategies were used to identify the mutation responsible for the *xav* phenotype. Bulk segregant analysis initially localized the mutation to chromosome 14 between Z15804 and Z7108 on linkage group 14. Further mapping using newly designed SSR markers localized the mutation between 274P15-SSR1 and 199B20-SSR1 (Fig. 1C). Sequence from the Ensembl Zv6 genome build did not appear to be correctly ordered between the flanking markers as was evidenced by the fact that our linkage data indicated markers 36H4-SSR1 (Fig. 1B) and Z4701 (data not shown) fell outside the interval while the Zv6 build placed these sequences directly between the flanking markers (data not shown). For this reason, we asked if the general order of some of the genes in the region could be confirmed based on conserved synteny with human. We found that *LOC557693*, *tmem33*, *zgc:92093*, and *ppid* potentially represented a conserved block of genes (Sup. Fig. 1). SSR markers were then designed in BAC clones that contained these genes to determine if the sequences were truly positioned within the interval. Following this strategy, marker 278P11-SSR1 was found to have zero recombinants. Interestingly, the linkage results also indicated that BAC DKEY-50I13,

positioned roughly 50 Mb from this region on the Zv6 build, was in fact located in the critical interval (Fig. 1C). The open reading frames for the three genes in BAC CH211-278P11 (*LOC565292= rxfp1-like*, *zgc:92093*, and *ppid*) were amplified from mutant and wild-type embryos and sequenced to look for mutations. *zgc:92093* was found to contain a T to A transversion at position 1305 which introduces a premature stop codon (Y435X) in the 617 amino acid protein (Fig. 1D, 1E). *zgc:92093* encodes electron-transfer-flavoprotein dehydrogenase (etfdh) which is highly conserved among species and is 80% homologous to its human counterpart.

Besides the truncation of the protein caused by the *xav etfdh* mutation, we also found that the overall abundance of *etfdh* mRNA in *xav* is dramatically reduced. Real-time quantitative RT-PCR (qRT-PCR) showed that there is 80% reduction of *etfdh* mRNA (Sup. Fig. 2A), likely due to nonsense mediated decay (Hentze and Kulozik, 1999). Furthermore, *xav* mutants showed nonsense mediated alternative splicing. As a result of the mutation, which resides in exon11, the exon10-exon13 junctions are mis-spliced in mutants, resulting in transcripts that are predicted to encode proteins lacking critical domains or truncated (Sup. Fig. 2B). These results suggest that *xav* contains a likely loss of function mutation in *etfdh*.

To confirm whether *etfdh* is the gene mutated in *xav*, we designed a splice-blocking morpholino against *etfdh* and compared the phenotypes in morphants and mutants. Injection of 8 ng *etfdh* MOI2E3 in WT embryos, which targets intron2-exon 3 junction, results in > 80% reduction of the normal transcript at 2 and 3 dpf, producing a mis-spliced transcript that lacks exon3 (Sup. Fig. 3C, 3D), resulting in predicted protein

fragment lacking all functional domains (Fig. 1E). *etfdh* morphants not only showed bent tail and reduced heart beat (Fig. 1A, 1B), but also exhibited aberrant swimming behavior and reduced neuromuscular synaptogenesis (see Supplemental Results and Sup. Fig 6 and data not shown), as in *xav* mutants. These results indicate that *etfdh* mutation is responsible for *xav* phenotypes.

***xav mutants exhibit plasma acylcarnitine and organic acid profiles similar to those in MADD patients***

Given the fact that *xav* and MADD patients have mutation in the same gene, we asked whether *xav* mutants exhibit phenotypes similar to those seen in human patients. Clinically, MADD is diagnosed by the plasma acylcarnitine profile, the urine organic acid profile and acylglycine analysis. These analyses were thus performed in *xav* mutants compared to WT embryos.

Tandem mass spectroscopy of plasma acylcarnitine detected a markedly higher level of a spectrum of intermediate acyl-fatty acid species in *xav* mutants, including C4, C5, C6, C8, C14, C16 and C18, together with a drastic reduction of C2 acylcarnitine (Fig. 2A), suggesting dysregulation of mitochondrial β-oxidation and alterations in multiple intermediary mitochondrial metabolic pathways in *xav*, similar to that observed in MADD patients (Frerman and Goodman, 2001).

Gas chromatographic analysis of organic acids from embryo homogenates detected a dramatic elevation of glutaric acid in *xav* (Fig. 2B). Further quantification

showed the glutaric acid content in *xav* is 0.99 μg/embryo, but < 0.05 μg/embryo in WT, resembling the glutaric acidemia seen in MADD patients (Frerman and Goodman, 2001).

While acylglycine analysis showed elevated acylglycine levels in MADD patients, no acylglycine was detected in either WT or *xav* embryos. This suggests that the function of glycine-N-acyltransferase, which converts acyl-CoA and glycine to CoA and acylglycine, may not be conserved between zebrafish and humans. Moreover, kidney defects were observed at the organ structural and cellular level in *xav* mutants compared to WT embryos at ~60 hpf (Sup. Fig. 3), consistent with a polycystic kidney phenotype that is prominent in MADD patients. Together, these analyses show that the *etfdh* mutation in *xav* results in MADD like metabolic and kidney defects.

***xav mutants exhibit several hallmarks of mitochondrial dysfunction***

Given the fact that *etfdh* functions in mitochondria, and is involved in fatty acid metabolism and electron transport, we asked whether mitochondria function is abnormal in *xav* mutants. First, we evaluated the efficiency of oxidative phosphorylation in homogenates of *xav* mutants and WT embryos at ~56 hpf, by measuring $O_2$ consumption after stimulation with α-ketoglutarate and fatty acids as substrates. Rates of $O_2$ consumption were decreased ~30-35% in *xav* mitochondria with either substrate (Fig. 3A; Sup. Fig. 4A). Maximal rates of state 3 respiration, stimulated by the addition of ADP, were blunted in *xav* mitochondria (Sup. Fig. 4A). These suggest that oxidative phosphorylation is compromised in *xav*.

Mitochondria maintain a membrane potential, which is usually generated by respiratory chain complexes, and is utilized to drive critical cellular processes, such as the production of ATP and $Ca^{2+}$ uptake. We measured mitochondrial membrane potential using tetramethylrhodamine ethyl ester (TMRE) as an indicator in *xav* mutant and WT embryos at ~56 hpf. We found a ~50% reduction of membrane potential stimulated by fatty acids (Fig. 3B), consistent with a decrease of $O_2$ consumption. Surprisingly, however, despite the decrease in $O_2$ consumption stimulated by α-ketoglutarate, mitochondrial membrane potential was observed to be increased by ~50% (Fig. 3B). This result suggests that additional membrane potential is generated in response to defects in the electron transport chain, but is not properly utilized for $O_2$ consumption.

Despite reduced $O_2$ consumption after α-ketoglutarate and fatty acid stimulation, the activity of complex IV was increased by 40% when assayed directly after N,N,N′,N′-tetramethyl-p -phenylenediamine (TMPD)/ascorbate stimulation (Fig. 3C), suggesting a compensatory response that potentiates the remaining respiratory capacity in *xav* mutants. Consistent with this idea, at ~56 hpf, a higher level of F1-F0 ATPase (complex V) protein was detected by immunostaining in *xav* mutants compared to WT (Sup. Fig. 4B). This likely reflects a response to insufficient respiration, and is consistent with compensation.

To further assess mitochondrial defects, we examined the activity of AMP-activated protein kinase (AMPK), which is an evolutionarily conserved metabolic sensor that responds to alterations in cellular energy levels to maintain energy balance. Biochemical analyses showed that while the total level of AMPK is unchanged in *xav*,

the level of activated AMPK (phospho-AMPK$\alpha^{Thr172}$) protein is significantly increased (Fig. 3D, 3E). This result suggests that there is a homeostatic regulation in *xav* mutants, in response to insufficient metabolism. In addition, measurement of ATP production showed a ~45% reduction in *xav* mutant compared to WT embryos (Fig. 3F), despite a compensatory increase of complex IV, complex V and activated, p-AMPK protein levels. Together, these results suggest that the *etfdh* mutation in *xav* results in respiratory chain deficiency, which is not restricted to the fatty acid metabolism pathway. This further leads to dysregulation of mitochondrial membrane potential and insufficient energy production.

In order to gain more insight into the mitochondrial dysfunction in *xav* and the underlying molecular mechanisms, we profiled the expression of genes known to be involved in mitochondrial function and biogenesis with qRT-PCR (Fig. 3G). We found a ~30-40% reduction of *mt-nd5* and *ndufs1*, two mitochondria encoded genes that belong to complex I. Mutations of these genes are associated with complex I deficiency and mitochondrial encephalomyopathy, lactic acidosis, and stroke-like episodes (MELAS), two disorders which have neurological manifestations (Benit et al., 2001; Loeffen et al., 2000; Triepels et al., 2001). The expression of *pgc-1β*, *esrrα* and *pparγ*, genes involved in transcriptional regulation of energy metabolism, were increased ~2.4, 1.5 and 2.8 fold, respectively. Interestingly, expression of zebrafish *uncoupling protein 4* (*fucp4*), which is proposed to be responsible for uncoupling of respiration from ATP synthesis and thus protect against reactive oxygen species (ROS) production, showed a ~6 fold increase, while *ucp2* expression remained unchanged. The closest homologue of *fucp4* in humans, *UCP3*, has been reported to be upregulated in MADD patients (Russell et al., 2003).

These results document mitochondrial dysfunction at the level of alteration of gene expression in *xav* mutants as a result of *etfdh* mutation.

Impairment of mitochondrial metabolism, including β-oxidation, may result in greater oxidative stress (Wallace, 1999), which increases generation of ROS. The oxidative fluorescent dye dihydrorodamine-123 (DHR-123) was used to qualitatively address cellular superoxide production. DHR-123 labeling in live embryos showed higher cellular superoxide levels in *xav* mutants compared to WT, especially in the nervous system, including in the spinal cord (Fig. 3H). We next assessed the expression profile of genes known to be involved in the ROS pathway. qRT-PCR analyses showed a 50% reduction of *catalase* transcripts and 5-fold increase of *glutathione reductase* (Fig. 3I), both of which are known to reduce ROS generation. We also found a 5 fold increase of *hspa9* (Fig. 3I), mutation of which produces an increase in ROS in blood cells (Craven et al., 2004). These results further confirm that *etfdh* mutation results in mitochondrial dysfunction and subsequent oxidative stress in *xav* mutants.

***Human MADD fibroblast cells display similar mitochondrial dysfunction as xav mutants***

We next asked whether the mitochondrial abnormalities observed in *xav* are similar to those in MADD patients. As analyses of MADD patient tissues are rare, and postmortem tissues are not available, we performed analyses on fibroblast cells from a patient, WH, and a control patient.

Fibroblasts from Patient WH exhibited increased mitochondrial oxidative capacity as elicited by the uncoupler carbonyl cyanide *m*-chlorophenylhydrazone (CICCP) compared to control fibroblasts (Fig. 4A), resembling the increased complex IV and complex V activity observed in *xav*. Basal ATP levels were slightly but significantly reduced in Patient WH fibroblasts (Fig. 4B). These results suggest insufficient respiration and compensation in MADD patients as in *xav* mutants. Moreover, while electron transport chain is compromised, cells *in vitro* are more readily able to maintain ATP homeostasis than *in vivo*, either by upregulating reserve respiration capacity, by shifting to glycolysis (as discussed in the following section) or by reducing dependence on fatty acids.

Gene expression profiling revealed that *PGC-1β*, *PPARG*, *ESRRα*, *UCP3* were all significantly increased in Patient WH (Fig. 4C), as in *xav*. Furthermore, the expression of ROS related genes are also altered in Patient WH, as in *xav*, in particular decreased *catalase* and increased *glutathione reductase* and *HSPA9* (Fig. 4C). These results extend our understanding of the extent of mitochondrial dysfunction in human MADD, and show further that this dysfunction is similar at the metabolic and gene expression level in *xav* and MADD patients.

***MADD fibroblasts and xav mutants exhibit increased aerobic glycolysis***

During the course of measuring mitochondrial oxidative responses, we noticed that there was also a significant increase in the extracellular acidification rate (ECAR) in

Patient WH, especially in the presence of an uncoupler (Fig. 5A). ECAR reflects changes in proton concentration and is used as readout of lactate production as this dominates the acidification rate and of levels of glycolysis (Watanabe et al., 2006). While the increase in ECAR in Patient WH fibroblasts suggested that aerobic glycolysis is increased, we performed two additional analyses to further examine this possibility. First, the amount of lactate secreted into the culture medium was directly measured in Patient WH fibroblasts. Basal lactate production was increased by ~25%, consistent with increased glycolysis (Fig. 5B). Second, the expression profile of genes critical for glycolysis or in the glycolytic pathway was assessed using qRT-PCR. mRNA for glycolytic enzymes *enolase 1* (*ENO1*), *phosphoglycerate mutase 1* (*PGAM1*), *phosphoglycerate kinase 1* (*PGK1*) and *phosphofructokinase* (*PFKM*) were all significantly increased in MADD patients (Fig. 5C). These results suggest that aerobic glycolysis is increased in fibroblasts from MADD patients.

To determine whether glycolysis is also elevated in *xav* mutants, the amount of lactate was directly measured and was found to be increased by ~2.4 fold in *xav* mutants compared to WT embryos at ~56 hpf (Fig. 5D). Gene expression analyses by qRT-PCR revealed significant changes in expression of several glycolysis related genes. mRNA for the glycolytic enzymes *eno1*, *pgam1a*, *pgk1* and *pfkma*, as well as *fructose-biphosphate aldolase C* (*aldoc*) was significantly increased (Fig. 5E). mRNA for *dihydrolipoamide S-acetyltransferase* (*dlat*), that belongs to the pyruvate dehydrogenase complex which links glycolysis to tricarboxylic acid (TCA) cycle, was significantly decreased (Fig. 5E). Together, these data suggest that in both human MADD cells and *xav* mutants, there is an electron transport chain deficiency which compromises oxidative phosphorylation,

leading to an upregulation in aerobic glycolysis, likely as an alternative energy source to compensate for this metabolic insuffiency.

***xav mutants exhibit increased neural proliferation***

Many proliferating cells, including some cancer cells, utilize aerobic glycolysis, which while an inefficient way to generate ATP compared to oxidative phosphorylation, has been suggested to have the advantage of generating a number of intermediates which can be used to incorporate nutrients into the cell biomass, a phenomenon known as the Warburg effect (reviewed in Vander Heiden et al., 2009). Because changes in utilization of metabolic pathway from oxidative phosphorylation to aerobic glycolysis affect proliferation, and because of the striking neural phenotypes observed in *xav* mutants, including reduced neuropil staining, abnormal glial patterning, reduced motor axon branching and neuromuscular synaptogenesis, increased cell death and progressive paralysis (Supplemental Results and Sup. Fig. 5 – 9), we asked whether neural cell proliferation is increased in *xav* mutants compared to WT embryos using BrdU incorporation.

The number of BrdU+ cells was significantly increased throughout the nervous system, in particular in the spinal cord, of *xav* mutants compared to WT embryos at 56-60 hpf (Fig. 6A, 6B). While in ~56-60 hpf WT embryos, there are ~3 BrdU+ cells in the spinal cord per hemisegment, there are ~24 in *xav* mutant embryos at the same developmental stage, resulting in an expansion of the proliferating cellular domain dorso-ventrally and rostro-caudally (Fig. 6A). The peri-ventricular location of these BrdU+

cells suggests that they are likely to be neural progenitor cells (Mueller and Wullimann, 2002, 2003). These observations suggest that neural cell proliferation is increased in the nervous system of *xav* mutants.

***Relationship between increased activation of the PPAR-ERK pathway and increased neural proliferation in xav mutants***

In order to explore the mechanistic relationship between metabolic dysfunction and increased neural proliferation in *xav*, we focused on the PPARG-ERK pathway. PPARG is a known regulator of the cell cycle and apoptosis, and is highly expressed in many cells, including neurons and some human cancer cells (reviewed in Fajas et al., 2001). High levels of PPARG expression have been reported in embryonic mouse brain and neural progenitors, while very low levels have been reported in adult mouse brain (Braissant and Wahli, 1998; Moreno et al., 2004). Recently, PPARG has been shown to regulate neural proliferation *in vitro*, through the activation of ERK and STAT3 (Wada et al., 2006). Because our qRT-PCR analyses showed a dramatic increase in *PPARG* expression in *xav* mutant embryos and MADD patient fibroblasts, this pathway was further examined using Western blot and immunostaining analyses.

Western blot analyses showed that PPARG protein levels were elevated in *xav*, consistent with elevated mRNA expression (Fig. 6D). Western blot and immunostaining analyses were also used to assess ERK activation using a phospho-ERK specific antibody (dp-ERK) (Neumann and Nuesslein-Volhard, 2000). The amount of dp-ERK protein was significantly increased, and dp-ERK immunoreactivity was increased in the spinal cord,

of *xav* compared to WT embryos at ~56 - 60 hpf (Fig. 6A, 6D). BrdU labeling of dividing cells and dp-ERK immunostaining in *xav* mutant embryos at ~56 - 60 hpf revealed a significant increase in the number of double positive BrdU+ / dp-ERK+ cells, from ~0 in WT to ~8 per hemisegment in *xav* mutant embryos at ~56-60 hpf (Fig. 6A, 6C). Furthermore, 45% of the BrdU+ cells were dp-ERK positive. Western blot analyses were then used to assess the level of activated STAT3 protein, using an antibody against phosphorylated STAT3 (phospho-STAT3$^{Tyr705}$) (Yamashita et al., 2002). The amount of phosphorylated STAT3 protein was significantly increased in *xav* embryos (Fig. 6D). These results suggest that the PPARG-ERK pathway is dysfunctional in *xav* mutants, and is associated with increased cell proliferation.

PPARG antagonists and agonists were used to assess the mechanistic relationship between the PPARG-ERK pathway and the increased cell proliferation observed in *xav* mutant embryos. We found that 25 μM of the PPARG antagonist 2,2-Bis[4-(glycidyloxy)phenyl]propane, 4,4′-isopropylidenediphenol diglycidyl ether (BADGE), when applied from 24 – 60 hpf, significantly reduced the number of BrdU+ cells in the spinal cord of *xav* mutants, from ~24 to ~10 cells per hemisegment (Fig. 6E). Furthermore, 10 μM of the PPARG agonist Ciglitizone, when applied to WT embryos from 24 – 60 hpf, significantly increased cell proliferation in the spinal cord, from ~3 to 36 cells per hemisegment (Fig. 6E). Moreover, we found that BADGE, when applied from 24 – 60 hpf, significantly reduced the proportion of *xav* mutants that were paralyzed at ~60 hpf, from 18% to 4%, and also delayed the onset of paralysis by ~12 hours (Fig. 6F; see also Supplemental Results).

Together, these data suggest that aberrant activation of the PPARG-ERK pathway underlies, at least in part, the cell proliferation and behavioral defects that are prominent in *xav* mutants, linking metabolic and mitochondrial dysfunction with defects in nervous system development, and possibly other organ system development, in *xav* mutants and MADD patients.

**Discussion**

We report that the *xav* mutation causes a loss of ETFDH function, and that both *xav* and fibroblasts from MADD patients have similar metabolic defects and mitochondrial dysfunction, including altered energy metabolism, dysregulated ROS production and altered expression of genes critical for mitochondrial function. *xav* and MADD fibroblasts exhibit excessive aerobic glycolysis, similar to the Warburg effect observed in cancer cells, leading to excessive neural proliferation in *xav*, mediated by upregulation of the PPARG-ERK pathway. *xav* mutants also display motility defects culminating in paralysis, abnormal glial patterning, reduced motor axon branching and neuromuscular synapse number, but muscle fiber and neuromuscular synapse function appear normal. While there is increased apoptosis throughout the nervous system, many of these phenotypes are independent of cell death, as they are not rescued when cell death is blocked. Strikingly, a PPARG antagonist attenuates aberrant neural proliferation and alleviates paralysis in *xav*, while PPARG agonists increase neural proliferation in wild type embryos. This work provides further insights into the relationship between metabolism and neural development, specifically that mitochondrial dysfunction that leads to an increase in aerobic glycolysis affects neurogenesis, at least in part through the PPARG-ERK pathway.

The molecular basis of the metabolic pathology in MADD can be explained by the malfunction of fatty acid and choline metabolism as a result of *ETF* or *ETFDH* mutation (Frerman and Goodman, 2001). However, it remains unclear why individuals with MADD exhibit other defects, especially neurological defects including cortex dysplasia,

encephalopathy and leukodystrophy (Bohm et al., 1982; Shevell et al., 1995; Stockler et al., 1994; Takanashi et al., 1999).

While it is not surprising that mutations in ETF genes or ETFDH would lead to impaired fatty acid metabolism, it is interesting that a broader metabolic defect is also present. Our finding that mitochondrial oxidative phosphorylation stimulated by substrates other than fatty acids is also compromised, and that there is a compensatory elevation of complex IV and complex V function, further supports the idea that there is crosstalk among various steps along the energy production pathway.

In most cancer cells and other rapidly proliferating cell populations, ATP is produced primarily by aerobic glycolysis followed by lactate fermentation, rather than by mitochondrial oxidative phosphorylation as in normal, differentiated cells, a phenomenon known as the Warburg effect. The Warburg effect has been proposed as an adaptive strategy to facilitate the uptake and incorporation of essential nutrients needed for increasing cell biomass and proliferation (reviewed in Vander Heiden et al., 2009). Despite understanding that proliferating cells switch from oxidative phosphorylation to aerobic glycolysis, the underlying triggers, effectors and mediators of this switch remain elusive. We show using several cellular and molecular assays that *xav* mutants and MADD fibroblasts exhibit a similar switch, enhanced aerobic glycolysis accompanied by reduced mitochondrial oxygen consumption, the consequence of which is increased cell proliferation, in particular in the nervous system of *xav* mutants. In *xav* mutants, the deficiency of fatty acid metabolism and oxidative phosphorylation may force cells to boost glycolysis as an alternative energy source to preserve viability. This switch may

alter the balance between cell proliferation and differentiation, a major regulator of which is PPARG signaling. In *xav* mutants and MADD fibroblasts, PPARG expression is increased at the mRNA and protein level, and activation of downstream effectors such as ERK and STAT3 are also increased. We showed that PPARG elevation underlies, in large part, the increase in cell proliferation in the nervous system of *xav* mutants by antagonizing this pathway in *xav* and agonizing this pathway in WT embryos. Under physiological conditions, the PPARG pathway may act as a sensor of the balance between oxidative phosphorylation and aerobic glycolysis, and shift the balance between neural cell proliferation and differentiation accordingly.

Using *xav* as a model for MADD, we have gained new insights into the cellular and molecular mechanisms underlying this rare but devastating human disorder. *xav* is the first animal model in which the *etfdh* gene is affected and in which neural defects can be demonstrated and studied. We have also identified the PPARG-ERK pathway as potentially valuable for therapeutic intervention. Understanding the relationship between metabolic and mitochondrial deficiencies and the mechanisms underlying the pathology of MADD, in particular the neurological phenotypes, has been hampered by the rarity of the disorder and thus analyses of autopsy and other tissues has been limited (Frerman and Goodman, 2001). It will be of particular interest to assess neural cell proliferation and other neural phenotypes in MADD patients as tissues become available. The striking phenotypic similarity between *xav* and MADD patient cells suggests that *xav* mutants will be a useful discovery tool to guide future analyses in human MADD patients, and identify avenues for therapeutic intervention.

**References**

Benit, P., Chretien, D., Kadhom, N., de Lonlay-Debeney, P., Cormier-Daire, V., Cabral, A., Peudenier, S., Rustin, P., Munnich, A., and Rotig, A. (2001). Large-scale deletion and point mutations of the nuclear NDUFV1 and NDUFS1 genes in mitochondrial complex I deficiency. Am J Hum Genet 68, 1344-1352.

Bennett, M.J., Ragni, M.C., Hood, I., and Hale, D.E. (1992). Comparison of post-mortem urinary and vitreous humour organic acids. Ann Clin Biochem 29 ( Pt 5), 541-545.

Bohm, N., Uy, J., Kiessling, M., and Lehnert, W. (1982). Multiple acyl-CoA dehydrogenation deficiency (glutaric aciduria type II), congenital polycystic kidneys, and symmetric warty dysplasia of the cerebral cortex in two newborn brothers. II. Morphology and pathogenesis. Eur J Pediatr 139, 60-65.

Bonham, J.R., Tanner, M.S., Pollitt, R.J., Robertson, L., Pourfarzam, M., and Bartlett, K. (1999). Oral sodium 3-hydroxybutyrate, a novel adjunct to treatment for multiple acyl-CoA dehydrogenase deficiency. J. Inher. Metab. Dis. 22, 101-119.

Braissant, O., and Wahli, W. (1998). Differential expression of peroxisome proliferator-activated receptor-alpha, -beta, and -gamma during rat embryonic development. Endocrinology 139, 2748-2754.

Erecinska, M., Cherian, S., and Silver, I.A. (2004). Energy metabolism in mammalian brain during development. Prog Neurobiol 73, 397-445.

Fajas, L., Debril, M.B., and Auwerx, J. (2001). PPAR gamma: an essential role in metabolic control. Nutr Metab Cardiovasc Dis 11, 64-69.

Ferrick, D.A., Neilson, A., and Beeson, C. (2008). Advances in measuring cellular bioenergetics using extracellular flux. Drug Discov Today 13, 268-274.

Frerman, F.E., and Goodman, S.I. (2001). Defects of electron transfer flavoprotein and electron transfer flavoprotein ubiquinone oxidoreductase: glutaric acidemia type II. In The metabolic and molecular bases of inherited diseases. B.A. Scriver CR, Sly WS, Valle D, ed. (New York: McGraw-Hill), pp. 2357-2365.

Hentze, M.W., and Kulozik, A.E. (1999). A perfect message: RNA surveillance and nonsense-mediated decay. Cell 96, 307-310.

Knapik, E.W., Goodman, A., Ekker, M., Chevrette, M., Delgado, J., Neuhauss, S., Shimoda, N., Driever, W., Fishman, M.C., and Jacob, H.J. (1998). A microsatellite genetic linkage map for zebrafish (Danio rerio). Nat Genet 18, 338-343.

Knott, A.B., Perkins, G., Schwarzenbacher, R., and Bossy-Wetzel, E. (2008). Mitochondrial fragmentation in neurodegeneration. Nat Rev Neurosci 9, 505-518.

Langheinrich, U., Hennen, E., Stott, G., and Vacun, G. (2002). Zebrafish as a model organism for the identification and characterization of drugs and genes affecting p53 signaling. Curr Biol 12, 2023-2028.

Lehnert, W., Wendel, U., Lindenmaier, S., and Bohm, N. (1982). Multiple acyl-CoA dehydrogenation deficiency (glutaric aciduria type II), congenital polycystic kidneys, and

symmetric warty dysplasia of the cerebral cortex in two brothers. I. Clinical, metabolical, and biochemical findings. Eur J Pediatr 139, 56-59.

Loeffen, J.L., Smeitink, J.A., Trijbels, J.M., Janssen, A.J., Triepels, R.H., Sengers, R.C., and van den Heuvel, L.P. (2000). Isolated complex I deficiency in children: clinical, biochemical and genetic aspects. Hum Mutat 15, 123-134.

Mattson, M.P., Gleichmann, M., and Cheng, A. (2008). Mitochondria in neuroplasticity and neurological disorders. Neuron 60, 748-766.

McKean, M.C., Beckmann, J.D., and Frerman, F.E. (1983). Subunit structure of electron transfer flavoprotein. J Biol Chem 258, 1866-1870.

Moreno, S., Farioli-Vecchioli, S., and Ceru, M.P. (2004). Immunolocalization of peroxisome proliferator-activated receptors and retinoid X receptors in the adult rat CNS. Neuroscience 123, 131-145.

Mueller, T., and Wullimann, M.F. (2002). BrdU-, neuroD (nrd)- and Hu-studies reveal unusual non-ventricular neurogenesis in the postembryonic zebrafish forebrain. Mech Dev 117, 123-135.

Mueller, T., and Wullimann, M.F. (2003). Anatomy of neurogenesis in the early zebrafish brain. Brain Res Dev Brain Res 140, 137-155.

Nam, D.H., Ramachandran, S., Song, D.K., Kwon, K.Y., Jeon, D.S., Shin, S.J., Kwon, S.H., Cha, S.D., Bae, I., and Cho, C.H. (2007). Growth inhibition and apoptosis induced

in human leiomyoma cells by treatment with the PPAR gamma ligand ciglitizone. Mol Hum Reprod 13, 829-836.

Neumann, C.J., and Nuesslein-Volhard, C. (2000). Patterning of the zebrafish retina by a wave of sonic hedgehog activity. Science 289, 2137-2139.

Nona, S.N., Shehab, S.A., Stafford, C.A., and Cronly-Dillon, J.R. (1989). Glial fibrillary acidic protein (GFAP) from goldfish: its localisation in visual pathway. Glia 2, 189-200.

Panzer, J.A., Gibbs, S.M., Dosch, R., Wagner, D., Mullins, M.C., Granato, M., and Balice-Gordon, R.J. (2005). Neuromuscular synaptogenesis in wild-type and mutant zebrafish. Dev Biol 285, 340-357.

Rinaldo, P., Matern, D., and Bennett, M.J. (2002). Fatty acid oxidation disorders. Annu Rev Physiol 64, 477-502.

Robu, M.E., Larson, J.D., Nasevicius, A., Beiraghi, S., Brenner, C., Farber, S.A., and Ekker, S.C. (2007). p53 activation by knockdown technologies. PLoS Genet 3, e78.

Russell, A.P., Schrauwen, P., Somm, E., Gastaldi, G., Hesselink, M.K., Schaart, G., Kornips, E., Lo, S.K., Bufano, D., Giacobino, J.P., Muzzin, P., Ceccon, M., Angelini, C., and Vergani, L. (2003). Decreased fatty acid beta-oxidation in riboflavin-responsive, multiple acylcoenzyme A dehydrogenase-deficient patients is associated with an increase in uncoupling protein-3. J Clin Endocrinol Metab 88, 5921-5926.

Ruzicka, F.J., and Beinert, H. (1977). A new iron-sulfur flavoprotein of the respiratory chain. A component of the fatty acid beta oxidation pathway. J Biol Chem 252, 8440-8445.

Schiff, M., Froissart, R., Olsen, R.K., Acquaviva, C., and Vianey-Saban, C. (2006). Electron transfer flavoprotein deficiency: functional and molecular aspects. Mol Genet Metab 88, 153-158.

Shen, J.J., Matern, D., Millington, D.S., Hillman, S., Feezor, M.D., Bennett, M.J., Qumsiyeh, M., Kahler, S.G., Chen, Y.T., and Van Hove, J.L. (2000). Acylcarnitines in fibroblasts of patients with long-chain 3-hydroxyacyl-CoA dehydrogenase deficiency and other fatty acid oxidation disorders. J Inherit Metab Dis 23, 27-44.

Shevell, M.I., Didomenicantonio, G., Sylvain, M., Arnold, D.L., O'Gorman, A.M., and Scriver, C.R. (1995). Glutaric acidemia type II: neuroimaging and spectroscopy evidence for developmental encephalomyopathy. Pediatr Neurol 12, 350-353.

Shimoda, N., Knapik, E.W., Ziniti, J., Sim, C., Yamada, E., Kaplan, S., Jackson, D., de Sauvage, F., Jacob, H., and Fishman, M.C. (1999). Zebrafish genetic map with 2000 microsatellite markers. Genomics 58, 219-232.

Stockler, S., Radner, H., Karpf, E.F., Hauer, A., and Ebner, F. (1994). Symmetric hypoplasia of the temporal cerebral lobes in an infant with glutaric aciduria type II (multiple acyl-coenzyme A dehydrogenase deficiency). J Pediatr 124, 601-604.

Takanashi, J., Fujii, K., Sugita, K., and Kohno, Y. (1999). Neuroradiologic findings in glutaric aciduria type II. Pediatr Neurol 20, 142-145.

Triepels, R.H., Van Den Heuvel, L.P., Trijbels, J.M., and Smeitink, J.A. (2001). Respiratory chain complex I deficiency. Am J Med Genet 106, 37-45.

Van Hove, J.L., Grunewald, S., Jaeken, J., Demaerel, P., Declercq, P.E., Bourdoux, P., Niezen-Koning, K., Deanfeld, J.E., and Leonard, J.V. (2003). D,L-3-hydroxybutyrate treatment of multiple acyl-CoA dehydrogenase deficiency (MADD). Lancet 361, 1433-1435.

Vander Heiden, M.G., Cantley, L.C., and Thompson, C.B. (2009). Understanding the Warburg effect: the metabolic requirements of cell proliferation. Science 324, 1029-1033.

Wada, K., Nakajima, A., Katayama, K., Kudo, C., Shibuya, A., Kubota, N., Terauchi, Y., Tachibana, M., Miyoshi, H., Kamisaki, Y., Mayumi, T., Kadowaki, T., and Blumberg, R.S. (2006). Peroxisome proliferator-activated receptor gamma-mediated regulation of neural stem cell proliferation and differentiation. J Biol Chem 281, 12673-12681.

Wallace, D.C. (1999). Mitochondrial diseases in man and mouse. Science 283, 1482-1488.

Wallace, D.C. (2005). A mitochondrial paradigm of metabolic and degenerative diseases, aging, and cancer: a dawn for evolutionary medicine. Annu Rev Genet 39, 359-407.

Watanabe, M., Houten, S.M., Mataki, C., Christoffolete, M.A., Kim, B.W., Sato, H., Messaddeq, N., Harney, J.W., Ezaki, O., Kodama, T., Schoonjans, K., Bianco, A.C., and Auwerx, J. (2006). Bile acids induce energy expenditure by promoting intracellular thyroid hormone activation. Nature 439, 484-489.

Willer, G.B., Lee, V.M., Gregg, R.G., and Link, B.A. (2005). Analysis of the Zebrafish perplexed mutation reveals tissue-specific roles for de novo pyrimidine synthesis during development. Genetics 170, 1827-1837.

Yamashita, S., Miyagi, C., Carmany-Rampey, A., Shimizu, T., Fujii, R., Schier, A.F., and Hirano, T. (2002). Stat3 Controls Cell Movements during Zebrafish Gastrulation. Dev Cell 2, 363-375.

Zannino, D.A., and Appel, B. (2009). Olig2+ precursors produce abducens motor neurons and oligodendrocytes in the zebrafish hindbrain. J Neurosci 29, 2322-2333.

**Figures and Legends**

**Figure 1. *xavier* external phenotype, genotype, cloning and morpholino phenocopy of *xav* mutants**

**A**. External *xav* and *etfdh* morphant (MO) phenotypes at ~60 hpf include a bent and thinner tail and smaller head and eyes. Scale bar = 100 μm. **B.** *xav* mutants and MO exhibit slower heart beat (WT 158 ± 6 beats / minute, N = 13 embryos; *xav* 87 ± 7; N = 14 embryos; MO 65 ± 7, N = 14 embryos; one-way ANOVA, followed by Dunn's pairwise comparison, * $p < 0.001$. **C.** Genetic and physical map of the *xav* (zgc:92093) locus (red), including microsatellite and SSR markers, number of recombinants, and BAC clones from the T51 radiation hybrid panel. **D.** *etfdh* mutation in *xav* is a T to A mutation (blue box) resulting in a premature stop codon (red box). The amino acid sequence of etfdh is highly conserved among several species, from C. elegans to human. **E.** Schematic location of *xav* mutation, resulting in truncation of the C terminal. *etfdh* MO is predicted to give rise to a protein fragment lacking all functional domains.

**Figure 1. *xavier* external phenotype, genotype, cloning and morpholino phenocopy of *xav* mutants**

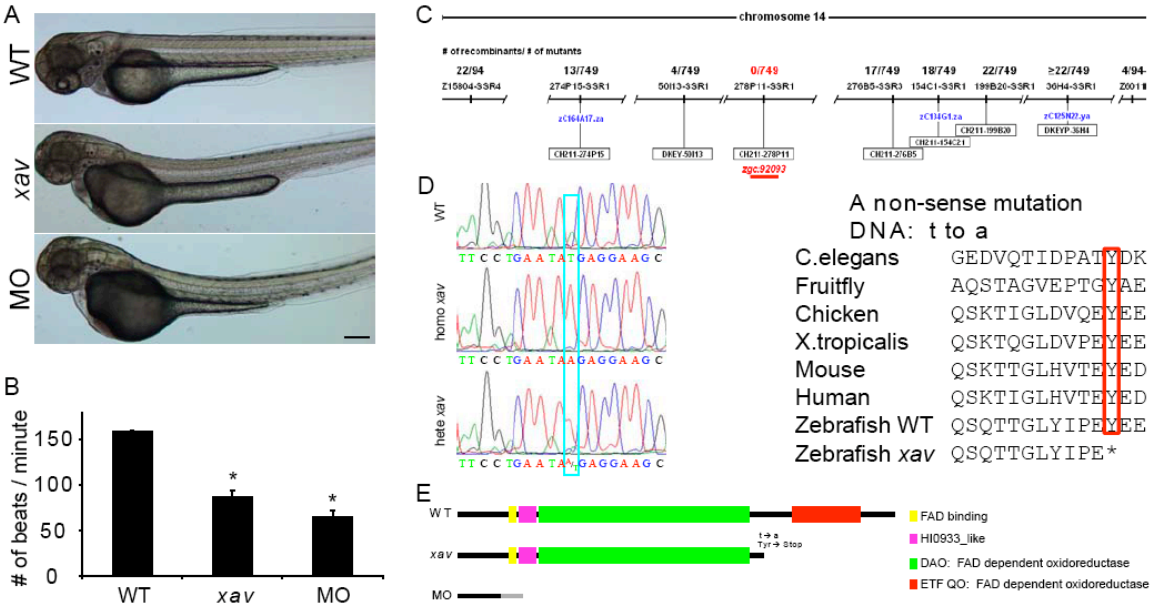

**Figure 2. *xavier* mutants display abnormal acylcarnitine and organic acid profile**

**A.** Representative acylcarnitine profile from homogenates of WT and *xav* mutant embryos using mass spectroscopy, showing a markedly higher level of several intermediate acyl-fatty acid species in *xav* mutants including C4, C5, C6, C8, C14, C16 and C18, and a reduction of C2 actylcarnitine (pool of ~100 embryos for *xav* mutant and WT at ~56 hpf). **B.** Representative organic acid profile from homogenates of WT and *xav* mutant embryos using gas chromatographic analysis, showing an elevation of the level of glutaric acid in *xav* mutants (black arrow) (pool of ~100 embryos for *xav* mutant and WT at ~56 hpf).

**Figure 2. *xavier* mutants display abnormal acylcarnitine and organic acid profile**

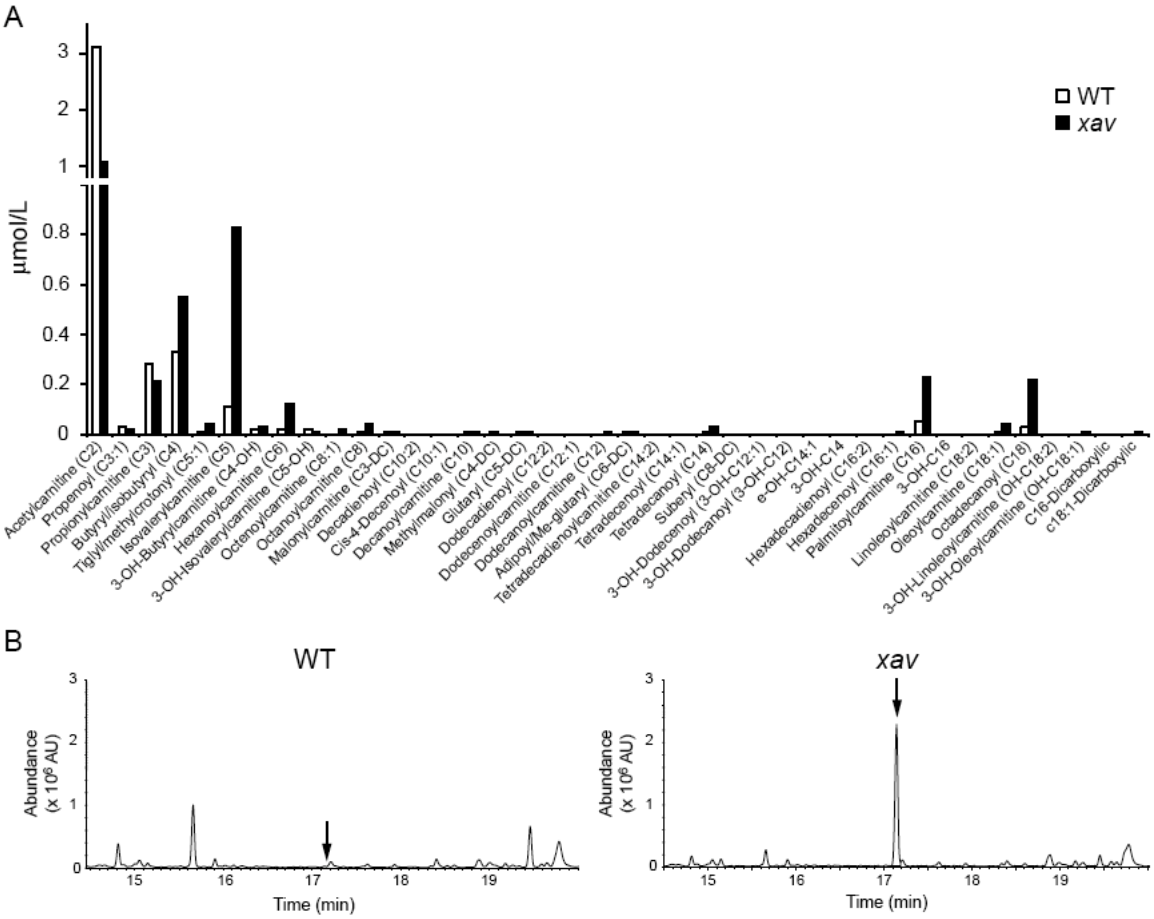

**Figure 3. *xav* mutants exhibit mitochondrial dysfunction**

**A.** Measured state 3 respiration stimulated by α-ketoglutarate and fatty acids showed a 30-35% reduction in *xav* mutant compared to WT embryos at ~56 hpf (values normalized to WT; α-ketoglutarate in *xav*, 0.72 ± 0.10; N = 4 experiments 50-100 embryos each; Student's t test, * p=0.03; fatty acid 0.65 ± 0.10 in *xav*; N= 4 experiments 50-100 embryos each; Student's t test, * p=0.02). **B.** Membrane potential stimulated by α-ketoglutarate and fatty acids was measured using TMRE and spectrofluorometry, showing a 55% increase in *xav* compared to WT at ~56 hpf (values normalized to WT; α-ketoglutarate *xav* 1.55 ± 0.15; N = 4 experiments 50-100 embryos each; Student's t test, *** p<0.001) and a 50% reduction (fatty acids *xav* 0.53 ± 0.07; N= 5 experiments 50-100 embryos each; Student's t test, *** p<0.001). **C.** Measured $O_2$ consumption rated stimulated by TMPD/ascorbate showed a 40% increase in *xav* compared to WT at ~56 hpf (values normalized to WT; *xav* 1.39 ± 0.13; N= 6 experiments 50-100 embryos each; Student's t test, * p=0.014). **D-E.** Western blot showed that while the total level of AMPK is unchanged in *xav*, the amount of activated AMPK (phospho-AMPK$\alpha^{Thr172}$) protein is significantly increased. Quantification showed a 2.3 fold increase in *xav* mutants compared to WT embryos (values normalized to WT; *xav* 2.3 ± 0.6; N= 3 experiments 30 embryos each; Student's t test, * p < 0.05). **F.** Measurement of ATP production showed a ~45% reduction in *xav* mutants compared to WT embryos (WT 20.6 ± 2.6 nmol per mg protein; *xav* 11.3 ± 2.3 nmol per mg protein; N= 9 replicates, 50-100 embryos each, Student's t test, * p<0.05). **G.** mRNA levels of genes involved in mitochondrial function and biogenesis were analyzed with qRT-PCR. A ~30-40%

reduction was observed in *mt-nd5* and *ndufs1*, and a ~2.4, 1.5 and 2.8 fold increase was observed in *pgc-1β*, *esrrα* and *pparγ* in *xav* mutants compared to WT. Expression of zebrafish *uncoupling protein 4* (*fucp4*) was increased ~6 fold, while expression of *ucp2* was unchanged (N = 3-4 replicates, 20 embryos each; Student's t test, * $p<0.05$, ** $p<0.01$, *** $p<0.001$). **H.** The oxidative fluorescent dye DHR-123 was used to measure cellular superoxide production in live embryos and showed higher cellular superoxide levels in *xav* mutants compared to WT, especially in the nervous system, including in the spinal cord. Scale bar = 100 μm. **I.** Expression profile of genes known to be involved in the ROS pathway was assayed with qRT-PCR and showed a ~50% reduction of *catalase* transcripts and ~5 fold increase of *glutathione reductase* and *hspa9* in *xav* compared to WT (N = 3 replicates, 20 embryos each; Student's t test, * $p<0.05$, ** $p<0.01$).

**Figure 3. *xav* mutants exhibit mitochondrial dysfunction**

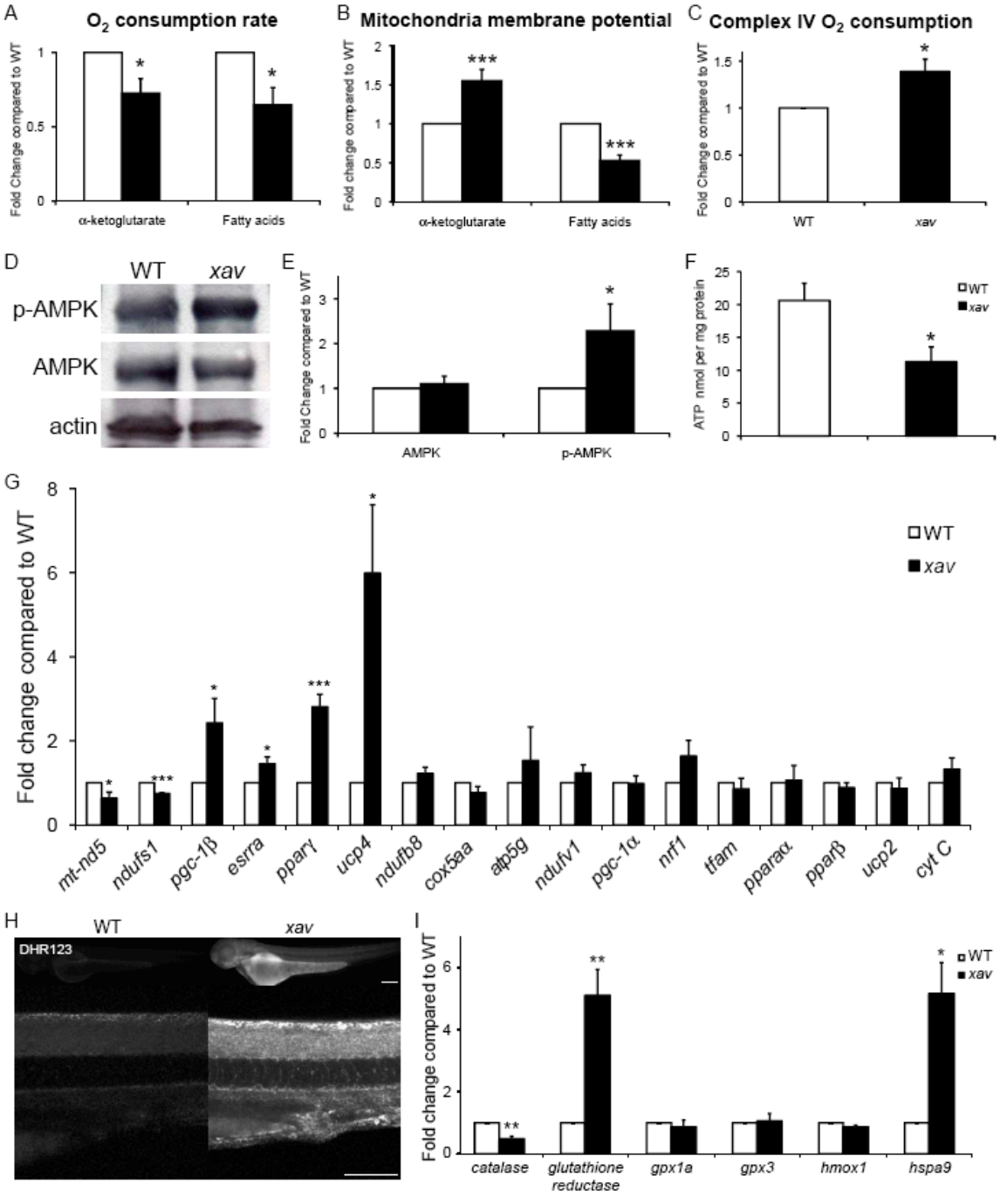

**Figure 4. Human MADD fibroblast cells display similar mitochondrial defects as *xav***

**A.** Oxygen consumption was measured in intact control and MADD Patient WH fibroblasts under basal conditions, following the addition of the mitochondrial inhibitor oligomycin (0.5 μg/ml), in the presence of the uncoupler CICCP (3 μM) and with the addition of complex I inhibitor Rotenone (100 nM). A 2-fold increase was observed in Patient WH fibroblasts compared to control, after uncoupler CICCP treatment, which measures the reserved mitochondrial oxidative capacity (N = 3 experiments, 7-9 replicates of cells from passage 7-12; Student's t test, *** $p<0.001$). **B.** Measurement of ATP levels showed a ca. 10% reduction in MADD Patient WH fibroblast cells compared to control (N = 14 replicates of cells from passage 7-12; Student's t test ,* $p<0.05$). **C.** Gene expression assayed by qRT-PCR revealed that *PGC-1β*, *PPARG*, *ESRRα*, *UCP3* were increased ~2, 4.6, 2 and 1.6 fold in Patient WH compared to control. The expression of ROS related genes are also altered in Patient WH, with a ca. 20% decrease in *catalase* and 4.7 and 5.7 fold increase in *glutathione reductase* and *HSPA9* expression (N = 3-7 replicates of cells from passage 7-12; Student's t test, * $p<0.05$, ** $p<0.01$, *** $p<0.001$).

**Figure 4. Human MADD fibroblast cells display similar mitochondrial defects as *xav***

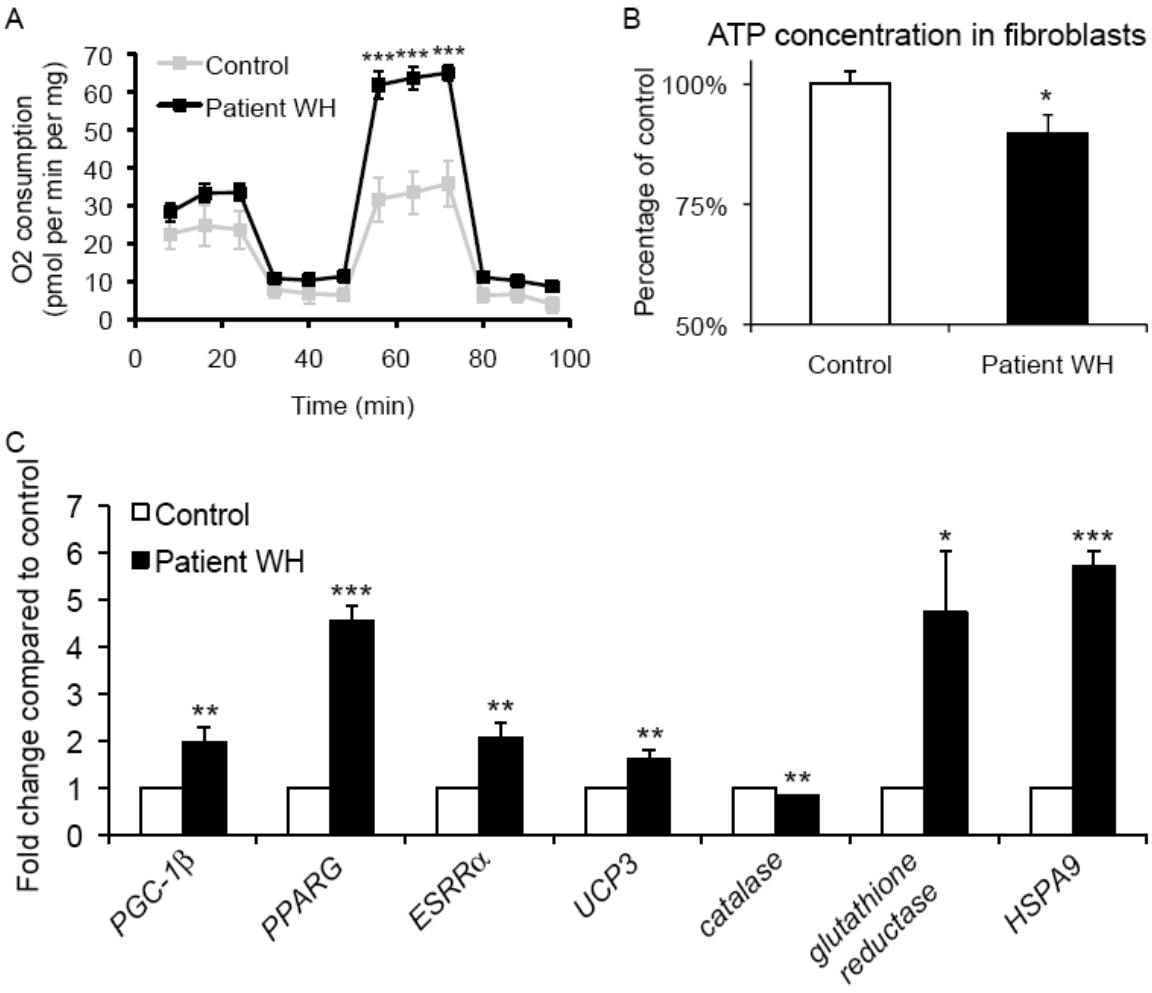

**Figure 5. Increased aerobic glycolysis in MADD fibroblasts and *xav***

**A.** ECAR was measured in intact control and MADD Patient WH fibroblasts under basal conditions, following the addition of the mitochondrial inhibitor oligomycin (0.5 μg/ml), in the presence of the uncoupler CICCP (3 μM) and the addition of complex I inhibitor Rotenone (100 nM). A trend towards higher ECAR rate was seen under basal conditions, and a significant 2-fold increase was observed after uncoupler CICCP treatment in Patient WH fibroblasts compared to control. (N = 3 experiments, 7-9 replicates of cells from passage 7-12; Student's t test, * $p<0.05$). **B.** Measurement of lactate secreted into the culture medium showed a ~20% increase in the basal lactate production in Patient WH fibroblasts compared to control (N = 2 experiments, 5-6 replicates of cells from passage 7-8; Student's t test, * $p<0.05$). **C.** qRT-PCR analyses of genes involved in glycolysis showed glycolytic enzymes *enolase 1* (*ENO1*), *phosphoglycerate mutase 1* (*PGAM1*), *phosphoglycerate kinase 1* (*PGK1*) and *phosphofructokinase* (*PFKM*), were increased by ~1.9, 2.7, 3.4 and 3.1 fold respectively in Patient WH fibroblasts compared to control (N = 5 replicates of cells from passage 7-9; Student's t test, * $p<0.05$, *** $p<0.001$). **D.** Measurement of lactate levels showed a ~2.4 fold increase in *xav* mutants compared to WT embryos at ~56 hpf (N = 7-9 replicates, 30-100 embryos each; Student's t test, * $p<0.05$). **E.** qRT-PCR analyses of gene expression revealed increased expression of glycolytic enzymes *eno1*, *pgam1a*, *pgk1*, *pfkma*, and *fructose-biphosphate aldolase C* (*aldoc*) by 2.8, 2, 1.9, 1.8 and 2.1 fold respectively, as well a ~20% decrease in *dihydrolipoamide S-acetyltransferase* (*dlat*), that belongs to the pyruvate dehydrogenase complex, which links glycolysis to tricarboxylic

acid (TCA) cycle, in *xav* mutants compared to WT embryos at ~56 hpf (N = 3-7 replicates, 20 embryos each; Student's t test, * $p<0.05$, ** $p<0.01$).

**Figure 5. Increased aerobic glycolysis in MADD fibroblasts and *xav***

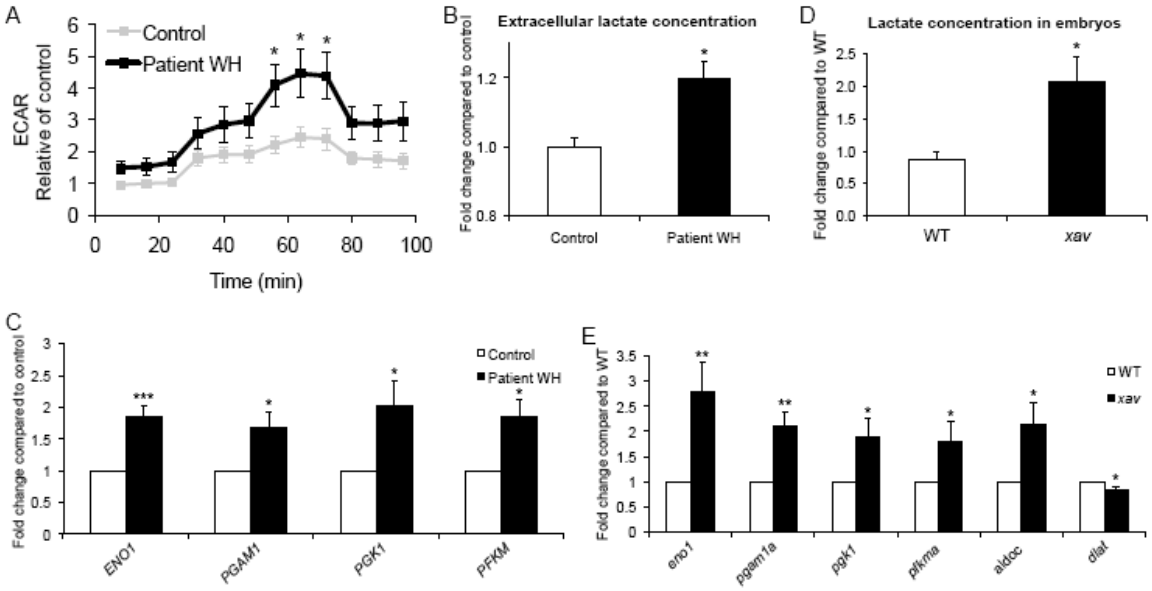

**Figure 6. *xav* exhibits increased neural cell proliferation as a result of increased glycolysis, due to perturbation of the PPARG-ERK pathway**

**A.** Whole mount embryos labeled with BrdU to mark cells undergoing proliferation. The number of BrdU+ cells was significantly increased in the nervous system, especially in the spinal cord, in *xav* mutants compared to WT embryos at ~56-60 hpf. Increased dp-ERK+ cells and BrdU+ / dp-ERK+ double labeled cells in the spinal cord in *xav* mutants compared to WT embryos at ~56-60 hpf. **B.** In spinal cord cross-sections from *xav* mutants and WT embryos at ~56-60 hpf, BrdU+ cells are distributed peri-ventricularly, suggesting that they are likely to be neural progenitor cells. Dashed line outlines the spinal cord and indicates the midline. Scale bar = 20 μm. **C.** Quantification of BrdU+ and dp-ERK+ cells at ~56-60 hpf. Per spinal cord hemisegment: BrdU+ cells WT 3.2 ± 0.4, *xav* 24 ± 1.4; dp-ERK+ cells WT 2.6 ± 0.3, *xav* 19.4 ± 0.8; BrdU+ / dp-ERK+ WT 0.2 ± 0.2, *xav* 7.8 ± 1.2. Percent of BrdU+ cells that are also dp-ERK+: WT 3.6% ± 3.6%, *xav* 45% ± 8% (N = 4-19 embryos, >2 carrier pairs; Student's t test, *** $p<0.001$). **D.** Western blot analyses of pparγ, dp-ERK and phospho-STAT3 expression showed dramatic increase in *xav* compared to WT embryos at ~56-60 hpf (N = 3 replicates, 30 embryos each; Student's t test, * $p<0.05$). **E.** BrdU labeling of proliferating cells in whole mounts of spinal cord of WT embryos, *xav* mutants, WT treated with 25 μm BADGE, *xav* mutants treated with 25 μm BADGE and WT treated with 10 μm Ciglitizone at ~56-60 hpf. Embryos were raised in BADGE or Ciglitizone from 24 to 60 hpf. Per spinal hemisegment: BrdU+ cells WT 3.2 ± 0.4, WT + BADGE 4.5 ± 0.3, *xav* 24 ± 1.4, *xav* + BAGDE 10.6 ± 0.9, WT + Ciglitizone 36 ± 2.5

(N = 6-19 embryos, >3 carrier pairs; one-way ANOVA, followed by Bonferroni's multiple comparison test, *** $p<0.001$).

**Figure 6. *xav* exhibits increased neural cell proliferation as a result of increased glycolysis, due to perturbation of the PPARG-ERK pathway**

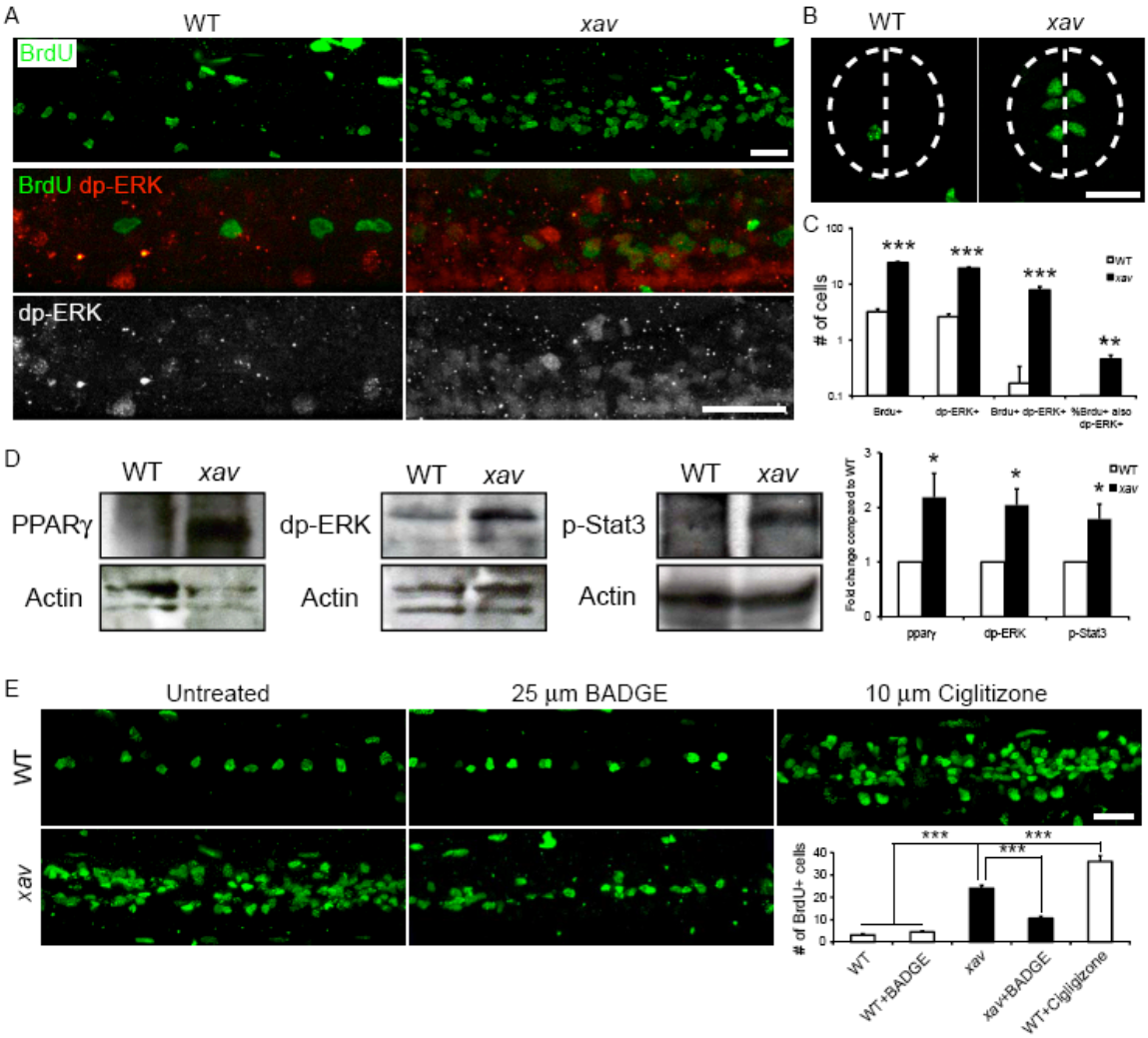

## SUPPLEMENTAL INFORMATION

### Supplemental Materials and Methods

#### Behavioral assessment of *xav* mutants and wild type embryos

Gross motility was assessed via head and/or tail tap with a fine plastic probe, and elicited movements observed under a stereomicroscope (Leica MZ12.5). The behavior was recorded using high-speed video microscopy (800 frames/ s; MotionPro 2000, Redlake), Supplemental Video 1 and 2.

#### Immunostaining and TUNEL assay

Embryos were anesthetized, fixed and immunostained as described previously (Panzer et al., 2005) using antibodies against the presynaptic neurotransmitter vesicle protein SV2 (Developmental Studies Hybridoma Bank (DSHB)), Zn5 (DSHB) and/or the glial specific protein GFAP (Nona et al., 1989) (gift from Drs. S. Nona and J. Scholes, Univ. of Sussex, United Kingdom), complex V (Invitrogen) and the appropriate fluorescently conjugated secondary antibody (Jackson Labs). To label AChRs, fluorescently conjugated α–bungarotoxin (Invitrogen) was used as described previously (Panzer et al., 2005). Presynaptic vesicles, AChR clusters and the co-localization of these two markers were measured from single plane projections of confocal image stacks using interactive software (Metamorph). For immunostaining of NaK ATPase with α6F (DHSB) together with Acetyl-tub (Sigma), embryos were fixed in Dent's fix (Drummond

et al. 1998). For sections, fixed embryos were incubated in 20% sucrose, embedded in OCT and cut into 20 μm sections.

TUNEL staining was performed according to the manufacturer's instructions (Chemicon).

**p53 morpholino injection**

A morpholino antisense oligonucleotide (Gene Tools) targeting p53 (GCGCCATTGCTTTGCAAGAATTG) (Langheinrich et al., 2002) was injected at the 1-2 cell stage at ~8 ng. Embryos were assessed at 56-72 hpf using the TUNEL assay.

**Mitochondria labeling in motor neurons**

An *hb9*:mito-GFP construct was generated by inserting mito-GFP (obtained from Drs. Marnie Halpern and Bill Saxton, Carnegie Inst. for Dev. Biology, Baltimore, MD) into an I-Sce vector containing *hb9* promoter (obtained from Dr. Michael Granato, Univ. of Pennsylvania Sch. Medicine and Dr. Dirk Meyer, Albert-Ludwigs University, Freiburg, Germany). DNA (50 ng/μl) was injected into 1-2 cell stage embryos, which were then raised to 24-48 hpf for assessing expression in motor neurons using confocal microscopy.

## Supplemental Results

### *Kidney defects in xav mutants*

Given that congenital polycystic kidneys have been reported in MADD patients (Bohm et al., 1982; Lehnert et al., 1982), we asked whether *xav* mutants display similar phenotypes. Immunostaining of whole mount embryos at ~60 hpf revealed that the cilia in the pronephric ducts, as stained by anti-acetylated tubulin, appear distended and irregularly thickened, and contain gaps, in *xav* mutants compared to WT embryos (Sup. Fig. 3). Pronephric duct epithelial cells, as labeled by an anti-NaK ATPase antibody, appear irregular in shape and showed aberrant clustering in *xav* embryos (Sup. Fig. 3). This result suggests that *xav* exhibit kidney morphological defects similar to those in MADD patients.

### *xav mutants exhibit abnormal motility and progressive paralysis*

*xav* mutants exhibited several behavioral deficits. While *xav* mutant embryos are normally motile up until 48 hpf, at this time, increased spontaneous muscle twitching and spastic movements are observed in mutants, while WT embryos are largely stationary unless stimulated (percent of time spent continuously moving, WT 0.4% ± 0.3%, *xav* 12% ± 4%, N = 3-5 embryos, 1 carrier pair, Student's t test, $p<0.05$) (Supplemental Video 1 and 2). However, once stimulated, WT embryos respond with a characteristic C-bend and swimming escape response (Panzer et al., 2005), but *xav* mutants, despite executing a C-bend similar to that in WT embryos, do not exhibit a normal swimming

escape response. *xav* mutants swim with reduced speed and distance, often ending in twitching movements (Supplemental Video 1 and 2). Moreover, by ~60 hpf, *xav* mutants are completely paralyzed (Panzer et al., 2005).

***xav mutants exhibit several neural phenotypes, including reduced neuropil staining and aberrant glial patterning***

Several analyses were performed to qualitatively assess the central and peripheral nervous system in *xav* mutants compared to WT embryos, to further understand the neural defects in *xav*, and provide insight into those neural defects that may be present in MADD patients, as this is a poorly explored aspect of the disorder due to its rarity (Frerman and Goodman, 2001).

At 3 dpf, *xav* embryos exhibited reduced neuropil as assayed by SV2 staining (Sup. Fig. 5). Glia number and patterning as assayed by GFAP staining was aberrant throughout the nervous system (Sup. Fig. 5). Not only were glial processes irregular in shape, but clumps of GFAP+ cells were observed in several brain regions (Sup. Fig. 5 and data not shown). These observations suggest that, in addition to neural cell proliferation defects, several aspects of neural development are impaired in *xav*, due to metabolic and mitochondria deficiency.

***xav mutants exhibit reduced motor axon branching, reduced neuromuscular synapse number and abnormal mitochondria distribution within motor neuron axons and at synapses***

*xav* mutants exhibit reduction of motor axon branching, and a reduction of neuromuscular synaptogenesis, at 56 hpf and most strikingly at 72 hpf (Sup. Fig. 6A; (Panzer et al., 2005)). Motor neuron number, as assayed by in situ hybridization for *islet-2*, is similar between *xav* mutants and WT embryos at 48 hpf (Sup. Fig. 6B). Moreover, there is no substantial apoptosis in the pool of motor neurons, as assayed by double staining for TUNEL and Zn5, which labels secondary motor neurons (Sup. Fig. 6C). These data suggest that the reduction in motor axon branching and neuromuscular synaptogenesis are not due to a decrease in motor neuron number.

To determine whether motor neurons and muscle fibers function normally in *xav* mutants, electrophysiological assays were performed in *xav* mutants and WT embryos. Miniature excitatory postsynaptic current (mEPC) recordings from fast muscles showed no statistical difference in terms of frequency, amplitude, rise time and exponential decay time (Sup. Fig. 7A, 7B, 7C). Furthermore, muscle fibers from *xav* embryos fire action potentials after exogenous stimulation, comparable to muscle fibers from WT embryos (Sup. Fig. 7D). These data suggest that despite a reduction of neuromuscular synapses in *xav* mutants, the physiological properties of postsynaptic muscle fibers are not compromised, making the possibility of deteriorative and nonspecific effects in muscle fibers an unlikely explanation for the morphological and motility defects. Thus, either

defects intrinsic to presynaptic motor neurons, and/or circuitry in the spinal cord and/or other CNS regions, is responsible for the observed paralysis in *xav* mutants.

We next assessed the distribution of mitochondria within motor neurons. Mito-GFP was expressed in motor neurons and branching and synapse formation followed over time. In WT embryos at ~56 hpf, mitochondria are distributed along the entire axon and some appear to be clustered (Sup. Fig. 8A). The majority of mitochondria clusters are at synapses, with some along the axon and branches (data not shown). Mitochondria clusters are continuously added over time, increasing both in number and density (Sup. Fig. 8A, 8B). In contrast, in *xav* mutants, while the number and distribution of mitochondria clusters along the axon are comparable to WT embryos at ~56 hpf, the continuous addition of mitochondria is absent, resulting in a decrease of mitochondria cluster density over time (Sup. Fig. 8A, 8B). These results suggest that the number, distribution and addition of mitochondria is impaired in *xav* mutants.

***xav mutants exhibit cell death throughout the nervous system that is rescued by p53 morpholino knockdown and does not account for the motor axon branching, neuromuscular synapse or motility defects***

A particularly prominent phenotype in *xav* mutants is the widespread cell death observed in the peripheral nervous system, and most strikingly in the CNS, compared to other tissues. There was a dramatic increase in TUNEL+ cells in *xav* mutants compared to WT embryos at ~56-72 hpf, particularly in the retina and spinal cord (Sup. Fig. 9A).

That TUNEL+ cells were not observed in all tissues argues against generalized cell death due to metabolic insufficiency.

Given prominent apoptotic cell death throughout the nervous system, we asked whether blocking cell death may abrogate any *xav* neural and behavioral phenotypes. Cell death was blocked using a morpholino against p53 (Langheinrich et al., 2002; Robu et al., 2007) and *xav* and WT embryos were assessed at ~56 hpf. *xav* mutants injected with p53 morpholino exhibited levels of cell death that were indistinguishable from WT in the central and peripheral nervous system (Sup. Fig. 9B). However, blocking cell death did not block the reduction of axon branching and synaptogenesis phenotypes that are present in *xav* mutants, as these phenotypes were similar between *xav* mutants and *xav* mutants injected with p53 morpholino (Sup. Fig. 9B). Moreover, *xav* mutants injected with p53 morpholino exhibited motility deficits that were indistinguishable from *xav* mutants, including the proportion of embryos paralyzed at ~56-60 hpf (data not shown). This result suggests that cell death per se is unlikely to account for the axon branching, synaptogenesis or paralysis phenotypes prominent in *xav* mutants.

## Supplemental Figures and Legends

### Supplemental Figure 1. Genetic map of the *xav* locus

Conserved synteny between genes in the *xav* interval and human chromosome 4. *xav* linkage results suggest the sequence in and around BAC clone DKEY-50I13 (accession no. CR846102.12) is misplaced on the Ensembl Zv6 genome build.

**Supplemental Figure 1. Genetic map of the *xav* locus**

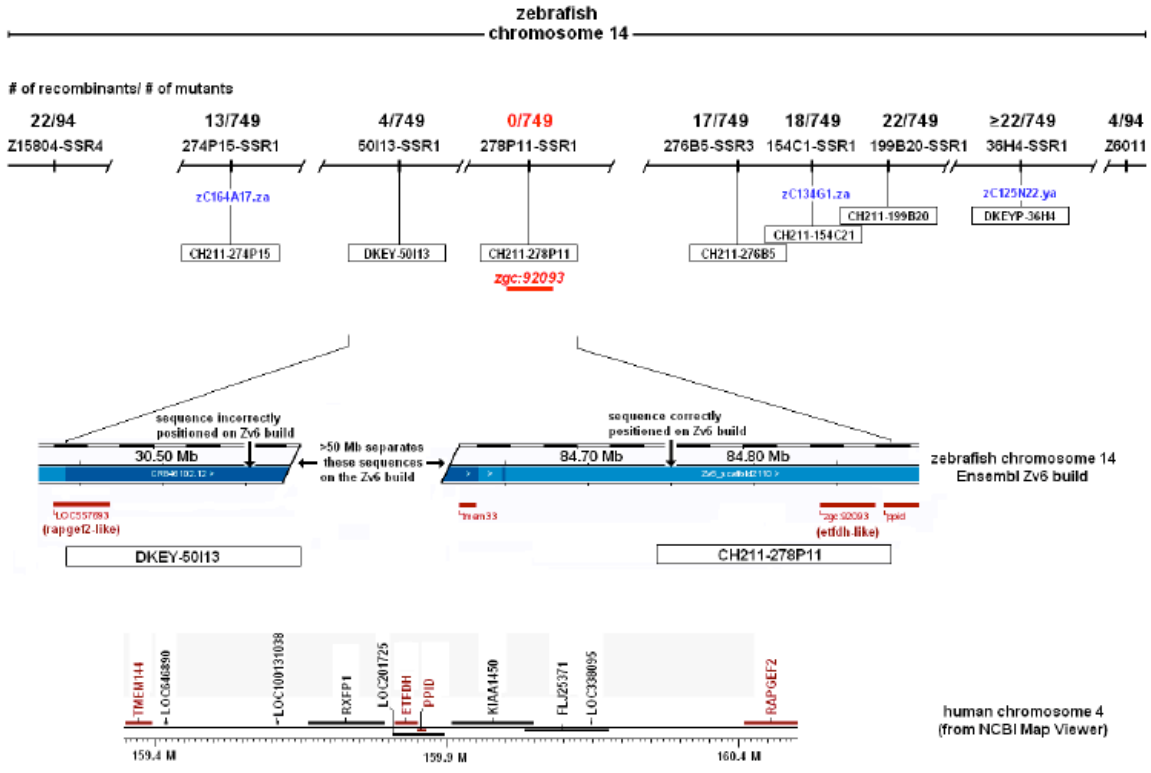

**Supplemental Figure 2. Nonsense mediated decay and nonsense mediated alternative splicing of *etfdh* transcript in *xav,* and morpholino knock down of *etfdh***

**A.** qRT-PCR showed that there is a significant, ~80% reduction of *etfdh* mRNA in *xav*, likely due to nonsense mediated decay. N = 3 pools of 20 embryos each for WT and *xav*; Student's t test, * $p<0.0001$. **B.** *xav* mutants showed nonsense mediated alternative splicing. As a result of the mutation, which resides in exon11, the exon10-exon13 junctions are mis-spliced in mutants, resulting in transcripts that are predicted to encode proteins lacking critical domains or truncated. Blue arrows indicate primer location. These results suggest that the *xav* mutation is likely to be loss of function. **C.** A splice-blocking morpholino against intron2-exon3 (MOI2E3) was designed for *etfdh*. **D.** Injection of 8 ng *etfdh* MOI2E3 in WT embryos, results in > 80% reduction of the normal transcript at 2 and 3 dpf, producing a mis-spliced transcript that lacks exon3. Red arrow indicates the MO location and blue arrows indicate primer location.

**Supplemental Figure 2. Nonsense mediated decay and nonsense mediated alternative splicing of *etfdh* transcript in *xav,* and morpholino knock down of *etfdh***

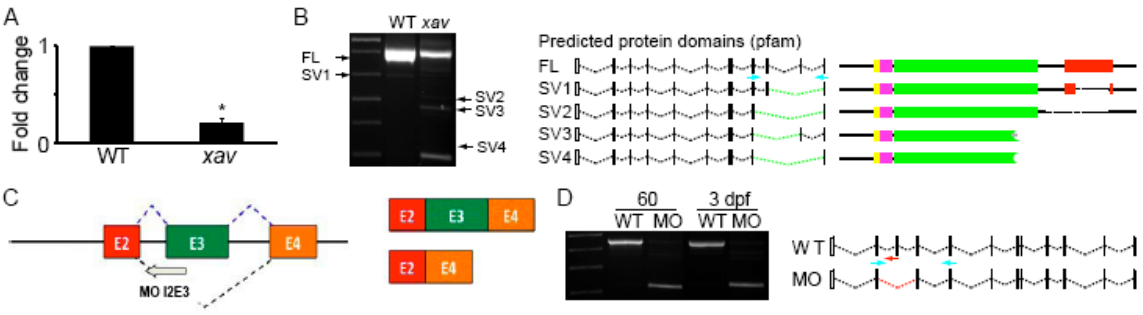

**Supplemental Figure 3. *xav* mutants display polycystic kidney like phenotypes.**

Immunostaining of whole mount zebrafish embryos revealed that the cilia in the pronephric ducts, as labeled by immunostaining with anti-acetylated tubulin antibody, appear distended and irregularly thickened, and contain gaps, in xav mutants compared to WT embryos at ~60 hpf. Pronephric duct epithelial cells, as labeled by immunostaining with the anti-NaK ATPase antibody $\alpha$6F, appear irregular in shape and showed aberrant clustering in *xav* embryos. N = > 10 xav and WT embryos for each immunostaining assessment. Scale bar = 20 $\mu$m.

**Supplemental Figure 3. *xav* mutants display polycystic kidney like phenotypes.**

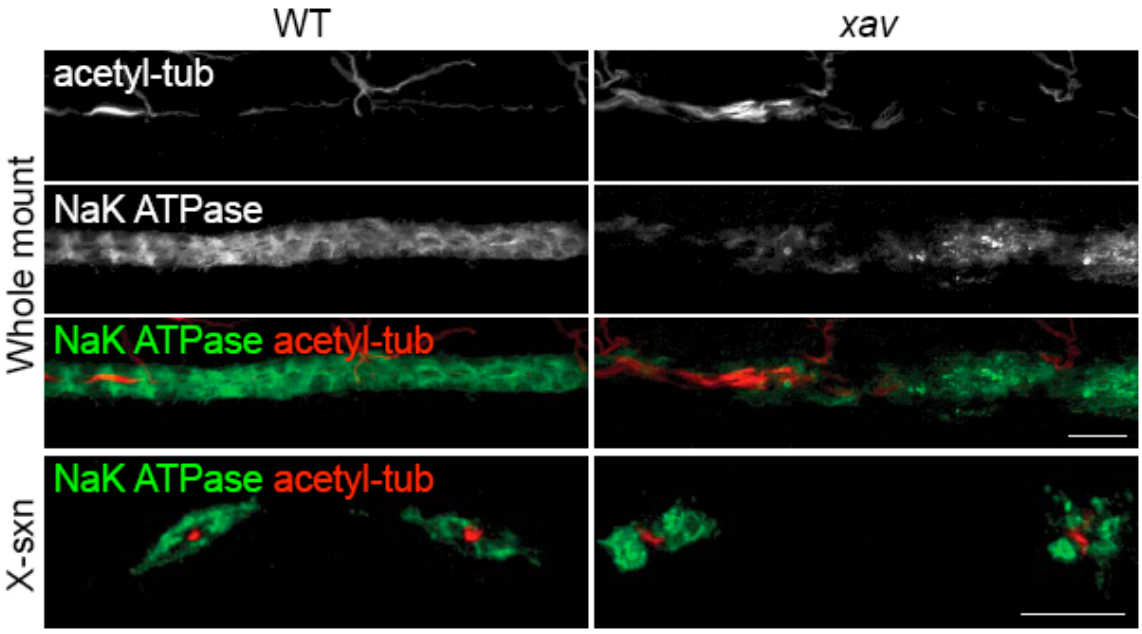

**Supplemental Figure 4. *xav* mutants exhibit respiratory deficiency**

**A.** Decreased rates of $O_2$ consumption in *xav* mitochondria. Homogenates from WT and *xav* embryos were incubated in an oxygen sensor chamber, and O2 consumption (y axis) as a function of incubation time (x axis) was recorded. In the upper panels, the mitochondria were incubated with α-ketoglutarate, and in the lower panels, mitochondria were incubated with fatty acid (C16 carnitine). ADP (0.2 mM) was added to the mitochondria to measure state 3 respiration. State 4 rates of respiration were calculated when ADP was depleted from the reaction. N = > 10 embryos from at least 2 carrier pairs for each metabolic assay**. B.** At ~56 hpf, a higher level of F1-F0 ATPase (complex V) protein was detected by immunostaining (red) in *xav* mutants (lower panels) compared to WT embryos (upper panels). A higher magnification view of the spinal cord is shown in the right most panels. TUNEL staining (green) was performed simultaneously and showed that there is increased cell death in the spinal cord in *xav* and that complex V positive cells are also TUNEL positive in *xav*. N = > 10 embryos from at least 2 carrier pairs for each immunostaining assay. Scale bar = 100 μm.

**Supplemental Figure 4. *xav* mutants exhibit respiratory deficiency**

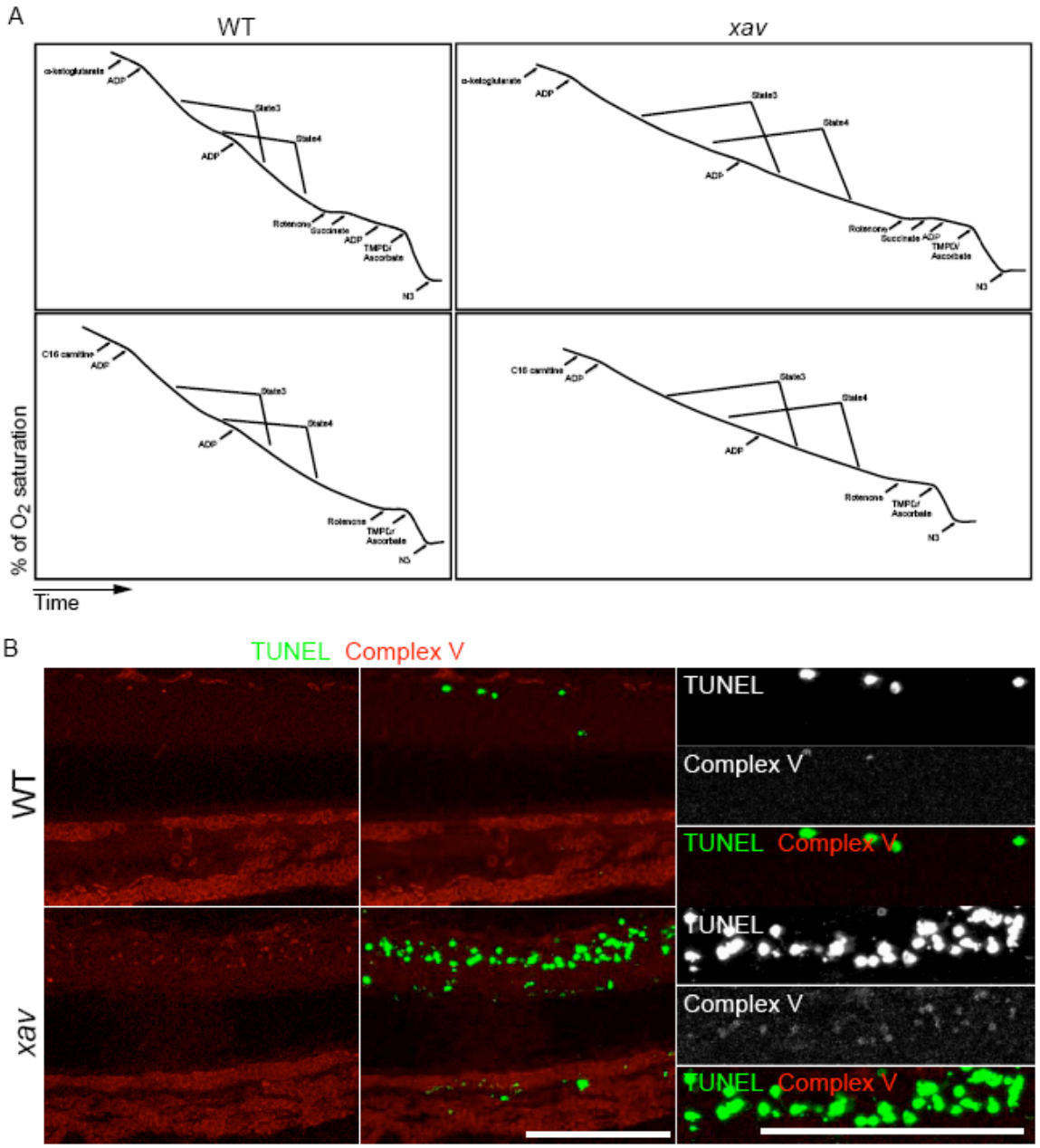

**Supplemental Figure 5. *xav* mutants exhibit neural and glial defects and cell death**

At 3 dpf, *xav* embryos exhibited increased cell death as assayed by TUNEL staining (green), reduced neuropil as assayed by SV2 staining (blue). Glia number and patterning as assayed by GFAP staining (red) was aberrant throughout the nervous system. Not only were glial processes irregular in shape, but clumps of GFAP+ cells were observed in several brain regions (white arrowheads point to several examples). N > 3 embryos, 1 carrier pair. Scale bar = 20 μm.

**Supplemental Figure 5.** ***xav*** **mutants exhibit neural and glial defects and cell death**

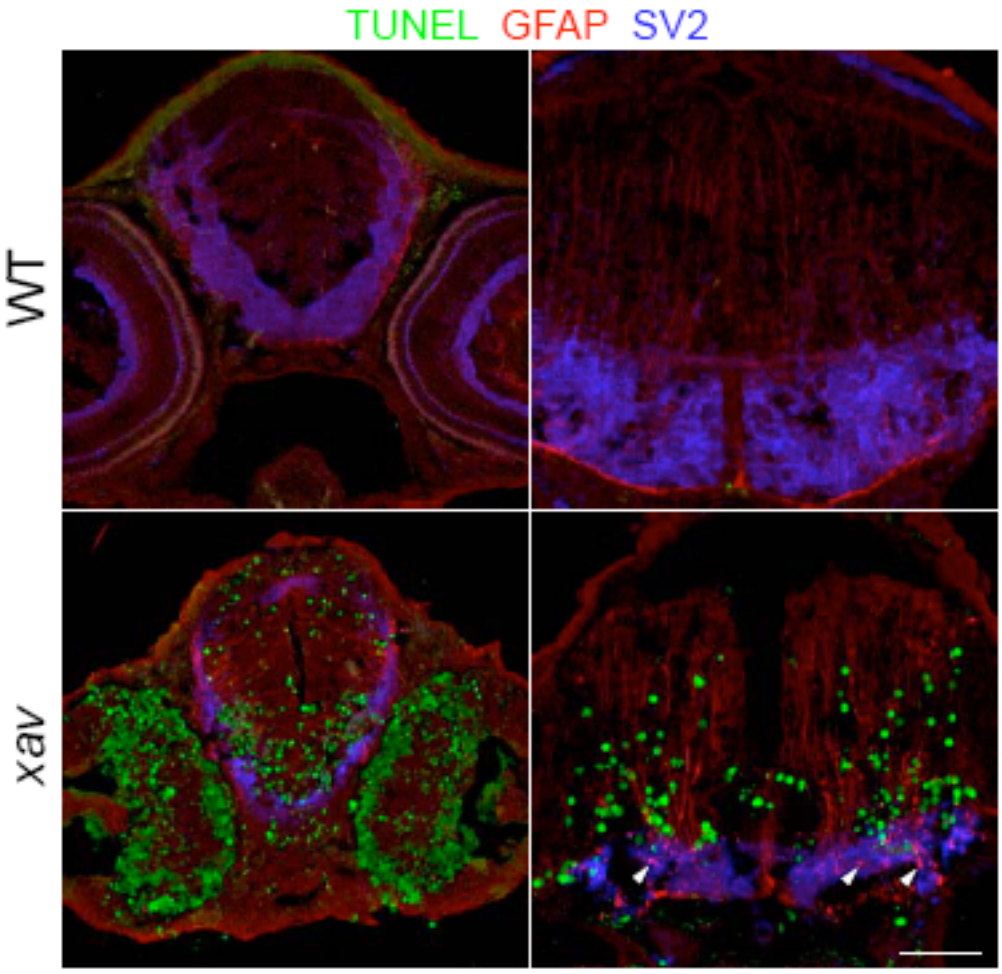

**Supplemental Figure 6. *xav* mutants exhibit reduced motor axon branching and neuromuscular synaptogenesis that are not caused by change of motor neuron number or viability**

**A.** SV2 (green) and AChR (red) labeling showed that motor axon branching and neuromuscular synaptogenesis were reduced in *xav* mutants and *etfdh* morphants compared to WT embryos, at 56 hpf and most strikingly at 72 hpf. Scale bar = 20 μm. **B.** Motor neuron number, as assayed by *in situ* hybridization for *islet-2*, is similar between *xav* mutants and WT embryos at 48 hpf. Scale bar = 100 μm. **C.** No substantial apoptosis was seen in the pool of motor neurons in *xav* compared to WT at 48 hpf, as assayed by double staining for TUNEL and Zn5, which labels secondary motor neurons. N > 10 embryos, 3 carrier pairs. Scale bar = 20 μm.

**Supplemental Figure 6.** ***xav*** **mutants exhibit reduced motor axon branching and neuromuscular synaptogenesis that are not caused by change of motor neuron number or viability**

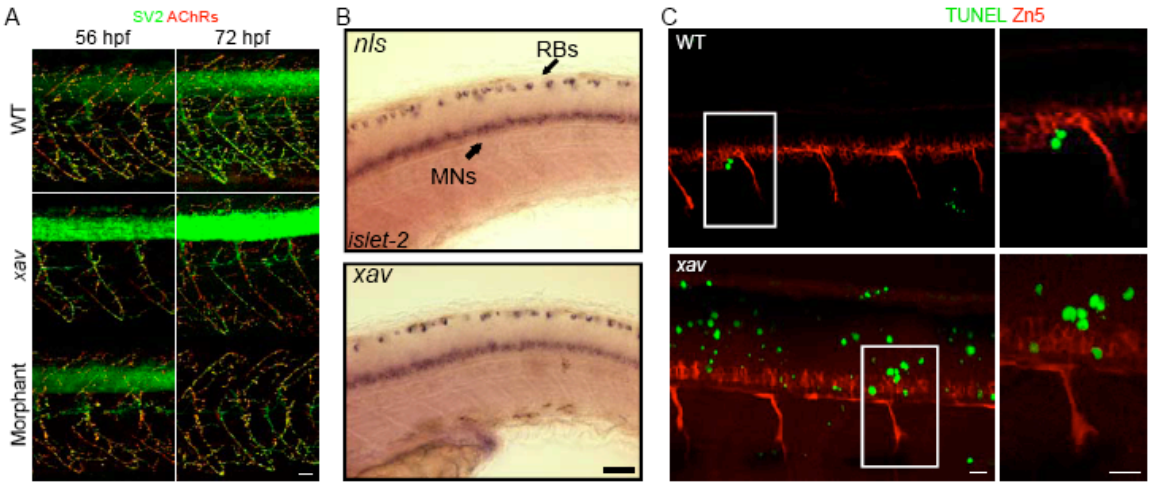

**Supplemental Figure 7. *xav* mutants display electrophysiological properties in the muscle, comparable to WT**

**A-C.** Miniature excitatory postsynaptic current (mEPC) recordings from fast muscles showed no statistical difference in terms of frequency, amplitude, rise time and exponential decay time. N = 4 embryos, 2 carrier pairs. **D.** Muscle fibers from *xav* embryos fire action potentials after exogenous stimulation, comparable in amplitude and shape to action potentials recorded from muscle fibers from WT embryos. N = 4 embryos, 2 carrier pairs.

**Supplemental Figure 7. *xav* mutants display electrophysiological properties in the muscle, comparable to WT**

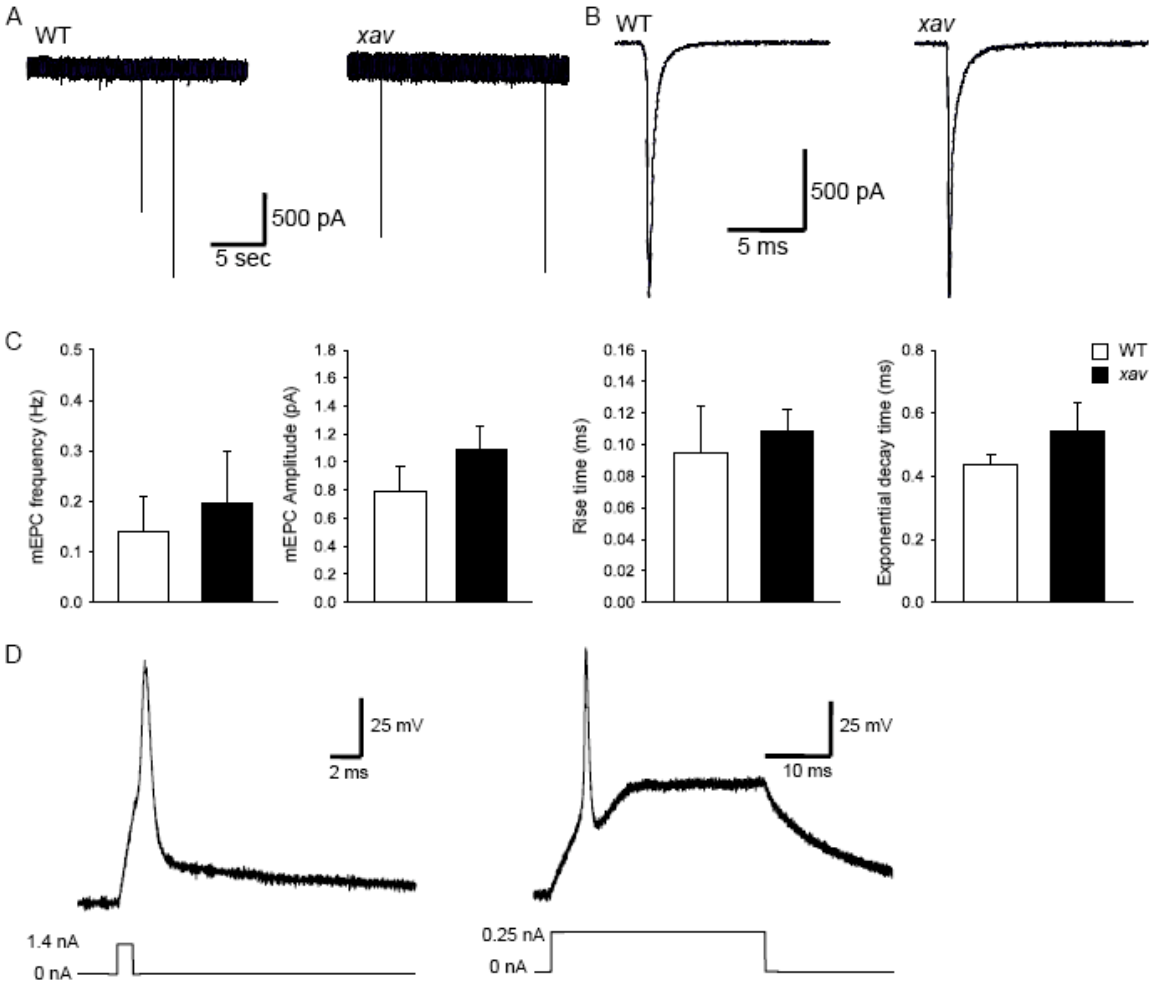

**Supplemental Figure 8. *xav* mutants exhibit aberrant mitochondria distribution in motor neurons**

**A-B.** Mito-GFP was expressed in motor neurons and branching and synapse formation followed over time. In WT embryos at ~56 hpf, mitochondria are distributed along the entire axon. Mitochondria are continuously added over time, increasing both in number and density. In contrast, in *xav* mutants, while the number and distribution of mitochondria clusters along the axon are comparable to WT embryos at ~56 hpf, the continuous addition of mitochondria is absent, resulting in a decrease of mitochondria cluster density by 3 dpf. N = 9-10 embryos, 3-4 carrier pairs. Scale bar = 20 μm.

**Supplemental Figure 8. *xav* mutants exhibit aberrant mitochondria distribution in motor neurons**

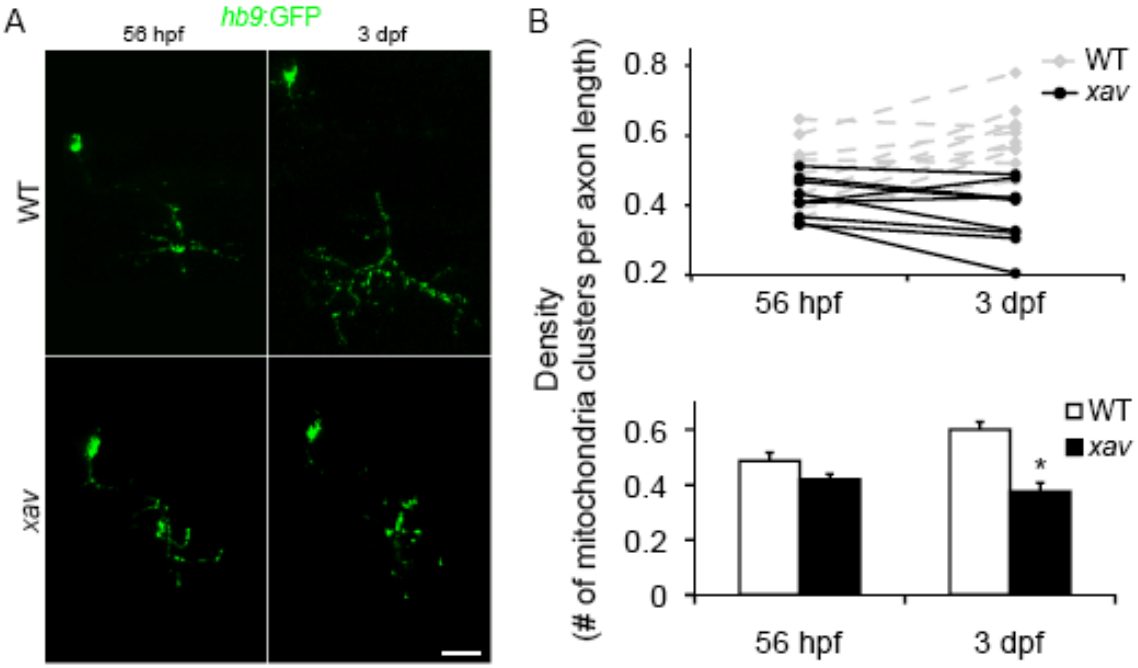

**Supplemental Figure 9. *xav* mutants exhibit cell death throughout the nervous system that is rescued by p53 morpholino knockdown and does not account for the motor axon branching, neuromuscular synapse or motility defects**

**A.** *xav* mutants exhibit widespread cell death in the peripheral and central nervous system. There was a dramatic increase in TUNEL+ cells in *xav* mutants compared to WT embryos at ~56-72 hpf, particularly in the retina and spinal cord. **B.** At 56 hpf**,** cell death was blocked using a morpholino against p53. However, blocking cell death did not block the reduction of axon branching and synaptogenesis phenotypes that are present in *xav* mutants. N > 6 embryos, 2 carrier pairs. Scale bar = 100 μm.

**Supplemental Figure 9. *xav* mutants exhibit cell death throughout the nervous system that is rescued by p53 morpholino knockdown and does not account for the motor axon branching, neuromuscular synapse or motility defects**

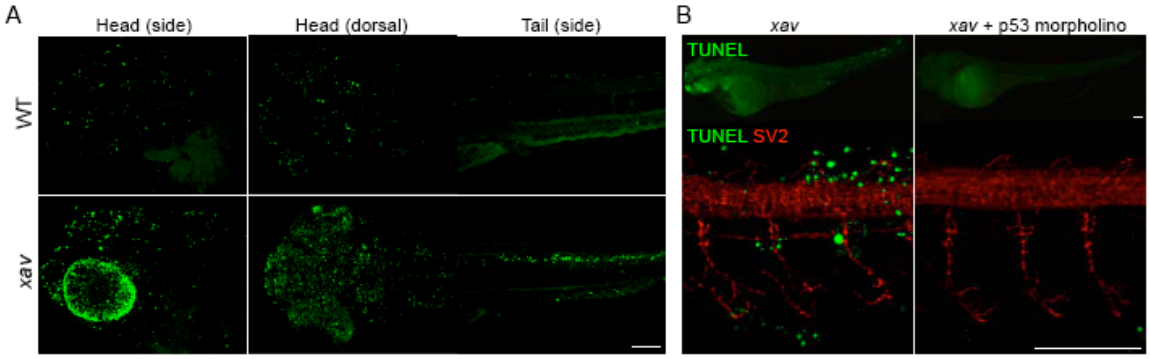

**Supplemental Table 1.** Primer sequences for new zebrafish simple sequence repeat (SSR) markers

| **SSR Name** | **Forward** | **Reverse** |
|---|---|---|
| Z15804-SSR4 | AACATGTTTGGGTATCCTGATTT | TGACCACCAGAATCAAGACG |
| 274P15-SSR1 | GGAAGCTAATTGCACGGTCT | AACCCACTGATAACAGTTCCAA |
| 50I13-SSR1 | TGCGTGCAATCAGGTTTAAG | TGTCCCAGTGACCAACATGA |
| 278P11-SSR1 | ATGGCAGCCTTCACCAAACA | CACCCGGAGTTCACCTTTCA |
| 276B5-SSR3 | TGCTTGCTAAGGTATTTGCTGA | TTAAAGCAGCAAGGCAATGA |
| 154C1-SSR1 | CAGGTATGAAATGCTGCTTGC | TTGCTCCAGCAGAGATGATG |
| 199B20-SSR1 | AGCTCCCAGGATTCCACTCT | CCCTAACTGTCTCTGCAACCA |
| 36H4-SSR1 | ATCCCTTTTGGGAAAACAGC | ACCTCATCACGTACGCACAA |
| **Gene Name** | | |
| *zgc:92093* (Acc # NM_001004598) | CGCATTCAACCTGGAAAACC | TGTGCCCCAGTGACGGTAAT |

**Supplemental Table 2.** Primers for qRT-PCR analyses of gene expression in *xav* and fibroblasts from human MADD patients

| Gene Name | Forward | Reverse |
|---|---|---|
| **Zebrafish** | | |
| *etfdh* | ACACGCTGGTTCTCCTCTGT | AGCGAAGCGTTCCATTTCTA |
| *β-actin1* | TGAATCCCAAAGCCAACAGAGAGA | TCACGACCAGCTAGATCCAGACG |
| *mt-nd5* | TTGACCATCGGGAAAATAGC | TTAGGGCTCAGGCGTTAAGA |
| *ndufs1* | GCCGTATGACACACTGGATG | CTCATGGGCCTGTTTGAAAT |
| *pgc-1β* | GGACGCCAGTGATTTTGACT | TCCAGCGCTGTACTGTATGG |
| *esrra* | CGAGGAGTTTGTCATGCTCA | CTGATGCAGCAGGTCTCGTA |
| *pparγ* | AGTACGGGGTCATCGAAGTG | GCGCAGACTCTTGAGGAACT |
| *ucp4* | GCGTGGAAAAGACAACCCTA | AAACGCACCTTTACCACGTC |
| *ndufb8* | TCTCCTGACCCCAGCTCTAA | CTTTCTCCTCTGCGGTTTTG |
| *cox5aa* | ACGGATGAGGAGTTTGATGC | TCCAGGATCTTTGGTTCAGG |
| *atp5g* | AGGAACCCATCTCTGAAGCA | GCAAACAGGATGAGGAAAGC |
| *ndufv1* | CTTGCAGAGAGGGAGTGGAC | GTCTCCTAAAGCGCAGATGG |
| *pgc-1α* | CTGCCTGAGCTTGACCTTTC | TTGGATGCTTCATTGCCATA |
| *nrf1* | CCGAACAGAGGAGCAGAAAC | GTGGCAACTTGTGTGGTGAC |
| *tfam* | AGCTGGCAGAGGACGATAAA | GTTTTGGCTTTGGCTTTGAG |
| *pparα* | CGACAAGTGTGAACGCAACT | TATCCGCCCAAAACGAATAG |
| *pparβ* | TGGAGTACGAGCGATGTGAG | CTTCTCCGCTTCTGGCATAC |
| *ucp2* | AGCTGGTGACGTTCCTCCTA | TTGTTCTCCCCCTGAATCTG |
| *cyt C* | GCATTGTCTGGGGTGAAGAT | TCTCTCGCCCTTCTTCTTGA |
| *catalase* | GCGGATACCAGAGAGAGTCG | ATCGGTGTCGTCTTTCCAAC |
| *glutathione reductase* | ATTGGCAGAGAACCCAACAC | ACATCCCCGACTGCATAGAC |
| *gpx1a* | GAAATACGTCCGTCCTGGAA | TCTCCCATAAGGGACACAGG |
| *gpx3* | TCCAGGAAATGGATTCGTTC | TCTCTCCTACAGGCGGACAT |

| | | |
|---|---|---|
| *hmox1* | GGAAGAGCTGGACAGAAACG | CGAAGAAGTGCTCCAAGTCC |
| *hspa9* | CGACTTGGGAACCACAAACT | CATTCCTACAAGCCGCTCTC |
| *eno1* | GGCAAAGGTGTCTCAAAAGC | TTGTTGTCTGTGCCATCCAT |
| *pgam1a* | TGAGAGGCATTGTGAAGCAC | GGCTTCAGGTTCTTGTCCAG |
| *pgk1* | GATGGAGTCCCTATGCCAGA | TGGACCCACACAGTCTTTCA |
| *pfkma* | CTGGAAGCCACTCCAGAGAC | AATCGACCCTCATTCATTGC |
| *aldoc* | CCATTGTGGAGCCTGAGATT | TCACCATGTTGGGTTTCAGA |
| *dlat* | GAGACCTGCTGGCTGAAATC | CTGGTGCCCTCAGAAATCAT |
| | | |
| **Human fibroblasts** | | |
| *ACTB* | GAGCTACGAGCTGCCTGACG | GTAGTTTCGTGGATGCCACAG |
| *PGC-1β* | TTATGCCTCCCTCACACCTC | TGAAGCTGCGATCCTTACCT |
| *PPARG* | GAGCCCAAGTTTGAGTTTGC | GGCGGTCTCCACTGAGAATA |
| *ESRRα* | AAAGTGCTGGCCCATTTCTAT | CCTTGCCTCAGTCCATCAT |
| *UCP3* | CTCCAGGCCAGTACTTCAGC | CGCAAAAAGGAGGGTGTAAA |
| *catalase* | TTTCCCAGGAAGATCCTGAC | ACCTTGGTGAGATCGAATGG |
| *glutathioine reductase* | ACTTGCCCATCGACTTTTTG | CATCTTCCGTGAGTCCCACT |
| *HSPA9* | AATTACTTGGGGCACACAGC | CGAAGCACATTCAGTCCAGA |
| *ENO1* | CTCCGTGACCGAGTCTCTTC | CCAGTCTTGATCTGCCCAGT |
| *PGAM1* | GGGGTCTAACCGGTCTCAAT | ACGTTTCCCCTCCTTGATCT |
| *PGK1* | TCACTCGGGCTAAGCAGATT | CAGTGCTCACATGGCTGACT |
| *PFKM* | AGAGCGTTTCGATGATGCTT | GTTGTAGGCAGCTCGGAGTC |

# Chapter 5

## General Conclusions and Future Directions

*The role of non-synaptic AChR clusters during early neuromuscular synaptogenesis*

The role of prepatterned AChR clusters in synapse formation has been a topic of much debate. *In vitro* studies demonstrate that motor axon growth cones ignore non-synaptic AChR clusters on cultured muscle fibers (Anderson and Cohen, 1977; Frank and Fischbach, 1979). In contrast, during axon regeneration in adult muscle, pre-existing AChR clusters are selectively reinnervated (Bennett and Pettigrew, 1976). Detailed studies of the function of prepatterned AChR clusters in the earliest stages of synaptogenesis have been hampered by technical limitations imposed by the study of mammalian embryos. Thus, it has remained unknown whether, *in vivo*, motor axon growth cones contact pre-existing AChR clusters, and if so, whether they incorporate them into newly formed synapses. My observations, made in collaboration with Jessica Panzer, demonstrated that protosynaptic AChR clusters mark target sites on muscle fibers that are preferentially contacted by motor axon growth cones. Such protosynaptic AChR clusters appear to be incorporated into newly formed synapses. This work provides a foundation for future studies, aimed at determining the identity of other postsynaptic proteins localized to protosynaptic receptor clusters, as well determining the mechanism by which motor axons detect these AChR clusters or presumptive synaptic sites marked

by pre-existing AChR clusters, which will greatly expand our understanding of this process. In addition, there is some evidence that axon growth cones in the CNS preferentially contact pre-existing target sites on dendrites (Cooper et al., 1992; Saito et al., 1992), and also that non-synaptic NMDA receptor clusters are present on the dendrites of CNS neurons prior to synaptogenesis (Aoki et al., 1994; Rao et al., 1998). Thus, prepatterning of postsynaptic targets may play a common, and little explored, role in synaptogenesis throughout the developing nervous system.

*Mechanisms that trigger the dispersion of prepatterned AChR clusters*

Unlike the appearance of aneural AChR clusters in mammals, which is contemporaneous with the motor axon branching and presynaptic terminal differentiation (Lin et al., 2001; Misgeld et al., 2002), at the zebrafish neuromuscular junction, these are present in the presumptive endplate band well in advance of motor axon innervation. Their dispersion, which is part of the process of refinement and determination of future synaptic sites, also occurs prior to axon ingrowth (Lin et al., 2001; Misgeld et al., 2002). While it is possible that ACh released by motor neurons may act as a dispersion factor at the mammalian neuromuscular junction (Misgeld et al., 2002), it is not very likely to be the case in zebrafish. It is conceivable that a muscle intrinsic mechanism may be responsible. It can be hypothesized that signaling coupled to MuSK activation (autoactivation or activation by an unknown ligand that generates the AChR prepattern (Kim and Burden, 2008; Lefebvre et al., 2007; Zhang et al., 2004)) may be stimulated by MuSK itself to initiate the internalization of AChRs, for degradation and/or for

mobilization and transportation. The observation that the dispersion takes place throughout the myotomal muscle and appears to be simultaneous across muscle fibers, suggest that this signal may be either far-reaching, or alternatively, be locally generated at the site of initial contact and then propagated among muscle fibers. This makes it reasonable to postulate that events such as spontaneous muscle contraction may elicit a signal that is dispersed among muscle fibers, possibly through gap junctions. Future studies to test these and other hypotheses, to identify putative dispersion factor(s), and to track the fate of existing, turning over and newly inserted populations of AChRs, may substantiate our understanding of the dynamics of postsynaptic specializations and their contribution to synaptogenesis.

*Notch-Delta signaling deficiency, as a result of dysregulated protein fucosylation, underlies neurogenic and synaptogenic defects in srn*

*srn* was identified as a synpatogeneic mutant that displays exuberant neuromuscular synapse formation (Panzer et al., 2005). We showed that the *srn* locus as a missense point mutation resulting in a Glycine to Valine change in GMDS, the first and rate-limiting enzyme in fucose metabolism. GMDS malfunction results in the loss of glycoprotein fucosylation, including Notch among many other proteins. My results strongly suggest that the dysregulated fucosylation of proteins in the Notch-Delta pathway accounts for the neurogenic defects prominent in *srn* mutants. While the lack of anti-zebrafish Notch antibodies prevented me from examining Notch fucosylation directly, Notch is a known substrate for fucosylation. Moreover, other proteins in the

Notch-Delta pathway, including Delta, Serrate and Jagged, contain consensus sequence(s) for O-linked fucose modification, C-X-X-G-G-S/T-C, where X is any amino acid and S/T is the modified residue (Harris and Spellman, 1993; Harris et al., 1993; Moloney and Haltiwanger, 1999) as well as for N-fucosylation, in which fucose is added to N-linked glycan side chains (Ishikawa et al., 2005; Jaeken and Matthijs, 2007; Sturla et al., 2003). In addition, Notch fucosylation has been shown to be reduced in the fly *Gfr* null model (Ishikawa et al., 2005) that is relevant to *srn*. It thus seems highly likely that the fucosylation of proteins in the Notch-Delta pathway is aberrant in *srn* mutants and that this accounts for some, but not all, *srn* neural phenotypes. Moreover, my observation that *srn* and Notch-Delta mutants have aberrant neuromuscular synapses, specifically dramatically increased presynaptic terminal area at the earliest established synapses in axial muscles, supports a previously underappreciated role for Notch-Delta signaling during synaptogenesis. Future experiments in which Notch-Delta signaling is manipulated after neurogenesis but before synaptogenesis would be of interest to parse the role of this pathway in neurogenesis and synaptogenesis.

*Notch-Delta independent pathways also contribute to srn neural defects*

While deficiencies in Notch-Delta signaling underlie some *srn* phenotypes, other *srn* phenotypes are likely to be independent of this pathway. *srn* mutants exhibit prominent defects in retinotectal connectivity that are quite different from those observed in Notch-Delta mutants. For example, in the retina, it has been shown that *crumbs* related genes, that are essential for the establishment of proper apical-basal polarity, are

important for retina patterning. Mutations in *crumbs homologue 2* (*crb2*), as in *oko meduzy* (*ome*), resulted in drastic neuronal patterning defects in the zebrafish retina (Malicki, 2000; Malicki and Driever, 1999; Malicki et al., 1996; Omori and Malicki, 2006; Schier et al., 1996; Tsujikawa and Malicki, 2004). Crumbs contains a consensus sequence for O-linked fucose modification, C-X-X-G-G-S/T-C, and thus is predicted to be fucosylated (Moloney and Haltiwanger, 1999). While complete loss of function of *crumbs* leads to catastrophic defects as in *ome*, *srn* mutants showed aberrant synaptic connectivity without disrupting retinal or tectal lamination. Thus it will be interesting to determine whether the lack of fucose modification in *crumbs* can cause similar defects as in *srn* mutants. Axon guidance molecules such as Netrin and Slits also contain consensus sequence for O-linked fucose modification (Moloney and Haltiwanger, 1999), and only Slit1a, but not Slit1b, Slit2 or Slit3, is expressed within the optic tectum and regulates retinal ganglion cell arborization and synaptogenesis (Campbell et al., 2007). In addition, the retinal ganglion axon arborization defects in *srn* mutants are similar to those seen in mutants *dackel* and *boxer*, which encode *ext2* and *extl3*, respectively, which are glycosyltransferases implicated in heparin sulfate biosynthesis (Lee et al., 2004). Heparin sulfate proteoglycans modulate axon guidance, in some cases by directly interacting with axon-guidance ligands and receptors, such as Slits and Robos (reviewed in Lee and Chien, 2004). Future work could focus on identifying the fucosylated proteins that mediate the axon guidance, branching, synaptogenesis and other neural deficits that are independent of Notch-Delta signaling.

*Mitochondrial and metabolic deficiency underlie neural and synaptic defects in xav*

*xav* was identified as a mutants that has reduced motor axon branching and neuromuscular synaptogenesis, and progressive paralysis (Panzer et al., 2005). We found that the *xav* mutation resides in electron transfer flavoprotein dehydrogenase (etfdh), which functions in the mitochondria electron transport chain and is important for fatty acid and choline metabolism. I showed that *xav* mutants exhibit metabolic and mitochondrial dysfunction, including altered energy metabolism, dysregulated ROS production and altered expression of genes critical for mitochondrial function. In particular, *xav* mutants showed excessive aerobic glycolysis, similar to the Warburg effect observed in cancer and other proliferating cells (Vander Heiden et al., 2009), leading to excessive neural cell proliferation, which is, at least in part, mediated by upregulation of the PPARG-ERK pathway. These abnormalities are associated with neural defects in *xav*, including reduced neuropil staining, abnormal glial patterning, reduced motor axon branching and synaptogenesis, as well as progressive paralysis. Future work could be focused on establishing the mechanistic connections between mitochondrial dysfunction and specific neural defects. It will be interesting to determine whether the increase of neural cell proliferation results in defects in neural differentiation and thus leads to the reduced neuropil and abnormal glial patterning. It will also be crucial to determine what pathway(s) causes the motor axon branching and synaptogenesis defects and the reduced motility and paralysis. Given our observation that motor neuron number is not reduced and that *xav* muscle fibers showed electrophysiological properties comparable to those in wild type embryos, one hypothesis worth testing is that abnormal neural proliferation leads to malformation of the circuitry

underlying motor behavior. Alternatively, mitochondrial malfunction within motor neurons may also account for these defects, and this would be consistent with my observation that the distribution of mitochondria within motor neuron axons is aberrant.

*Linking metabolism and neural development*

It is well appreciated that energy metabolism and brain function are highly coupled processes. It is known that two principle components of energy production, mitochondrial oxidative metabolism and glycolysis, play pivotal roles in nervous system function, such as synaptic transmission, by providing ATP in the former case, or specific glycolytic intermediates in the case of glycolysis (Okada and Lipton, 2007). When metabolism is aberrant, as seen in inherited disorders of metabolism, most of these conditions are associated with some neurologic sequelae, such as congenital malformation of the nervous system, mental retardation, mood disorders, seizures, ataxias and neuropathy (reviewed in Ramachandram, 2009). The mechanistic links between metabolism and neural development and function are areas of active research. I identified one pathway, the PPARG pathway, that is upregulated due to metabolic deficiency in both *xav* and fibroblasts from MADD patients, and that, in *xav*, leads to excessive neural proliferation. Future work could be focused on elucidating the mechanism(s) upstream of PPARG and understanding how metabolic status is sensed, in turn regulating the PPARG pathway. Moreover, it will be interesting to determine the targets of PPARG activation that mediate neural proliferation, and how these may be related in *xav* and MADD patients.

*Conclusion*

My first project using *in vivo* imaging and cellular analyses of the formation of neuromuscular synapses uncovered important roles of the prepatterning of postsynaptic specializations in guiding synaptogenesis. My work on the characterization of a zebrafish mutant *slytherin* revealed a previously underappreciated role for protein fucosylation in regulating neural and glial specification and patterning, axon branching and synaptogenesis, through both Notch dependent and independent pathways. My work on the characterization of a second mutant, *xavier*, extends our understanding of the connections among mitochondria, metabolism and neural development, and provide insights into how mitochondrial and metabolic dysfunction lead to defects in neural proliferation, glial patterning, axon branching and synaptogenesis in zebrafish and human patients. It is possible that this work, while foundational, may in the future lead to insights that could provide avenues for therapeutic intervention in humans with mutations in these genes that compromise neural development and function and thus impact quality of life.

## References

**Anderson, M. J. and Cohen, M. W.** (1977). Nerve-induced and spontaneous redistribution of acetylcholine receptors on cultured muscle cells. *J Physiol* **268**, 757-73.

**Aoki, C., Venkatesan, C., Go, C. G., Mong, J. A. and Dawson, T. M.** (1994). Cellular and subcellular localization of NMDA-R1 subunit immunoreactivity in the visual cortex of adult and neonatal rats. *J Neurosci* **14**, 5202-22.

**Bennett, M. R. and Pettigrew, A. G.** (1976). The formation of neuromuscular synapses. *Cold Spring Harb Symp Quant Biol* **40**, 409-24.

**Campbell, D. S., Stringham, S. A., Timm, A., Xiao, T., Law, M. Y., Baier, H., Nonet, M. L. and Chien, C. B.** (2007). Slit1a inhibits retinal ganglion cell arborization and synaptogenesis via Robo2-dependent and -independent pathways. *Neuron* **55**, 231-45.

**Cooper, R. L., Fernandez-de-Miguel, F., Adams, W. B. and Nicholls, J. G.** (1992). Anterograde and retrograde effects of synapse formation on calcium currents and neurite outgrowth in cultured leech neurons. *Proc R Soc Lond B Biol Sci* **249**, 217-22.

**Frank, E. and Fischbach, G. D.** (1979). Early events in neuromuscular junction formation in vitro: induction of acetylcholine receptor clusters in the postsynaptic membrane and morphology of newly formed synapses. *J Cell Biol* **83**, 143-58.

**Harris, R. J. and Spellman, M. W.** (1993). O-linked fucose and other post-translational modifications unique to EGF modules. *Glycobiology* **3**, 219-24.

**Harris, R. J., van Halbeek, H., Glushka, J., Basa, L. J., Ling, V. T., Smith, K. J. and Spellman, M. W.** (1993). Identification and structural analysis of the tetrasaccharide NeuAc alpha(2-->6)Gal beta(1-->4)GlcNAc beta(1-->3)Fuc alpha 1-->O-linked to serine 61 of human factor IX. *Biochemistry* **32**, 6539-47.

**Ishikawa, H. O., Higashi, S., Ayukawa, T., Sasamura, T., Kitagawa, M., Harigaya, K., Aoki, K., Ishida, N., Sanai, Y. and Matsuno, K.** (2005). Notch deficiency implicated in the pathogenesis of congenital disorder of glycosylation IIc. *Proc Natl Acad Sci U S A* **102**, 18532-7.

**Jaeken, J. and Matthijs, G.** (2007). Congenital disorders of glycosylation: a rapidly expanding disease family. *Annu Rev Genomics Hum Genet* **8**, 261-78.

**Kim, N. and Burden, S. J.** (2008). MuSK controls where motor axons grow and form synapses. *Nat Neurosci* **11**, 19-27.

**Lee, J. S., von der Hardt, S., Rusch, M. A., Stringer, S. E., Stickney, H. L., Talbot, W. S., Geisler, R., Nusslein-Volhard, C., Selleck, S. B., Chien, C. B. et al.** (2004). Axon sorting in the optic tract requires HSPG synthesis by ext2 (dackel) and extl3 (boxer). *Neuron* **44**, 947-60.

**Lefebvre, J. L., Jing, L., Becaficco, S., Franzini-Armstrong, C. and Granato, M.** (2007). Differential requirement for MuSK and dystroglycan in generating patterns of neuromuscular innervation. *Proc Natl Acad Sci U S A* **104**, 2483-8.

**Lin, W., Burgess, R. W., Dominguez, B., Pfaff, S. L., Sanes, J. R. and Lee, K. F.** (2001). Distinct roles of nerve and muscle in postsynaptic differentiation of the neuromuscular synapse. *Nature* **410**, 1057-64.

**Malicki, J.** (2000). Harnessing the power of forward genetics--analysis of neuronal diversity and patterning in the zebrafish retina. *Trends Neurosci* **23**, 531-41.

**Malicki, J. and Driever, W.** (1999). oko meduzy mutations affect neuronal patterning in the zebrafish retina and reveal cell-cell interactions of the retinal neuroepithelial sheet. *Development* **126**, 1235-46.

**Malicki, J., Neuhauss, S. C., Schier, A. F., Solnica-Krezel, L., Stemple, D. L., Stainier, D. Y., Abdelilah, S., Zwartkruis, F., Rangini, Z. and Driever, W.** (1996). Mutations affecting development of the zebrafish retina. *Development* **123**, 263-73.

**Misgeld, T., Burgess, R. W., Lewis, R. M., Cunningham, J. M., Lichtman, J. W. and Sanes, J. R.** (2002). Roles of neurotransmitter in synapse formation: development of neuromuscular junctions lacking choline acetyltransferase. *Neuron* **36**, 635-48.

**Moloney, D. J. and Haltiwanger, R. S.** (1999). The O-linked fucose glycosylation pathway: identification and characterization of a uridine diphosphoglucose: fucose-beta1,3-glucosyltransferase activity from Chinese hamster ovary cells. *Glycobiology* **9**, 679-87.

**Okada, Y. and Lipton, P.** (2007). GLUCOSE, OXIDATIVE ENERGY METABOLISM, AND NEURAL FUNCTION IN BRAIN SLICES. In *Handbook of Neurochemistry and Molecular Neurobiology*, (ed. A. Lajtha G. E. Gibson and G. A. Dienel), pp. 924: SPRINGER REFERENCE.

**Omori, Y. and Malicki, J.** (2006). oko meduzy and related crumbs genes are determinants of apical cell features in the vertebrate embryo. *Curr Biol* **16**, 945-57.

**Panzer, J. A., Gibbs, S. M., Dosch, R., Wagner, D., Mullins, M. C., Granato, M. and Balice-Gordon, R. J.** (2005). Neuromuscular synaptogenesis in wild-type and mutant zebrafish. *Dev Biol* **285**, 340-57.

**Rao, A., Kim, E., Sheng, M. and Craig, A. M.** (1998). Heterogeneity in the molecular composition of excitatory postsynaptic sites during development of hippocampal neurons in culture. *J Neurosci* **18**, 1217-29.

**Saito, Y., Murakami, F., Song, W. J., Okawa, K., Shimono, K. and Katsumaru, H.** (1992). Developing corticorubral axons of the cat form synapses on filopodial dendritic protrusions. *Neurosci Lett* **147**, 81-4.

**Schier, A. F., Neuhauss, S. C., Harvey, M., Malicki, J., Solnica-Krezel, L., Stainier, D. Y., Zwartkruis, F., Abdelilah, S., Stemple, D. L., Rangini, Z. et al.** (1996). Mutations affecting the development of the embryonic zebrafish brain. *Development* **123**, 165-78.

**Sturla, L., Rampal, R., Haltiwanger, R. S., Fruscione, F., Etzioni, A. and Tonetti, M.** (2003). Differential terminal fucosylation of N-linked glycans versus protein O-fucosylation in leukocyte adhesion deficiency type II (CDG IIc). *J Biol Chem* **278**, 26727-33.

**Tsujikawa, M. and Malicki, J.** (2004). Genetics of photoreceptor development and function in zebrafish. *Int J Dev Biol* **48**, 925-34.

**Vander Heiden, M. G., Cantley, L. C. and Thompson, C. B.** (2009). Understanding the Warburg effect: the metabolic requirements of cell proliferation. *Science* **324**, 1029-33.

**Zhang, J., Lefebvre, J. L., Zhao, S. and Granato, M.** (2004). Zebrafish unplugged reveals a role for muscle-specific kinase homologs in axonal pathway choice. *Nat Neurosci* **7**, 1303-9.